High-performance infrared photodetectors based on AlInAsSb digital alloy materials system

---

A Dissertation

Presented to

the Faculty of the School of Engineering and Applied Science

University of Virginia

In Partial Fulfillment of

the Requirements for the Degree of

Doctor of Philosophy

By

Dekang Chen

August 2022

APPROVAL SHEET

This Dissertation
is submitted in partial fulfillment of the requirements
for the degree of
Doctor of Philosophy

Author Signature: Dekang Chen

This dissertation has been read and approved by the examining committee:

Advisor: Joe C. Campbell _____

Committee Chair: Andreas Beling _____

Committee Member: Steven M. Bowers _____

Committee Member: Kyusang Lee _____

Committee Member: Bellave S. Shivaram _____

Accepted for the School of Engineering and Applied Science:

Craig H. Benson, School of Engineering and Applied Science

August 2022

This dissertation is dedicated to my parents

Table of Contents

Acknowledgement 1
Abstract 3
List of figures 5
List of tables 10
1. Introduction 11
2. Infrared SACM avalanche photodiodes 13
    2.1. Motivation 13
    2.2. Photon-trapping structure simulation and design 15
        2.2.1. Photonic crystal 15
        2.2.2. Metal grating 21
    2.3. Device simulation and design 31
    2.4. Fabrication and characterization 39
    2.5. Quantum efficiency enhancement 44
        2.5.1. Metal grating 44
        2.5.2. Edge coupling 62
    2.6. Bandwidth characterization and analysis 74
    2.7. Future work 84
3. Infrared nBn photodetectors 87
    3.1. Motivation 87
    3.2. Device simulation and design 88
    3.3. Fabrication and characterization 91
    3.4. Bandwidth characterization and analysis 96
    3.5. Future work 115
4. Double mesa APDs 117
    4.1. Motivation 117
    4.2. Determine background doping polarity by double mesa structure 119
    4.3. Future work 129
References 132
Appendix 136
    A. Normal APD fabrication recipe 136
    B. Metal grating fabrication by single layer lift-off 137

C. Metal grating fabrication by double layer lift-off 138
List of Publications 139

Acknowledgement

A qualified scientist or engineer is supposed to be rational, but I am sometimes an emotional person and feel lucky about my life. I feel I may be blessed that whenever I reach a critical moment on my path, I always meet precious people who help and change my life. Among them, my advisor Joe, is undoubtedly the most important one. The three years I spent in Joe's group were the period when I felt like I was improved the most. Joe's passion for research, rigorous attitude and humility have always subtly influenced and encouraged me. In the past years, I have not only made research progress from Joe's strong support, but also learned a lot of methods and attitudes of doing work and being a good person from him. I think these will benefit me for the rest of my life. I sincerely wish good health and happiness for Joe and his family, and I believe he will lead more great achievements for our field in the future.

I would like to thank all my committee members, Prof. Andreas Beling, Prof. Steven M. Bowers, Prof. Kyusang Lee and Prof. Bellave S. Shivaram for their time and support. Their comments are very insightful which helps me to improve my research a lot.

I am very grateful to all my group members. They are all my good teachers and precious friends who not only gave me selfless guidance in research and study, but also gave me encouragement and companionship. I couldn't have achieved what I am today without their help.

I would like to thank my collaborators at the University of Texas for their help on my research. Thanks all the IFAB cleanroom stuffs and UVa stuffs who helped me during my research and life at UVa.

Last but not least, I would like to thank my parents. No matter when it is and where am I, they always give me the most selfless care and help. Their expectations are the biggest motivation for me

to move forward. Thanks my brother Dean Chen. He always encouraged me when I was at my lowest and kept me back on my feet. Love you all forever,

University of Virginia

Charlotteville, VA, USA

August 2022

Abstract

The mid-wave infrared (MWIR) spectrum, typically referring to the wavelength range of 2 - 5 μm, has the potential to enable next-generation breakthroughs in photonics applications. Therefore, high-performance photodetectors that operate in this range are of high interest. However, high signal-to-noise ratio (SNR), a critical figure of merit for photodetectors, is extremely difficult to achieve in the MWIR range. The challenge is twofold, one is the low signal power level, determined by the application scenario in the MWIR range, and the other is the high noise level, which originates from the high dark current of the narrow bandgap material. To address these challenges, my PhD research focuses on developing high performance MWIR photodetectors based on the AlInAsSb digital alloy materials system. The primary goal is to achieve high SNR. The solution is twofold.

The first approach is to achieve a high signal level by using the internal gain of avalanche photodiodes (APDs). To maximize the SNR performance, I designed a new separate absorption, charge, and multiplication (SACM) APD with an ultra-thin absorber to suppress dark current, while the quantum efficiency of the device is maintained at a high level by using photo-trapping structures. The device exhibits dark current level more than 2 order lower than the previous record result at 2 μm, and the quantum efficiency reaches ~ 22 % by using surface metal gratings and ~ 24 % through edge coupling. Moreover, the maximum gain of the device is as high as ~ 1000 at 240 K. Consequently, record high SNR performance is demonstrated by the thin SACM APD. Additionally, the thin absorber design also improved the speed performance. The frequency response measurement shows that the maximum bandwidth reaches ~ 7 GHz, and the gain-bandwidth product is over 200 GHz. Both of these two values are more than 4 time higher than the previously record bandwidth for 2 μm APDs. In the future, this idea of using the combination of an ultra-thin absorber and photon trapping structures can be applied to longer wavelength cut-off APDs in the MWIR range.

Instead of boosting up the signal level by using an APD, another solution to improve the SNR is to suppress the dark current by using an n-barrier-n (nBn) photodetector design. Although nBn photodetectors have been substantially improved using superlattice materials systems, their performance is limited by their valence band discontinuity, especially in the long wave infrared range. However, the AlInAsSb digital alloy materials system has been found to have minimal valence band discontinuity, which provides the potential to improve the performance nBn photodetectors fabricated from conventional materials. Therefore, I designed and demonstrated the first AlInAsSb nBn, and the detectivity of the device at room temperature achieved record high value at 2 μm. Additionally, since the target of the previous research on nBn photodetectors is high SNR, the frequency behavior and bandwidth have not been studied. To enable high-speed applications, I proposed the first equivalent circuit model and the bandwidth theory for the nBn photodetector. The new model provided good fits to measurements, and moreover, it reveals the limiting factor of the bandwidth of nBn photodetector and the methods to improve the frequency response. This work lays the foundation for extending the application sphere of nBn photodetectors to high-speed scenarios in the MWIR range.

Additionally, I developed a special double mesa approach that is easy and straightforward to determine the background doping density and polarity of an unintentionally doped layer, which is a critical parameter for the design of both the SACM APD and the nBn photodetectors in my PhD work. Moreover, my research on the double mesa also reveals its potential to suppressing surface leakage dark current and extend surface breakdown voltage, which will be a promising area of research in the future.

List of figures

Fig. 2.2-1 (a) Schematic cross-section of the $Al_xIn_{1-x}As_ySb_{1-y}$ SACM APD. (b) One unit cell of the triangular-lattice photonic crystal. (c) Normalized distribution of the electric field intensity square $|E|^2$ in the x-z plane. (d) Normalized distribution of the electric field intensity square $|E|^2$ in the x-y plane at the center of the resonance. 16

Fig. 2.2-2 Calculated absorption spectra of the SACM APD with the photonic crystal, anti-reflection coating, and flat surface. Anti-reflection coating is set as a quarter wavelength thick SiO_2 layer on the device, and the flat surface is set with no additional structures. 18

Fig. 2.2-3 Photonic band diagram for the TE mode in the triangular-lattice photonic crystal. The y-axis represents the frequency, and the x-axis represents the transverse component of the wavevector. The left inset shows the Brillouin zone with the irreducible zone filled by red, and the right inset shows a cross-section of the air-hole arrays of the photonic crystal. The cyan solid line and the black solid lines represent the light lines in the air and in the semiconductor, respectively. 20

Fig. 2.2-4 (a) Schematic cross-section of the $Al_xIn_{1-x}As_ySb_{1-y}$ SACM APD. (b) One unit cell of the metal grating structure. (c) Normalized distribution of the magnetic field intensity square $|H|^2$ in the x-z plane. The region between the two dash lines represents the intrinsic $Al_{0.3}InAsSb$ layer, and the solid line represents the top of the GaSb substrate. (d) Normalized distribution of the magnetic field intensity square $|H|^2$ in the x-y plane at the center of the resonance peak in the absorber. The white arrows represent the magnetic field vectors and have no z component. The region between two solid lines indicates the position of the metal stripes. Incidence wavelength in (c) and (d) is 2 μm. 22

Fig. 2.2-5 Calculated absorption spectra of the device with metal grating, anti-reflection coating, and the flat surface. The anti-reflection coating and flat surface are set the same as in the simulation of photonic crystals. The absorption was calculated from the top of the GaSb contact layer to the GaSb substrate; the metal is not included. 24

Fig. 2.2-6 The variation of the absorption versus the metal grating thickness. 26

Fig. 2.2-7 Poynting vector distribution under the metal grating in the x-z plane with an incidence wavelength of 2 μm, where the normalized magnitude of the Poynting vector is indicated by the scale bar on the left. The dash line represents the top of the absorber. 28

Fig. 2.2-8 (a) Illustration of the polarization angle sweep in the simulation. (b) Absorption and surface reflectivity at 2 μm wavelength of the 1D metal grating with different polarization angles. (c) Absorption and surface reflectivity at 2 μm wavelength of the 2D metal grating with different polarization angles. 29

Fig. 2.2-9 (a) Illustration of the incidence and polarization angle sweep in the simulation. (b) Absorption at 2 μm wavelength of the metal grating with different incidence angles. 30

Fig. 2.3-1 Schematic cross section of the SACM APD reported in ref. [8]. 32

Fig. 2.3-2 Simulated electric field profile with different charge layer doping concentrations. 34

Fig. 2.3-3 Simulated band diagram with (a) an abrupt grading layer and (b) a continuous grading layer at equilibrium and under reverse bias. 36

Fig. 2.3-4 (a) I-V curves measured from TLMs with different N type contact layer solutions. (b) forward biased I-V curves of the device and estimated series resistances by using different N type contact layer solutions. 37
Fig. 2.3-5 Simulated band diagram of the SACM APD with a $Al_{0.3}InAsSb$ contact layer added between the GaSb buffer layer and the $Al_{0.7}InAsSb$ contact layer. 38
Fig. 2.3-6 Schematic cross section of the thin absorber SACM APD. 38
Fig. 2.4-1 Microscope image of fabricated thin absorber SACM devices. 39
Fig. 2.4-2 measured capacitance-voltage curve of a 150 μm diameter device. 40
Fig. 2.4-3 (a) Measured current-voltage and gain curve of a 100 μm diameter device at room temperature. (b) Measured gain curves of the device at 240 K with different optical attenuations. 41
Fig. 2.4-4 measured excess noise factors of a 100 μm diameter device under 2 μm illumination. . 42
Fig. 2.4-5 Comparison of excess noise factors at gain of ~ 10 for common III-V APDs and Si APDs. 42
Fig. 2.4-6 Measured dark current density at various temperatures and reference curves of state-of-the-art HgCdTe APD [33] and AlInAsSb SACM APD [8] at 2 μm. 43
Fig. 2.4-7 Measured external quantum efficiency of a 150 μm diameter device at room temperature. 44
Fig. 2.5.1-1 Optimal dimensions of the metal grating in one unit cell 45
Fig. 2.5.1-2 (a) Simulated magnetic field profile at 2 μm and (b) absorption spectrum with the optimal grating dimensions. 46
Fig. 2.5.1-3 Simulated absorption efficiency with different metal thicknesses and grating duty cycles. 46
Fig. 2.5.1-4 Test grating patterns (a) on a thin PMMA layer after development and (b) after thin metal deposition and lift-off; The e-beam energy is 30 keV and the exposure does is 45 $\mu C/cm^2$. 48
Fig. 2.5.1-5 Metal grating pattern after lift-off using a ~ 1.2 μm thick PMMA layer. 50
Fig. 2.5.1-6 Metal grating pattern after lift-off using a ~ 0.7 μm thick PMMA layer. 50
Fig. 2.5.1-7 Illustration of the challenge while using (a) a thin PR layer and (b) a thick PR layer to lift off thick metal by a single PR layer. 52
Fig. 2.5.1-8 General process flow of double layer lift-off [36]. 52
Fig. 2.5.1-9 Collapsed pattern after the double layer lift-off. 53
Fig. 2.5.1-10 Over-undercut structure shown in the collapsed pattern region after the double layer lift-off. 53
Fig. 2.5.1-11 Illustration of the optimized e-beam lithography process for lifting off thick metal by double photoresist layer. 54
Fig. 2.5.1-12 Metal grating patterns fabricated by the optimized e-beam lithography for double layer lift-off. 55
Fig. 2.5.1-13 Process flow for fabricating metal gratings on the top of APD devices. 57
Fig. 2.5.1-14 Lift-off problem for large area metal gratings. 57
Fig. 2.5.1-15 Illustration of (a) original grating layout and (b) improved discrete blocks design. .. 57

Fig. 2.5.1-16 Comparison of large area metal grating patterns (a) without gap added and (b) with gap added. 58
Fig. 2.5.1-17 SEM image of the fabricated thin SACM APD with sub-micron metal gratings on the top surface. 59
Fig. 2.5.1-18 Measured quantum efficiency of the thin SACM APD with surface metal gratings versus (a) wavelength and (b) grating spacing. 60
Fig. 2.5.1-19 Comparison of (a) the designed metal grating pattern and (b) fabricated metal grating pattern. 62
Fig. 2.5.2-1 (a) Schematic of the edge coupled waveguide APD. (b) Cross section views the thin absorber SACM APD. 63
Fig. 2.5.2-2 Simulated internal and external quantum efficiency of the edge coupled waveguide SACM APD at 2 μm; the grey dashed line shows the reference efficiency measured by surface normal illumination. 64
Fig. 2.5.2-3 Illustration of the device structure of waveguide APD (a) before cleaving (b) after cleaving. 65
Fig. 2.5.2-4 Illustration of (a) the vertically aligned design and (b) the vertically mismatched design of waveguide APD devices 66
Fig. 2.5.2-5 Illustration of the horizontal mismatch layout of waveguide APD devices 67
Fig. 2.5.2-6 Illustration of the mismatched design for waveguide APD devices. 68
Fig. 2.5.2-7 Illustration of the final photomask layout for waveguide APDs. 68
Fig. 2.5.2-8 Microscope view of the waveguide APDs (a) before cleaving and (b) after cleaving. 69
Fig. 2.5.2-9 (a) Microscope image of the cleaved waveguide APDs from the top and (b) high resolution SEM image of the cleaved edge of the waveguides. 70
Fig. 2.5.2-10 Schematic setup for the waveguide APD measurement. 71
Fig. 2.5.2-11 Microscope picture of the waveguide APD measurement setup. 71
Fig. 2.5.2-12 Measured external quantum efficiency of the edge coupled waveguide SACM APD at 2 μm; simulated result is plotted for reference. 73
Fig. 2.6-1 Experimental setup for waveguide APD bandwidth measurement. 74
Fig. 2.6-2 (a-1) ~ (e-1) Measured frequency response and (a-2) ~ (e-2) extracted 3-dB bandwidth and gain bandwidth product of waveguide APDs with dimensions of (a-#) 40 × 45 μm (b-#) 40 × 25 μm (c-#) 20 × 40 μm (d-#) 10 × 55 μm and (e-#) 10 × 35 μm, respectively. 78
Fig. 2.6-3 Summary of the measured bandwidth (BW) and gain-bandwidth product (GBP) of waveguide APDs with different dimensions. 78
Fig. 2.6-4 Measured S_{11} curves of waveguide APDs with dimensions of (a) 10 × 60 μm (b) 20 × 60 μm (c) 30 × 60 μm and (d) 40 × 60 μm and at various bias voltages. 79
Fig. 2.6-5 Equivalent circuit model of P-I-N photodiode 79
Fig. 2.6-6 Simulated S_{11} curves of waveguide APDs with dimensions of (a) 10 × 60 μm (b) 20 × 60 μm (c) 30 × 60 μm and (d) 40 × 60 μm and at bias voltages of -19V. 81
Fig. 2.7-2 Sandwich absorber design for releasing the absorber thickness limit for photon-trapping SACM APDs. 86
Fig. 3.2-1 Schematic cross-section of the AlInAsSb nBn photodetector. 89

Fig. 3.2-2 Simulated energy band diagram of the AlInAsSb nBn photodetector (a) at equilibrium, (b) under a reverse bias of -1V, and (c) under a forward bias of 1V. 89
Fig. 3.2-3 (a) Simulated responsivity and absorption and (b) carrier collection efficiency of the AlInAsSb nBn photodetector versus absorber thickness under 2-μm illumination. The absorber, barrier and buffer layer are assumed to be unintentionally doped with an n-type background doping concentration of 1×10^{16} cm^{-3}; the simulation temperature is 300 K. 90
Fig. 3.2-4 Simulated responsivity versus voltage of the AlInAsSb nBn photodetector with different n-type doping concentrations in the absorber and the buffer layer. 91
Fig. 3.3-1 (a) Measured I-V curves of a 150-μm diameter AlInAsSb nBn photodetector at room temperature; total current was measured under 2-μm laser illumination. (b) Measured C-V curves of AlInAsSb nBn photodetectors with different mesa diameters. 93
Fig. 3.3-2 (a) Room temperature measured EQE of a 250-μm diameter AlInAsSb nBn photodetector versus wavelength for reverse bias from -0.1V to -3V. (b) EQE at 2-μm versus reverse bias voltage. 94
Fig. 3.3-3 (a) Measured dark current density of a 150-μm diameter AlInAsSb nBn photodetector at different temperature. (b) Measured dark current density as a function of inverse temperature. The dashed line shows the fitting to the diffusion-current-limited regime. 96
Fig. 3.4-1 Schematic of directly probing the nBn photodetectors using a G-S probe. 97
Fig. 3.4-2 Setup schematic of the frequency response measurement 98
Fig. 3.4-3 Frequency response of AlInAsSb nBn photodetectors with device diameters of (a) 80 μm (b) 100 μm (c) 150 μm (d) 200 μm at various bias voltages. Photocurrent is set to 10 μA. 99
Fig. 3.4-4 3-dB bandwidth of AlInAsSb nBn photodetectors with various device diameters and bias voltages. Photocurrent is set to 10 μA 100
Fig. 3.4-5 Band diagram and electric field profiles of AlInAsSb nBn photodetectors at various bias voltages. The simulation is performed under dark condition. 101
Fig. 3.4-6 Simulated transit-time bandwidth versus bias voltage curve for AlInAsSb nBn photodetectors. 101
Fig. 3.4-7 Equivalent circuit model of a typical P-I-N photodiode 103
Fig. 3.4-8 Measured capacitance-voltage curves by a LCR meter at a frequency of 10 kHz and calculated theoretical junction capacitance of AlInAsSb nBn photodetectors with different device diameters. 103
Fig. 3.4-9 Equivalent circuit model of (a) an N-P-N phototransistor [74] and (b) an nBn photodetector 104
Fig. 3.4-10 (a) Correspondence between the band structure and the new equivalent circuit model for nBn photodetectors. (b) Band diagram and electron carrier density distribution of AlInAsSb nBn photodetectors at equilibrium and under reverse bias. The simulation is performed under dark condition. 106
Fig. 3.4-11 Measured $S11$ curves of AlInAsSb nBn photodetectors with device diameters of (a) 80 μm (b) 100 μm (c) 150 μm (d) 200 μm at various bias voltages 108
Fig. 3.4-12 Simulated $S11$ curves of AlInAsSb nBn photodetectors with device diameters of (a) 80 μm (b) 100 μm (c) 150 μm (d) 200 μm at a bias voltage of -2 V 109

Fig. 3.4-13 Frequency response of AlInAsSb nBn photodetectors with device diameters of (a) 80 μm (b) 100 μm (c) 150 μm (d) 200 μm measured at different photocurrent levels; simulated frequency response is plotted in dash grey for reference; bias voltage is set at -2V. 114

Fig. 4.1-1 Simulated band diagram and electric field profile with N-type and P-type background doping in the absorber. 118

Fig. 4.2-1. (a) Schematic cross-section of the $Al_{0.7}InAsSb$ APDs with an over-etched double mesa structure and (b) Top view of a fabricated device. The doping concentrations are as follows: (1) GaSb P^+ 1×10^{19} cm^{-3}; (2) $Al_{0.7}InAsSb$ P 5×10^{18} cm^{-3}; (3) $Al_{0.7}InAsSb$, unintentionally doped; (4) $Al_{0.7}InAsSb$ N 5×10^{18} cm^{-3}; (5) GaSb N 1×10^{18} cm^{-3}; (5) GaSb substrate; The UID layer thickness is 1000 nm and 887 nm for sample A and sample B, respectively. 120

Fig. 4.2-2. Measured capacitance-voltage curves of double mesa devices with different top and bottom mesa diameters from sample A. The legend refers to the mesa size of d_{bottom_mesa} - d_{top_mesa} μm. (b) Current-voltage curves of a 150-100 μm double mesa device on sample A. The total current was measured under flood illumination with a lamp. 122

Fig. 4.2-3. Measured capacitance of double mesa devices from sample A compared with the theoretical capacitance calculated using either the top mesa diameter or bottom mesa diameter. The capacitance is measured at -15 V in (a) (b) and measured at -30 V in (c) (d). The number inside the figure represents the size of another mesa that is not marked by the horizontal axis. 123

Fig. 4.2-4. Normalized distribution of the electric field magnitude E inside the double mesa devices from sample A (p-type background). 124

Fig. 4.2-5. Measured capacitance-voltage curves of double mesa devices with different top and bottom mesa diameters from sample B. The legend refers to the mesa size of d_{bottom_mesa} - d_{top_mesa} μm. (b) Current-voltage curve of a 150-100 μm double mesa device on sample A. The total current was measured under flood illumination with a lamp. 125

Fig. 4.2-6. Measured capacitance of double mesa devices from sample B compared to the theoretical capacitance calculated using either (a) top mesa diameter or (b) bottom mesa diameter. The capacitance is measured at -30 V. The number inside the figure represents the size of another mesa that is not marked by the horizontal axis. 126

Fig. 4.2-7. Normalized distribution of the electric field magnitude E inside the double mesa devices on sample B (n-type background). 127

Fig. 4.2-8. Measured capacitance at 80 K of double mesa devices from sample B compared to the theoretical capacitance calculated using either(a) top mesa diameter or (b) bottom mesa diameter. The number inside the figure represents the size of another mesa that is not marked by the horizontal axis. (c) Capacitance-voltage curves of the 150-100 μm devices from sample B measured at different temperatures. 128

Fig. 4.3-1. Design of the double mesa structure for the thin absorber SACM APD and the simulated electric field profile at – 20 V. 130

Fig. 4.3-2. Design of the triple mesa structure for the thin absorber SACM APD and the simulated electric field profile at – 20 V. 131

List of tables

Table 2.2-1 Optical Constants at 2 μm wavelength of the materials used in the simulation..... 17
Table 2.3-1 Simulated transit-time bandwidth with various multiplication layer thickness 33
Table 2.3-2 Simulated punch through voltage, bandwidth, and gain with different charge layer doping concentrations. 34
Table 2.3-3 Simulated transit-time bandwidth with an abrupt grading layer and a continuous grading layer. 35
Table 2.5.1-1 Thickness of PMMA photoresist with different spin speed 47
Table 2.6-1 Fitted parameters in the equivalent circuit model of P-I-N photodiode..... 81
Table 2.6-2 Measured 3-dB bandwidth and the theoretical RC bandwidth calculated by the fitted resistances and capacitances. 81
Table 2.6-3 Measured 3-dB bandwidth, theoretical RC bandwidth, simulated transit-time bandwidth and the calculated substrate limiting bandwidth. 83
Table 3.4-1 Fitted parameters in the equivalent circuit model of an nBn photodetector 109
Table 3.4-2 Theoretical 3-dB bandwidth calculated by equation (5) and the fitted parameters in Table 1 110

1. Introduction

Mid-wave infrared (MWIR) photonics possesses the potential for realizing next-generation breakthroughs in a wide range of areas including spectroscopy [1, 2], medical diagnostics [3, 4], environmental monitoring [5], communication [6] and defense. Consequently, photodetectors that operate in this spectral range are attracting growing interest [7].

The primary figure of merit for the MWIR photodetectors is the signal-to-noise ratio (SNR), which is the ratio between the desired power of the signal and the undesired power of the noise. In analog photodetection such as imaging, high SNR provides an output signal above the circuit noise floor and increases the sensitivity of the detection system. In digital logic applications such as photon-counting receivers, high SNR generates output strong enough to minimize the bit error rate (BER) of the following decision circuit.

However, improving the SNR is challenging for MWIR photodetectors. The first challenge is the low signal level. Different from optical telecommunications where the signal is guided by a fiber and can be amplified by an optical amplifier, many applications in MWIR range, such as imaging and spectroscopy, are required to detect radiation signals from a long distance through free space. Therefore, the optical signal that reaches the photodetector is usually weak and in some instances reaches the few-photons level. Consequently, low noise is crucial for MWIR detectors to avoid weak signals being overwhelmed by the noise floor. However, achieving low noise is also challenging in the MWIR range. One of the primary noise sources of photodetectors is dark current, which refers to the current that is measured in the absence of illumination. Due to the narrow bandgap material used to absorb the mid-wave optical signal, such as HgCdTe, InAs/GaSb type-II superlattice (T2SL) and InAs/InAsSb type-II strained-layer superlattice (T2SLS), the dark current of the device is usually exceedingly high due to the Shockley-Read-Hall (SRH) generation, tunneling, or even thermal

generation in the narrow bandgap. Therefore, MWIR photodetectors, such as HgCdTe detectors, need to be cooled to cryogenic temperatures to avoid excessively high dark current, and this adds cost and creates difficulties in packaging and system design.

While efforts toward enhancing the SNR of conventional MWIR photodetectors are ongoing, another promising approach is to develop new materials systems that may overcome the limits of conventional photodetectors. Recently, high performance avalanche photodiodes (APDs) have been demonstrated in the $Al_xIn_{1-x}As_ySb_{1-y}$ (referred to as AlInAsSb) digital alloy material system [8, 9]. These devices show high gain, low dark current, extremely low excess noise and high temperature stability compared to conventional III-V materials. Moreover, AlInAsSb can be lattice matched to GaSb and InP substrates for a broad range of bandgap energies (from 0.25 eV to 1.3 eV). This characteristic provides high flexibility for designing complex photodetector structures, such as staircase APDs [10], and is also beneficial for developing complex designs for MWIR photodetectors.

To address these challenges, my PhD research focuses on high performance MWIR photodetectors based on the AlInAsSb digital alloy materials system. The primary goal is to achieve high SNR, but my approach is twofold. One is toward achieving a higher signal level by using avalanche photodiodes with internal gain to boost signal power, and also introducing photo-trapping structures to further improve quantum efficiency. The other direction is to reduce the noise level of the photodetector using an n-Barrier-n structure. Additionally, my PhD work investigates the high frequency behavior of MWIR photodetectors so as to promote its use in high-frequency scenarios in the MWIR spectral range.

2. Infrared SACM avalanche photodiodes

2.1. Motivation

To improve SNR, one approach is to boost the signal level. However, many applications in the MWIR range need to detect weak optical signals from free space, where it is hard to amplify the optical signal using an optical amplifier. An alternative method is to utilize the internal gain of the photodetector itself. Therefore, owing to their low-noise internal gain, avalanche photodiodes (APDs) have become a widely used detector in optical receivers.

APDs are semiconductor devices that convert photons to electrons and then multiply the number of electrons, resulting in an amplified photocurrent signal. The internal gain of an APD originates from impact ionization. Under high reverse bias, a high electric field exists in the depletion region along which the progenerated carriers accelerate. However, the velocity of the photogenerated carriers does not continue to increase with higher field but will saturate due to collisions in the crystal lattice. During this process, the excess carrier energy is transferred to the crystal. Once the crystal energy is higher than the threshold energy, bound electrons can be excited across the energy gap and generate a free electron-hole pair. Subsequently, the generated carriers will continue to accelerate along the electric field, collide with crystal and generate more electron-hole pairs. This impact ionization process is figuratively referred as an “avalanche” process. The resulting internal gain can amplify weak optical signals above the noise floor, which makes APDs very useful for sensing weak optical signals in MWIR applications.

However, designing APDs in MWIR range is challenging. Since the internal gain of APDs result from impact ionization, a high electric field is required. However, due to the narrow bandgap materials used for MWIR absorption, Shockley-Read-Hall (SRH) generation and tunneling in the narrow-bandgap material will significantly increase under high electric field, which will lead to

excessively high dark current. An APD design has been developed to address this issue, the separate absorption, charge, and multiplication (SACM) APD. Since the challenge is the conflict between the high electric field required for high gain, and the low electric field required to maintain low dark current in narrow bandgap material, the SACM structure partitions the absorption and the impact ionization process into different materials. In a typical SACM APD, a narrower-bandgap absorber and a wider-bandgap multiplication layer are positioned on opposite sides of a lightly doped charge layer [8]. Consequently, when the depletion extends into the absorber, a high electric filed is already built up in the multiplication layer due to the voltage needed to deplete the charge layer. This achieves high electric field in the multiplication layer, providing high gain, and a low electric field in the absorber, minimizing the dark current from the narrow bandgap material. The SACM design has significantly improved the SNR of infrared APDs.

Recently, our group has demonstrated high performance 2 μm SACM APDs based on the AlInAsSb digital alloy materials system and has achieved start-of-the-art performance at ~100K higher temperature than HgCdTe APDs [8]. In order to further increase the SNR, lower dark current is required. Since the primary source of dark current is the narrow bandgap absorber, one of the most straightforward solutions is to reduce the thickness of the absorber. However, a thinner absorber also results in less absorption and low quantum efficiency. Therefore, the challenge is to maintain a high quantum efficiency while decreasing the thickness of the absorber. Two conventional approaches to achieve this are to incorporate an anti-reflection (AR) coating and using back-illumination structures. While an AR coating can be used to improve the efficiency, its affect is limited, particularly for thin absorbing layers. Back-illumination can ideally increase the quantum efficiency by 2 times by taking advantage of reflection from the top contact if absorption in the substrate is not significant, however, packaging and measurement are more complicated. An alternative solution is to utilize photon-

trapping structures without increasing or even decreasing the absorber thickness. Recently, photodetectors that incorporate various photon-trapping structures such as photonic crystals [11-13], metal gratings [14, 15] and metallic nanoantennas [16-18] have been reported. The primary motivation for these approaches is to diffract and couple normal incident light into the laterally-propagating mode inside the absorber. This can significantly improve the quantum efficiency compared to conventional structures. However, these approaches have not been applied to APDs for 2-μm detection. In this section, I describe two approaches, photonic crystals, and metal gratings, that I have investigated to enhance the absorption at 2 μm in the $Al_xIn_{1-x}As_ySb_{1-y}$ SCAM APDs reported in [8]. The goal is to enable a thin absorber design to minimize dark current.

At the same time, a thinner absorbing layer also increase the transit-time component of the bandwidth, and therefore provide the potential to achieve higher speed. With rapidly expanding applications in the MWIR and LWIR range, device speed is attracting more and more attention. However, bandwidth performance of MWIR APDs, especially at room temperature, has rarely been reported except for a few low bandwidth results [19, 20]. Therefore, addressing the thin absorber and photo trapping designs also has the potential to enable high bandwidth 2 μm APDs, which is another important research that will be introduced in this section.

2.2. Photon-trapping structure simulation and design

2.2.1. Photonic crystal

Various types of photonic crystals have been shown to enhance the absorption of photodiodes by diffracting and coupling the normal incident light into the laterally propagation mode formed by the epitaxial layers and the photonic crystal. For the SACM APD, the fundamental condition for achieving absorption enhancement with a photonic crystal is that a waveguide structure containing the absorber layer is supported. $Al_xIn_{1-x}As_ySb_{1-y}$ is an excellent material system to satisfy this

condition. Based on our experimental measurements, $Al_xIn_{1-x}As_ySb_{1-y}$ with a lower Al content has a higher refractive index and a narrower bandgap, thus the absorption layer functions as the core of a waveguide. An epitaxial layer stack of the $Al_xIn_{1-x}As_ySb_{1-y}$ SACM APDs for which the absorption enhancement approaches have been designed is shown in Fig. 2.2-1 (a). The epitaxial layers were grown on n-type Te-doped GaSb (001) substrates by solid-source molecular beam epitaxy (MBE).

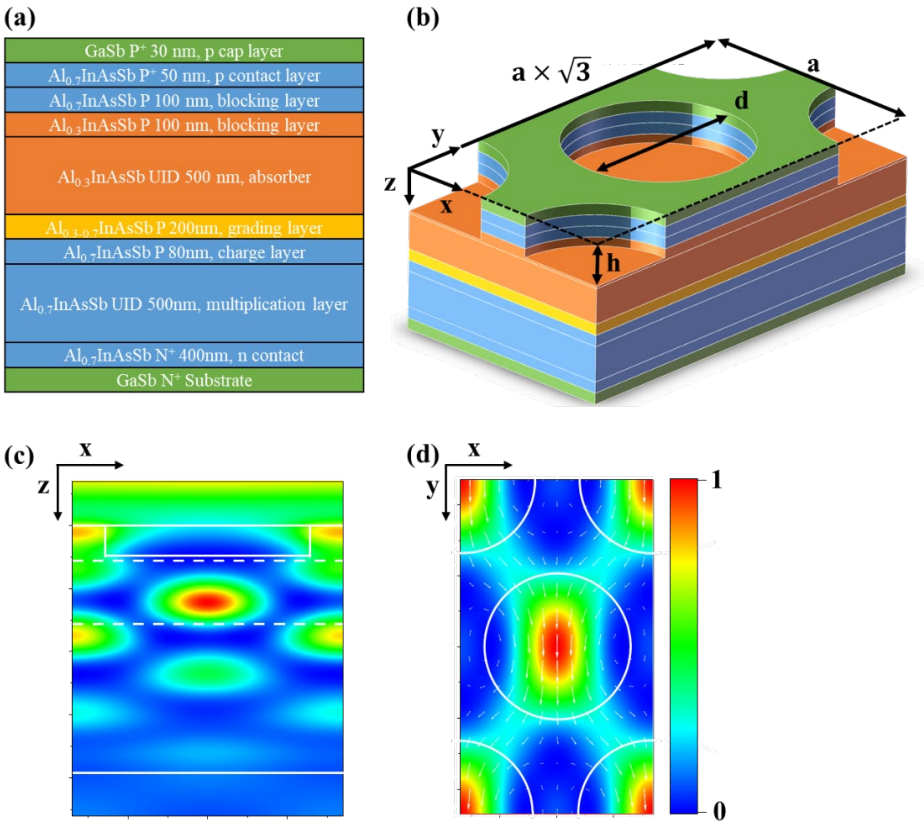

Fig. 2.2-1 (a) Schematic cross-section of the $Al_xIn_{1-x}As_ySb_{1-y}$ SACM APD. (b) One unit cell of the triangular-lattice photonic crystal. (c) Normalized distribution of the electric field intensity square $|E|^2$ in the x-z plane. (d) Normalized distribution of the electric field intensity square $|E|^2$ in the x-y plane at the center of the resonance.

Fig. 2.2-1 (b) illustrates a triangular-lattice photonic crystal with air-hole arrays etched into the layers; spacing a, diameter d, and depth h of the air-holes were optimized to obtain the highest

absorption. To calculate the field distribution and absorption, the finite-difference time-domain (FDTD) method was used with periodic boundaries set in the x and y directions, by which the simulation region can be reduced to one unit cell as shown in Fig. 2.2-1 (b). In the z-direction, perfectly matched layer (PML) boundaries were set to avoid an artificial resonance between the top and bottom boundaries in the vertical direction. For the 2-μm optical input, a normal-incidence, plane-wave source was configured above the device with TEM polarization and the electric field direction parallel with the y-axis. All the refractive indices and absorption coefficients used in the simulation were obtained by experimental measurements and Sellmeier dispersion fitting, as listed in Table 2.2-1.

Table 2.2-1 Optical Constants at 2 μm wavelength of the materials used in the simulation

Materials	Real refractive index n	Imaginary refractive index k
$Al_{0.3}InAsSb$	3.52	0.053
$Al_{0.3\text{-}0.7}InAsSb$	3.43	0
$Al_{0.7}InAsSb$	3.34	0
GaSb	3.88	0
Ag	0.65	12.2

The optimal dimensions of the air-holes were determined to be a = 680 nm, d = 520 nm, and h = 260 nm. Fig. 2.2-1 (c) shows the electric field intensity distribution in the x-y plane with these dimensions. There are multiple resonance peaks, among which the strongest is in the $Al_{0.3}InAsSb$ absorption layer. Weaker resonance peaks are also found in the GaSb cap layer, $Al_{0.3\text{-}0.7}InAsSb$ grading layer, and $Al_{0.7}InAsSb$ multiplication layer. This is due to the diffracted light coupled into multiple resonance modes supported by the complex layer structure. Fig. 2.2-1(d) shows a cross-section at the center of the resonance peak in the absorber, the electric field intensity, and vector distribution in the x-y plane. The resonance mode in the absorber is TE mode with resonance peaks

located beneath the airhole region, where the electric field tends to distribute in the same direction (y-direction).

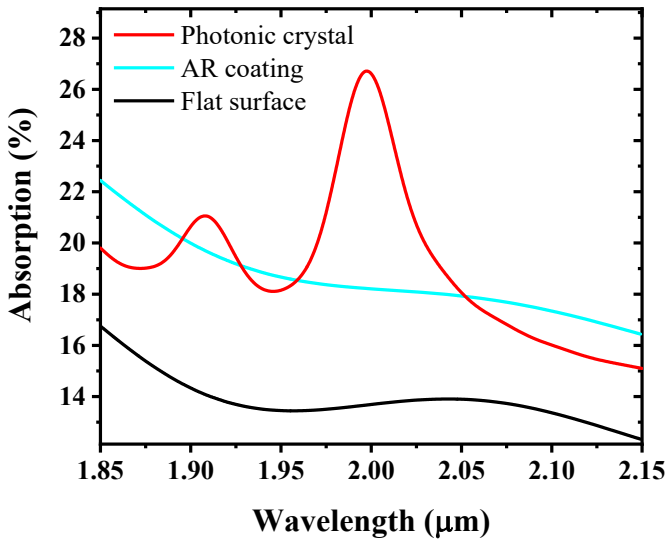

Fig. 2.2-2 Calculated absorption spectra of the SACM APD with the photonic crystal, anti-reflection coating, and flat surface. Anti-reflection coating is set as a quarter wavelength thick SiO_2 layer on the device, and the flat surface is set with no additional structures.

The absorption spectra of the APD with a photonic crystal, an SiO_2 AR coating, or the bare as-grown structure are plotted in Fig. 2.2-2. For the photonic crystal, the absorption was enhanced to ~ 27 %, which is double that of the bare surface (~ 13 %) and even higher than the AR coating (~ 18 %). Moreover, there are two resonance peaks found in the absorption spectra of the photonic crystal, one at 2 μm, and the other around 1.9 μm. This is due to the multiple resonance frequencies of the triangular-lattice photonic crystal. The enhancement provided by the photonic crystal is due to the interaction of light with both the photonic crystal and the layer structure. This can be understood by analysis of two effects. First, the normal incidence light is diffracted when it

illuminates the top of the photonic crystal due to the periodic refractive indices. Subsequently, part of the diffracted light is coupled into the laterally propagating photonic-crystal-slab mode formed by the photonic crystal and the absorption layer, with the result that the absorption is enhanced by photon-trapping. Hence, the absorption is determined by the combination of the coupling process (how much light is coupled into the photonic-crystal-slab mode), the fractional mode intensity within the absorber layer, and the fraction of light transmitted through the absorber without being coupled into any mode. As for the photonic-crystal-slab mode, in the vertical direction (z-direction), the light is confined by total internal reflection due to the refractive index difference between the $Al_{0.3}InAsSb$ layer ($n \sim 3.52$ at 2 μm) and the surrounding $Al_{0.7}InAsSb$ layers ($n \sim 3.34$ at 2 μm). In the transverse directions (x-y plane), the field profile is determined by the 2D photonic crystal. In order to investigate the transverse intensity distribution of the photonic-crystal-slab mode, the photonic band diagram was calculated based on both the Monte Carlo method and FDTD simulation. The simulation region was one unit cell in the x-y plane with a z range from the top of the photonic crystal to the bottom of the air-holes. As shown in Fig. 2.2-3, a photonic bandgap is created by the photonic crystal structure. Moreover, the two peak wavelengths in the absorption spectra, 2 μm and 1.9 μm, are exactly at the M and K points in the first Brillouin zone, respectively. Consequently, the light propagates as a Bloch wave with zero group velocity in the transverse direction at these two wavelengths and thus the absorption is significantly increased. Furthermore, it is notable that both 2 μm and 1.9 μm wavelengths are on the upper band above the bandgap, which is generally referred to as the "air band" for a photonic crystal, where the electric field intensity is concentrated in the region with a lower effective refractive index. This phenomenon is consistent with the mode profile shown in Fig. 2.2-1 (d), where the electric field intensity is concentrated under the air-holes. If the size of the photonic crystal is modified and the lower band under the bandgap, generally referred to

as the “dielectric band” where the electric field is concentrated in the region with a higher effective refraction index, is shifted up, the 2 μm wavelength can be coupled into the dielectric band. However, for the present case, I found no hole dimensions where the mode exists at the edge of the Brillouin zone in the dielectric band, i.e., the absorption is not enhanced at all when the mode exists in the dielectric band. This is reasonable if we look into the layer structure of the device. If the light is coupled into the dielectric band, the electric field will be primarily concentrated in the higher index region where the GaSb contact layer and p-type $Al_{0.7}InAsSb$ layer exist, in which little light is absorbed at 2 μm.

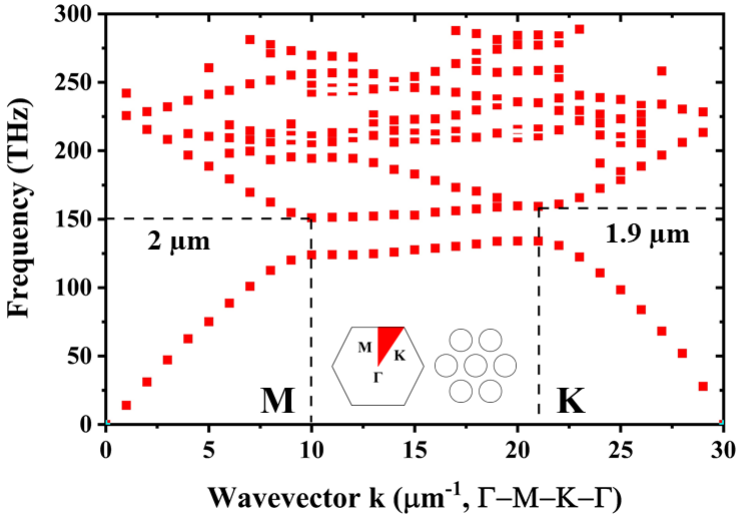

Fig. 2.2-3 Photonic band diagram for the TE mode in the triangular-lattice photonic crystal. The y-axis represents the frequency, and the x-axis represents the transverse component of the wavevector. The left inset shows the Brillouin zone with the irreducible zone filled by red, and the right inset shows a cross-section of the air-hole arrays of the photonic crystal. The cyan solid line and the black solid lines represent the light lines in the air and in the semiconductor, respectively.

For the coupling process, not all the diffracted light that is coupled into the photonic-crystal-slab mode overlaps the absorber. Part of the optical field in the mode is in the GaSb, $Al_{0.7}InAsSb$, and

$Al_{0.3\text{-}0.7}InAsSb$ layers, as indicated by Fig. 2.2-1 (c). As a result, the coupling efficiency of the photonic crystal is lower than it would be for a higher confinement factor.

In summary, for the photonic crystal approach the mechanisms for the absorption enhancement are two-fold. First, it supports a photonic-crystal-slab mode in the absorber, where the light is confined in the vertical direction by total internal reflection and forms a standing wave in the transverse direction. Second, it also serves as a lateral coupler that diffracts the normal incidence light and couples it into the laterally-propagating photonic-crystal-slab mode in the absorber.

2.2.2. Metal grating

Metal gratings have also been proved to be an effective approach to enhance the light absorption of photodiodes [14, 15] and other optoelectronic devices [21-23]. The mechanism is generally more complex due to the metal plasmon, but similar to the photonic crystal approach, lateral coupling is beneficial in most cases.

In order to study the physics of light absorption using metal grating structures, the structure was simulated using FDTD. The simulation setup is similar to that for the photonic crystal approach, except the air-hole arrays were replaced by an Ag metal grating. As shown in Fig. 2.2-4 (b), the grating has period *a*, strip width *b,* and metal thickness *h*. The simulation region is one grating period in the x-y plane with periodic boundary, and from the top of the metal grating to the GaSb substrate in the z-direction with PML boundary. A normal-incidence plane wave source with TEM polarization was set above the device, and the electric field direction was set to be parallel with the x-axis.

The dimensions of the metal grating were optimized to be $a = 586$ nm, $b = 370$ nm (fill factor $b/a \sim 0.63$), and $h = 420$ nm for maximum absorption at 2 μm wavelength. As indicated in Fig. 2.2-4 (c), significant resonance was found in the absorber, but the mode is different from that of the

photonic crystal. As indicated in Fig. 2.2-4 (d), the resonance mode is TM mode with the magnetic field in the y-direction. The orientation of the magnetic field is reversed in the region under and outside the metal grating. Moreover, different from the photonic crystal, there is no obvious resonance peak found outside the absorber, which indicates high coupling efficiency for the metal grating.

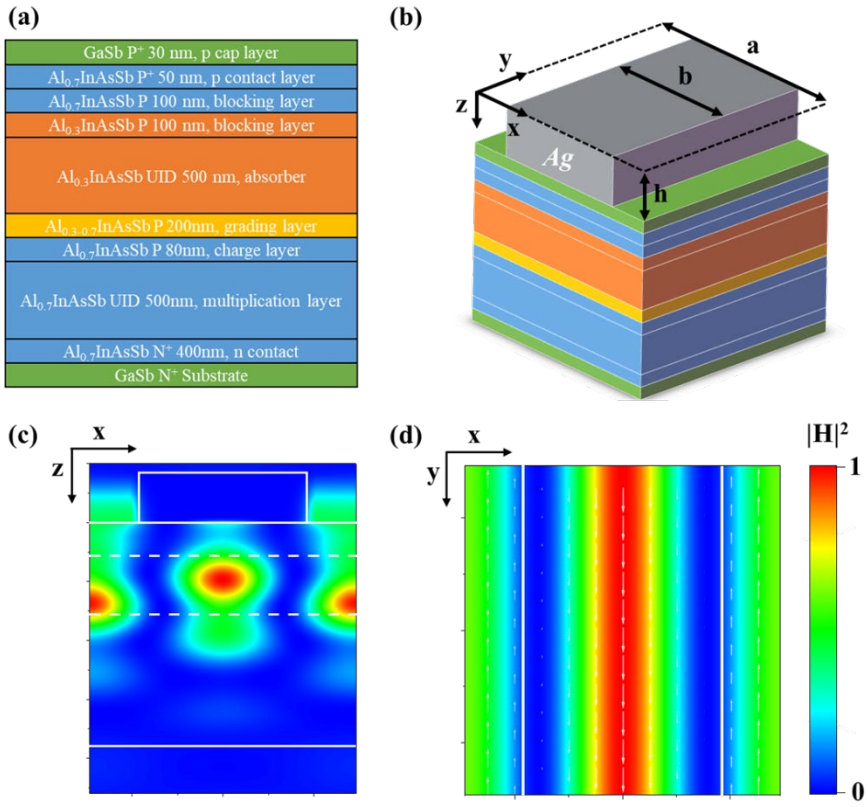

Fig. 2.2-4 (a) Schematic cross-section of the $Al_xIn_{1-x}As_ySb_{1-y}$ SACM APD. (b) One unit cell of the metal grating structure. (c) Normalized distribution of the magnetic field intensity square $|H|^2$ in the x-z plane. The region between the two dash lines represents the intrinsic $Al_{0.3}InAsSb$ layer, and the solid line represents the top of the GaSb substrate. (d) Normalized distribution of the magnetic field intensity square $|H|^2$ in the x-y plane at the center of the resonance peak in the absorber. The white arrows represent the magnetic field vectors and have no z component. The region between two solid lines indicates the position of the metal stripes. Incidence wavelength in (c) and (d) is 2 μm.

Fig. 2.2-5 shows the calculated absorption spectra with metal grating on the surface. A strong absorption enhancement is achieved, where the absorption with the metal grating (~ 65%) is nearly 5 times higher than the bare surface (~ 13%) and 2.5 times higher than the photonic crystal approach (~ 27%). It should be clarified that the absorption calculation here only takes the semiconductor region into account, i.e., from the top of the GaSb contact layer to the GaSb substrate; the metal is not included. The absorption in the metal grating was calculated separately to be less than 5%, which is negligible compared with the absorption in the absorber.

The strong absorption enhancement by the metal grating is the result of multiple effects. First, it is worth noting that with nearly 63% of the surface covered by metal, the calculated reflection is only ~10%, which is much lower than the reflection of a bare GaSb surface (~ 35% at 2 μm). This phenomenon is generally known as the plasmon-enhanced transmission effect of subwavelength metal slits [24-26]. As reported in previous studies [25], periodic subwavelength metal structures are able to assist the coupling of the incident electromagnetic wave into the TEM waveguide modes inside the metal slits, and the far-field transmission can be nearly 100 % with an appropriate grating size. Moreover, the plasmon-enhanced transmission effect is strongly structure dependent. As a result of resonances inside the metal slit waveguides, the peak absorption will reappear periodically with the change of metal thickness. To verify this phenomenon for the metal grating structure, absorption with varying grating thickness was calculated and plotted in Fig. 2.2-6. The absorption peaks repeat periodically with metal thickness, which is consistent with the characteristics of the plasmon-enhanced transmission effect. However, it should be noted that the peak absorption gradually decreases with increasing thickness. This apparently conflicts with previous studies, but in fact, it is reasonable for my device design, i.e., the metal grating here not only provides

transmission enhancement but also gives rise to lateral coupling. Therefore, the thickness to achieve optimal transmission enhancement may not yield the highest coupling efficiency.

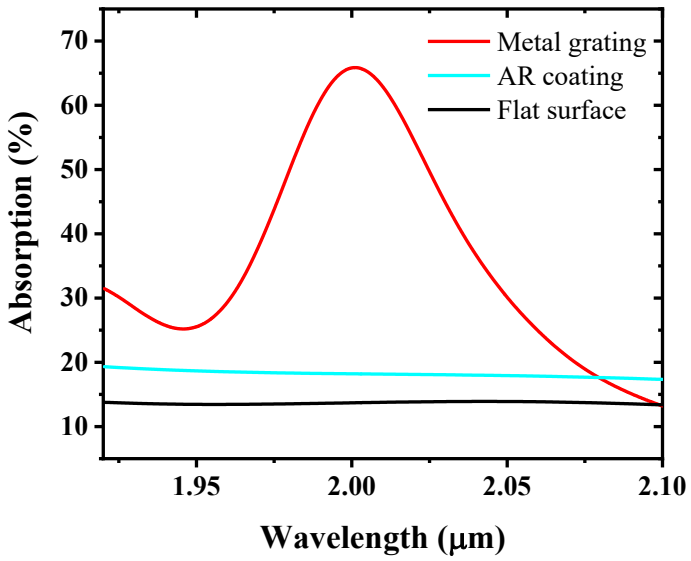

Fig. 2.2-5 Calculated absorption spectra of the device with metal grating, anti-reflection coating, and the flat surface. The anti-reflection coating and flat surface are set the same as in the simulation of photonic crystals. The absorption was calculated from the top of the GaSb contact layer to the GaSb substrate; the metal is not included.

Although the plasmon-enhanced transmission effect exists, it should not be the primary design consideration for high absorption. As shown in Fig. 2.2-5, absorption will be merely increased to about 18 % when a quarter-wavelength-thick AR-coating is deposited on the surface, even though the surface reflection should be close to zero. Consequently, there must be another effect that determines the absorption, which is, in fact, the lateral coupling effect similar to that observed for the photonic crystal approach, i.e., normal-incident light is diffracted by the metal grating and coupled into the laterally-propagating mode in the absorber.

Similar to the photonic crystal, the analysis of the metal grating approach can be separated into to two parts, the resonance mode analysis, and the coupling process analysis. For the resonance mode, the metal grating does not function exactly as the photonic crystal. In the vertical direction (z-direction), the two approaches are similar, i.e., light is confined in the absorber by total internal reflection. It is worth noting that plasmonic modes should be excluded from consideration here because plasmonic modes exist at the interface between metal and semiconductor. Moreover, mode analysis, performed by FDTD simulation, shows that the effective refractive index is 3.41 for the resonance mode in the absorber. This value is between the refractive indices of the $Al_{0.3}InAsSb$ absorber ($n \sim 3.52$) and the $Al_{0.7}InAsSb$ cladding ($n \sim 3.34$), which indicates that the nature of the resonance mode is that of a waveguide. In the transverse direction (x-y plane), the mode profile is influenced by diffraction. Along the x-direction, the effective wavelength of the mode is equal to the grating period, i.e., $\lambda_0/n_{eff} = a$, which is exactly the Bragg diffraction condition for achieving the highest coupling efficiency with a grating coupler. As a result, two intensity centers can be observed in the x-direction, as shown in Fig. 2.2-4 (c). In the y-direction, the field intensity is uniform since no diffraction occurs, and k_y is zero. Thus, the resonance mode generated by the metal grating is merely a waveguide mode, and the metal grating only serves as a coupler.

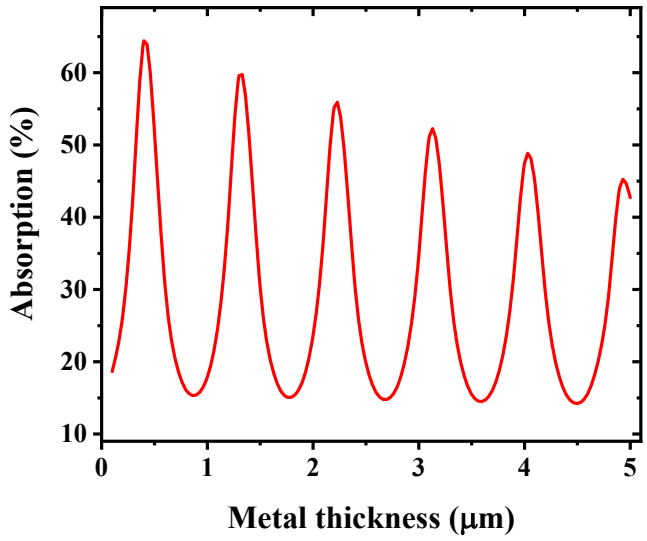

Fig. 2.2-6 The variation of the absorption versus the metal grating thickness.

Even though there are differences in the modes, once coupled, the light will be trapped in the same waveguide structure for both metal grating and photonic crystal. Hence, higher absorption for the metal grating is most probably due to its high coupling efficiency, i.e., the metal grating will couple more light into the resonance mode in the absorber. If the metal grating is replaced by a dielectric (GaSb) grating, the absorption will be much lower and is comparable to that of the photonic crystal. Therefore, the material property of metal is the primary contributor to strong absorption rather than the structural difference. The near-field interaction of the EM-wave with a metal grating has been reported in previous studies [27, 28]. These provide insight for the high coupling efficiency of my metal grating approach. The near field generated by the metal grating is a superposition of two fields, one is a field from the incident plane wave, and the other from dipoles induced at the edges of the metal strips. Since the induced dipole field is strongly localized within the region near the metal, the far-field properties of a metal grating are similar to a dielectric grating. However, in the

near field, the situation is very different. The metal grating induces a much more complicated vector structure than a dielectric grating. The most distinct characteristic is that the electric field is forced to be perpendicular to the metal surface underneath the metal strips, due to the boundary condition of the metal, which requires the electric field to be perpendicular to the metal surface. Therefore, in my simulation with a TEM wave input, the propagation of the light will be almost transverse under the metal strips, as clearly indicated by the Poynting vector distribution in Fig. 2.2-7. Further from the surface, although the direction of the wave vector begins to tilt away from x-direction due to the decay of the induced dipole field, light still has a large transverse component when it reaches the upper edge of the absorber. Such an increase in the transverse component will result in more power being allocated to the non-zero diffraction orders, which ultimately causes more power to be coupled into the absorber slab and less power carried away by zero-order diffraction with transmission to the far-field. Simply put, the near-field radiation influenced by the induced dipoles is more likely to be coupled into the waveguide structure, which is located in the near field rather than being transmitted to the far-field, and this significantly enhances the absorption if the slab material is absorptive.

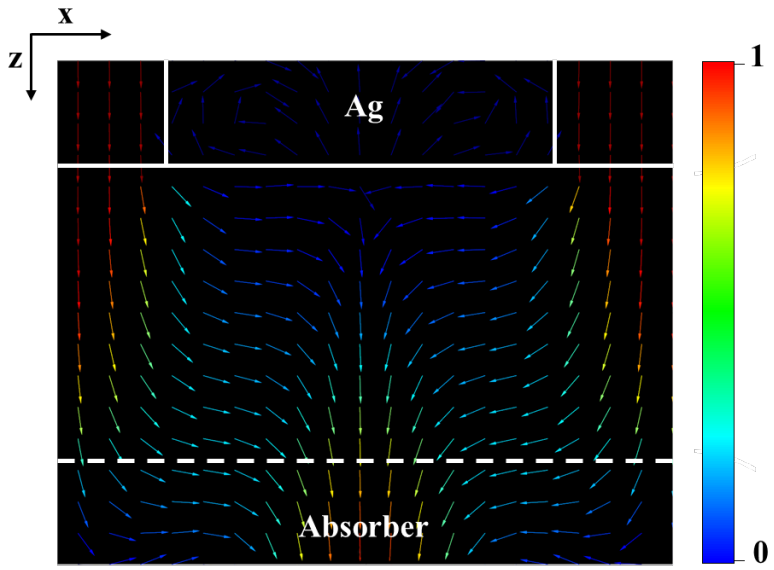

Fig. 2.2-7 Poynting vector distribution under the metal grating in the x-z plane with an incidence wavelength of 2 μm, where the normalized magnitude of the Poynting vector is indicated by the scale bar on the left. The dash line represents the top of the absorber.

It is worth noting that the polarization of the optical input is set to be TM in the simulation. However, the actual polarization may be unpredictable and may significantly affect the coupling efficiency. To investigate the influence of the polarization, the polarization angle is changed by rotating the magnetic field direction of the normal incidence light along the z-axis in the simulation, as illustrated in Fig. 2.2-8 (a). The angle value is defined as the angle to the original magnetic field direction (y-axis). Subsequently, the absorption of different polarization angles was calculated and plotted in Fig. 2.2-8 (b) and Fig. 2.2-8 (c) for the 1D metal grating and the 2D metal grating, respectively. It is clear that the absorption of the 1D grating is dependent of polarization, with a maximum absorption for TM wave and a minimum absorption for TE waves. However, the absorption of the 2D grating is clearly independent of polarization. This is due to the physics of plasmon enhanced transmission, where only the components of the TEM wave whose electric field direction is perpendicular to the metal surface can be coupled into the resonance mode in the metal slit. Therefore, when the polarization deviates from TM, the sum of the perpendicular component of the electric field to the side wall of the 1D grating decreases, and the fraction of light that can benefit from the plasmon enhanced transmission is reduced, with a result that the reflectivity of the grating becomes higher, and the absorption is reduced. On the other hand, the sum of the perpendicular component of the electric field to the side surface of the 2D grating is constant. Thus, the fraction of the light that can benefit from the plasmon enhanced transmission is the same, with a result that the surface reflection does not change and the absorption is independent of polarization. Consequently, in the following, a 2D grating will be considered.

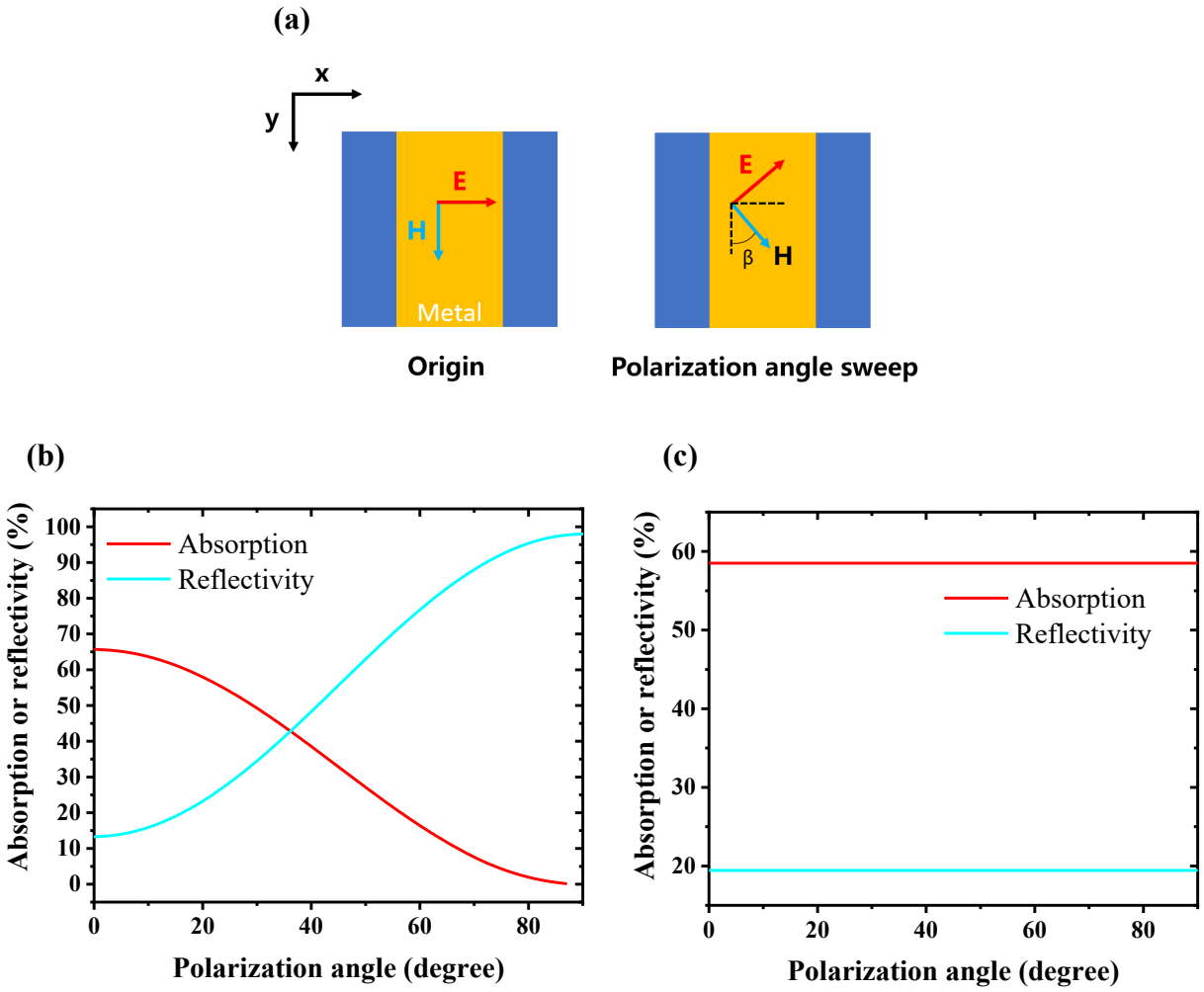

Fig. 2.2-8 (a) Illustration of the polarization angle sweep in the simulation. (b) Absorption and surface reflectivity at 2 μm wavelength of the 1D metal grating with different polarization angles. (c) Absorption and surface reflectivity at 2 μm wavelength of the 2D metal grating with different polarization angles.

Another practical concern for the performance of the metal grating is the incidence angle of the light, which may also significantly affect the coupling efficiency. To investigate this, the incidence angle was changed by rotating the wavevector direction of the incidence light. The angle value is defined as the angle to the surface normal (z-axis), as illustrated in Fig. 2.2-9 (a).

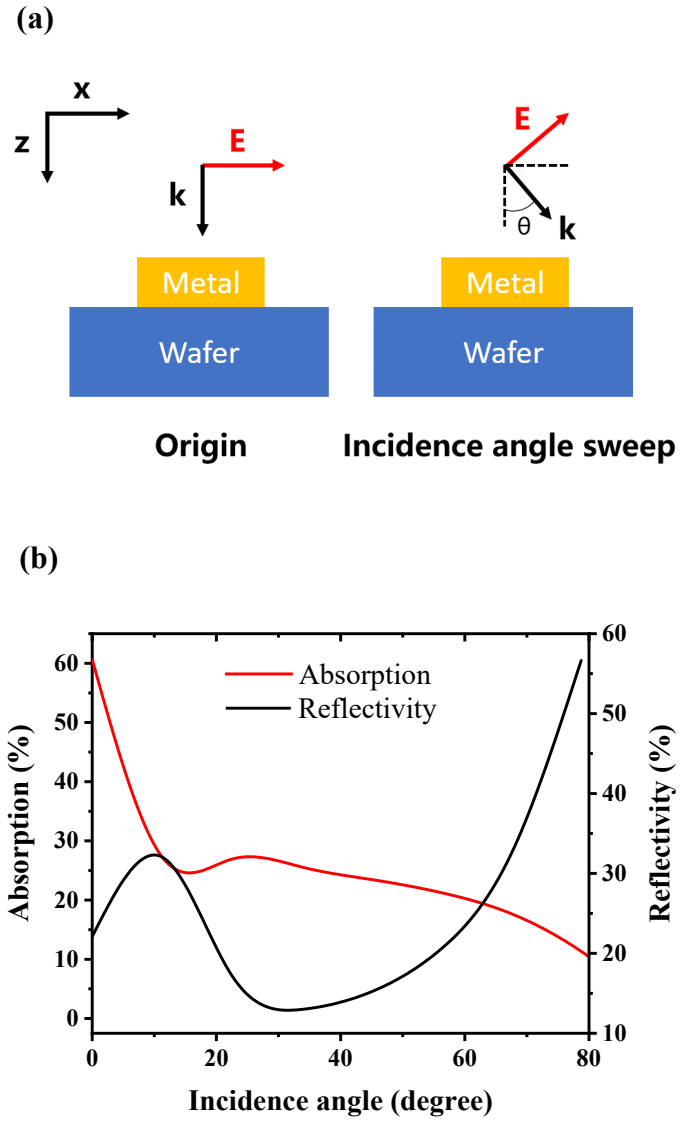

Fig. 2.2-9 (a) Illustration of the incidence and polarization angle sweep in the simulation. (b) Absorption at 2 μm wavelength of the metal grating with different incidence angles.

As shown in Fig. 2.2-9 (b), at high incidence angles, the decrease of the absorption seems to be dominated by increased reflection at the surface, which is similar to the photonic crystal. At low incidence angles, there is a rapid increase in reflectivity and therefore reduced absorption. This is probably due to the fact that the electric field is no longer perpendicular to the metal when the

incident angle deviates from normal. As a result, the plasmonic-enhanced transmission is no longer satisfied. Therefore, incidence angle may need to be carefully controlled.

In summary, two approaches are proposed to enhance the absorption of AlInAsSb SACM APDs for 2-μm detection, along with a thin absorber design. With a triangular-lattice photonic crystal structure, the absorption is enhanced approximately 2 times relative to the bare surface. The enhancement mechanism is primarily increasing coupling of the normal incidence light into the photonic-crystal-slab resonance mode. Significantly stronger absorption, ~ 5 times that of the bare surface, can be achieved with a metal grating on the surface. The high absorption was found to be caused by the high coupling efficiency of the metal grating, which originates from the fact that the near field diffraction of the metal grating has stronger non-zero diffraction order components.

Although based on the simulations, both approaches proposed in this section appear to be effective, the metal grating is projected to be superior for MWIR APDs compared to the photonic crystal. This is not only because the photonic crystal shows lower efficiency from the simulation, but moreover it requires etching air holes into the narrow bandgap absorber which will significantly increase the surface leakage dark current. Therefore, I focused on the metal grating to enhance the efficiency for the 2-μm SACM APDs.

2.3. Device simulation and design

The metal grating structure enables use of a thin absorber to reduce the dark current while keeping a high quantum efficiency. Therefore, the original layer structure of the SACM APD in ref. [8], as shown in Fig. 2.3-1, needs to be modified to satisfy this purpose. The focus of the design is to achieve high quantum efficiency and high bandwidth while minimizing the dark current.

Fig. 2.3-1 Schematic cross section of the SACM APD reported in ref. [8].

The first design parameter is the thickness of the absorber. While a thinner absorber is preferred to minimize the dark current, its thickness should not be less than a half wavelength so as to support a waveguide mode and enable the photon trapping mechanism. Therefore, the theoretical minimum absorber thickness can be estimated by the equation

$$d_{abs} \geq \frac{1}{2} \cdot \frac{\lambda_0}{n} \qquad (2.3-1)$$

where is d_{abs} is the thickness of the absorber, λ_0 is the wavelength in vacuum and n is the refractive index of the absorber material. By substituting the refractive index values in Table 2.2-1, the critical thickness is calculated to be ~ 300 nm in $Al_{0.3}InAsSb$. Therefore, this value was selected for the absorber thickness. It is worth noting that although the absorber thickness is selected at a critical value, the design is still reliable for possible refractive index variations owing to the 100 nm $Al_{0.3\text{-}0.7}InAsSb$ grading layer. In addition to providing bandgap grading, the $Al_{0.3\text{-}0.7}InAsSb$ grading layer also serves as a refractive index buffering layer that can extend the waveguide core region and therefore provide flexibility for refractive index variations in practice.

The second design parameter is the thickness of the multiplication layer. To achieve a high gain-bandwidth product, a thinner multiplication layer is preferred. As shown in Table 2.3-1, the simulated transit-time bandwidth (without consideration of the avalanche built-up time) increases with a thinner multiplication layer. However, to maintain the same gain level in a thin multiplication layer, high bias is needed, and therefore excessive electric field may cause surface break down or even tunneling which will result in low maximum gain. Therefore, by considering the tradeoff between the bandwidth and the maximum gain, the multiplication layer thickness was designed to be 250 μm.

Table 2.3-1 Simulated transit-time bandwidth with various multiplication layer thickness

Multiplication layer thickness (nm)	Transit-time bandwidth (GHz)
100	17.6
200	16.5
300	15.1
400	14.5
500	13.1

The third design parameter is the doping concentration of the charge layer. Generally, high charge layer doping can increase the electric field contrast between the absorber and the multiplication layer, leading to low dark current and high gain. However, high charge layer doping may also result in exceedingly high electric field prior to the punch through voltage. This can cause an early device break-down even before the heterojunction barrier is fully overcome at the charge layer, which may severely limit the quantum efficiency. Therefore, an appropriate charge layer doping is critical. Fig. 2.3-2 shows the simulated electric field profile with different charge layer doping concentrations. The estimated gain at the punch through voltage is calculated based on the electric field simulation and the impact ionization coefficients reported in [29]. The results are listed in Table 2.3-2. We find

that the proper charge layer doping concentration should be around 3×10^{17} cm^{-3}, which can give a moderate gain of ~ 3.5 at punch through voltage.

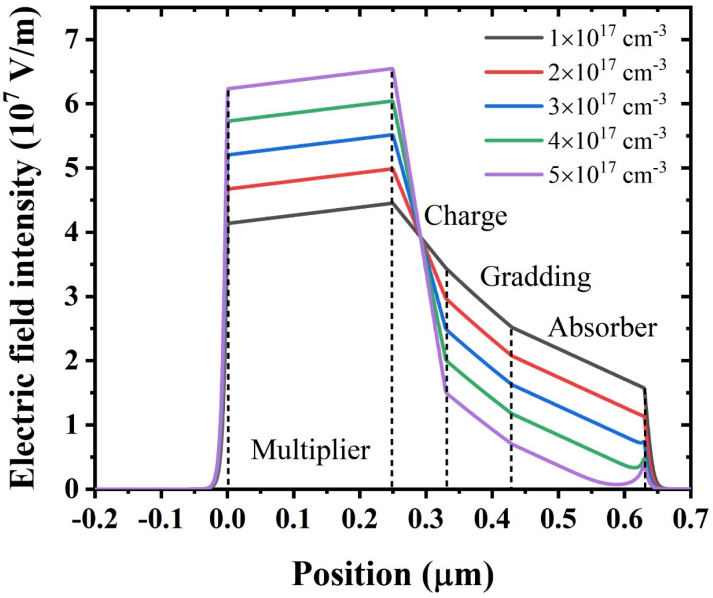

Fig. 2.3-2 Simulated electric field profile with different charge layer doping concentrations.

Table 2.3-2 Simulated punch through voltage, bandwidth, and gain with different charge layer doping concentrations.

Doping concentration (cm^{-3})	Punch through voltage (V)	Transit-time bandwidth (GHz)	Estimated gain (at punch through voltage)
1×10^{17}	-7	16.7	1.02
2×10^{17}	-10	16.6	1.4
3×10^{17}	-13	16.4	3.5
4×10^{17}	-16	16.5	31.3
5×10^{17}	-19	16.1	575.9

In addition to the three major parameters introduced, other optimizations were also addressed to maximize the bandwidth of the device. The Al component of the grading layer was designed to be continuously graded to facilitate electron transit. Fig. 2.3-3 shows the band diagram comparison of a continuous grading layer (Al fraction graded continuously from 30% to 70%) and an abrupt grading

layer (Al fraction graded using an intermediate layer of 50%). The simulated transit-time bandwidth using these two grading layer designs is compared in Table 2.3-3. It is evident that with a continuous grading layer, the transit-time bandwidth is improved more than 2 times. The reason for the improvement can be explained by Fig. 2.3-3, where the bandgap of the grading layer is continuously varied with a continuously graded Al fraction, and therefore the barrier for electron transport is significantly reduced.

Table 2.3-3 Simulated transit-time bandwidth with an abrupt grading layer and a continuous grading layer.

Grading layer type	Transit-time bandwidth (GHz)
Abrupt	16.4
Continuous	30.1

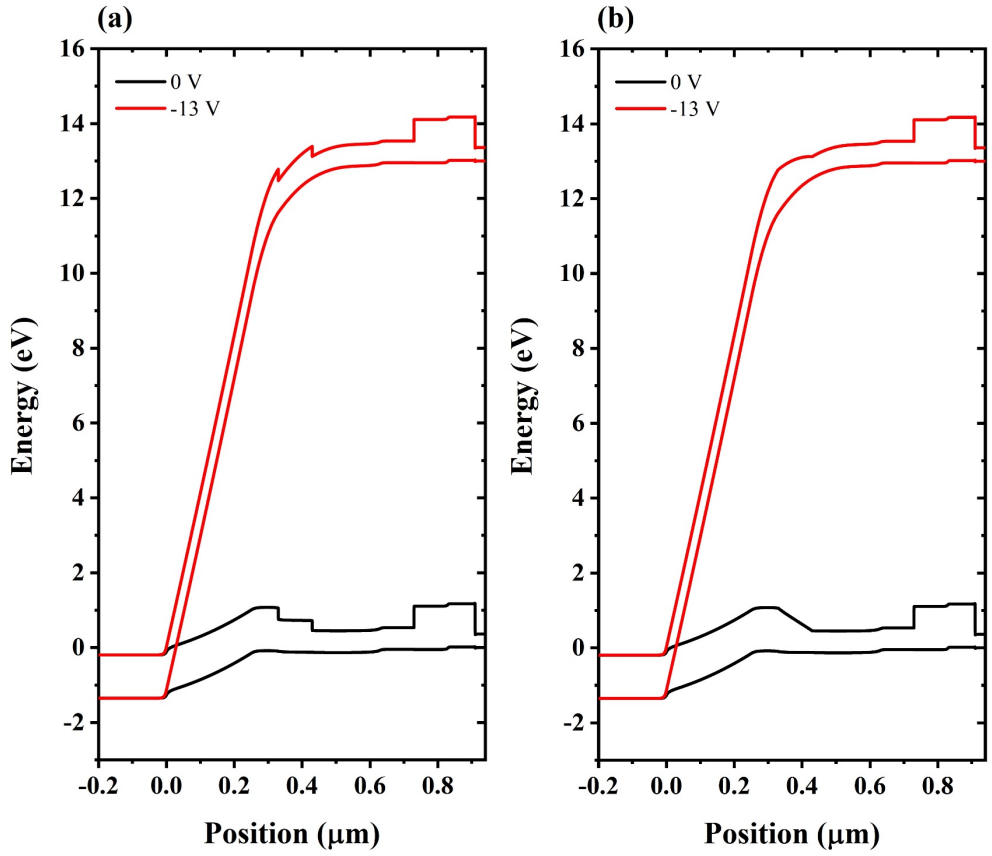

Fig. 2.3-3 Simulated band diagram with (a) an abrupt grading layer and (b) a continuous grading layer at equilibrium and under reverse bias.

In addition to the transit-time bandwidth component, the RC time limit bandwidth is another important contributor to the speed of the device. As expressed by equation $f_{RC} = 1/(2\pi RC)$, low series resistance R is critical for achieving high RC bandwidth. Based on investigations in ref. [20], the metal-semiconductor contact on the N-type $Al_{0.7}InAsSb$ layer with Ti/Au metal stacks is non-ohmic, and the contact resistance can be as large as 3000 Ohms. Therefore, optimizing the N-type contact is important. Various approaches have been attempted to optimize the N-type contact, such as using a GaSb buffer layer as the contact layer, annealing metal contacts on the GaSb buffer layer, and using a narrow bandgap $Al_{0.3}InAsSb$ layer as the contact layer. Fig. 2.3-4 (a) shows the I-V curves measured from transfer link method (TLMs) with the same pad dimensions and distances. It is evident that contacts on $Al_{0.7}InAsSb$ and GaSb layer show non-ohmic characteristics where a large turn-on voltage exists. Annealing contacts on GaSb at 290 ºC for 60 s appears to transform the contact to ohmic, but the TLM current is still lower than that of the contact on a narrow bandgap $Al_{0.3}InAsSb$ layer. To further evaluate each N-contact solution, the series resistance of the device was estimated from the forward biased I-V curve, as shown in Fig. 2.3-4 (b). Consistent with the TLM measurements, using $Al_{0.3}InAsSb$ as an N contact layer gives the lowest series resistance (less than 50 Ohms). This result is reasonable as a narrow bandgap is highly preferred for forming a good ohmic contact on N type semiconductors. Consequently, the $Al_{0.7}InAsSb$ N-type contact layer in the original design [8] was replaced by an $Al_{0.3}InAsSb$ layer to improve the series resistance. Additionally, the top P-type GaSb cap layer was replaced by a thin InAs layer to avoid possible oxidation of GaSb. It is worth noting that the $Al_{0.3}InAsSb$ N contact layer is absorptive, and therefore

photogenerated holes may diffuse back into the multiplication layer and increase the noise of the device. To study this issue, the band diagram of the device with an $Al_{0.3}InAsSb$ N contact layer was simulated and is plotted in Fig.2.3-5. We see that the hole diffusion will be blocked by the large barrier formed at the heterojunction between the narrow bandgap $Al_{0.3}InAsSb$ layer and the wide bandgap $Al_{0.7}InAsSb$ layer. Therefore, using $Al_{0.3}InAsSb$ as a contact layer will not cause a hole injection problem.

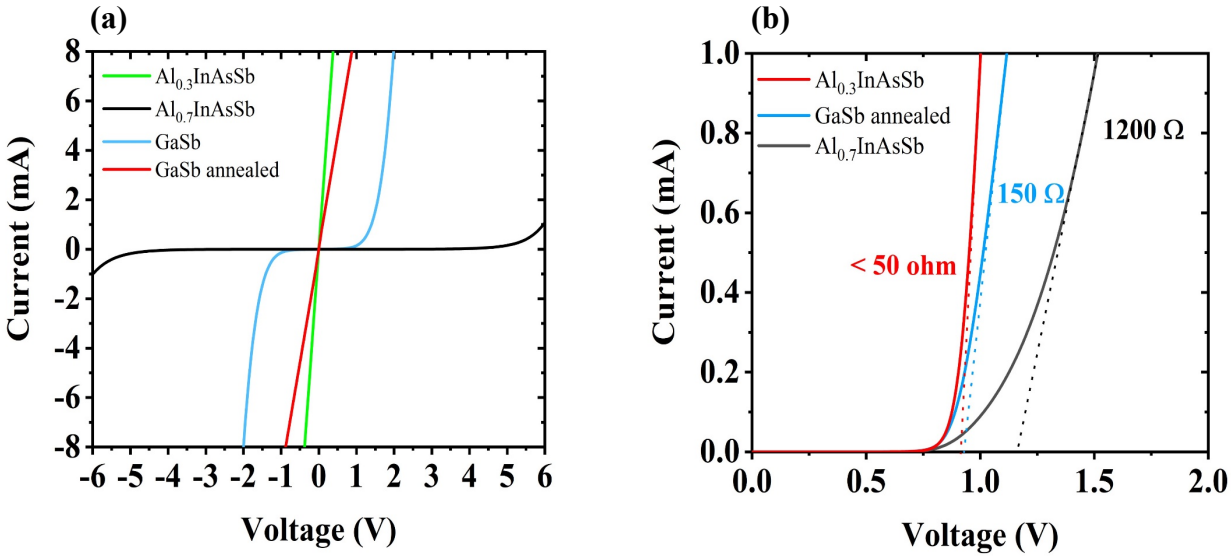

Fig. 2.3-4 (a) I-V curves measured from TLMs with different N type contact layer solutions. (b) forward biased I-V curves of the device and estimated series resistances by using different N type contact layer solutions.

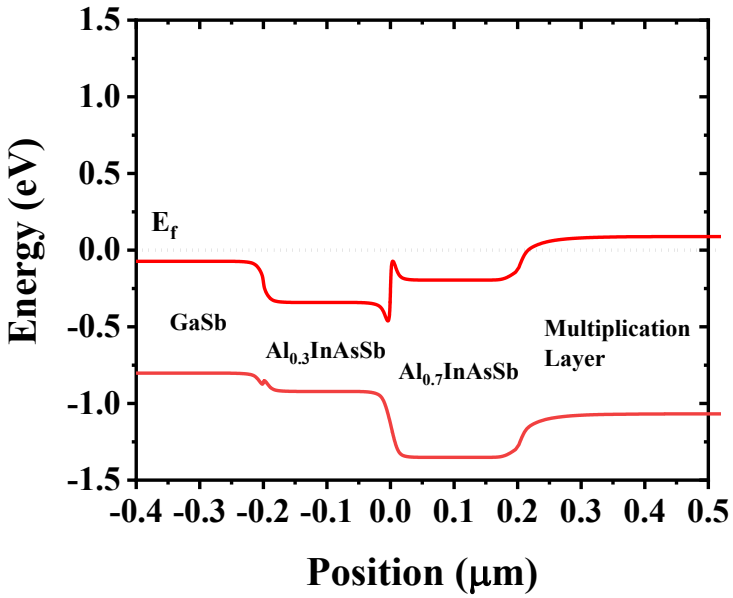

Fig. 2.3-5 Simulated band diagram of the SACM APD with a $Al_{0.3}InAsSb$ contact layer added between the GaSb buffer layer and the $Al_{0.7}InAsSb$ contact layer.

Finally, based on all the optimizations discussed above, the final epitaxy structure of the thin absorber SACM APD was fixed and is shown in Fig. 2.3-6.

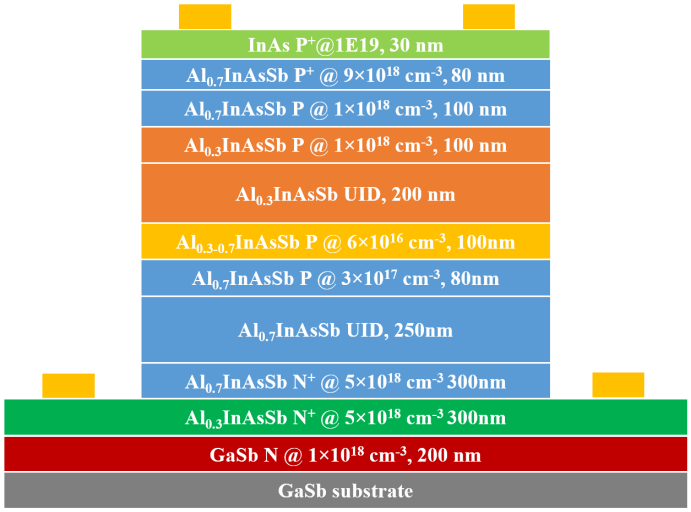

Fig. 2.3-6 Schematic cross section of the designed thin absorber SACM APD.

2.4. Fabrication and characterization

The designed layer structure shown in Fig. 2.3-6 was grown by our colleagues at the University of Texas by molecular beam epitaxy (MBE) as a digital alloy of four binary constituents: AlAs, AlSb, InAs, and InSb lattice matched to an n-type GaSb substrate. I then fabricated devices into circular mesa structures by citric acid wet etching using standard photolithography techniques, and SU-8 was used for surface passivation. A detailed fabrication recipe is listed in Appendix A at the end of this dissertation. Fig. 2.4-1 shows a microscope image of the fabricated devices.

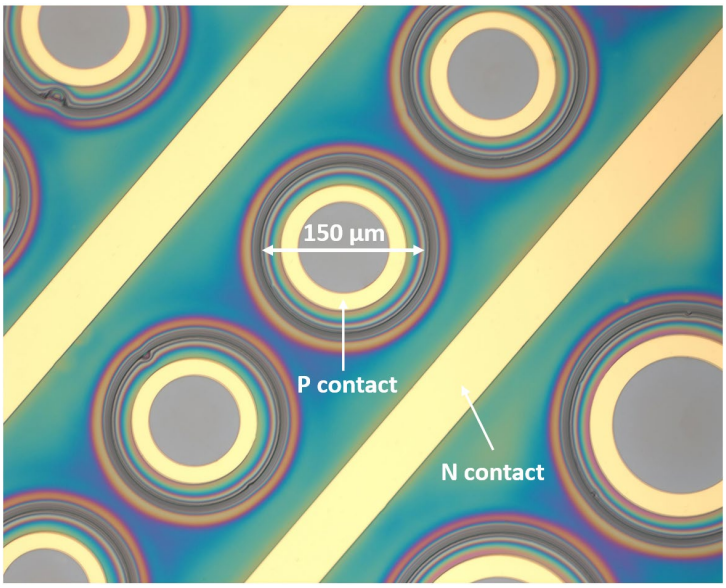

Fig. 2.4-1 Microscope image of fabricated thin absorber SACM devices.

As shown in Fig. 2.4-2, capacitance-voltage curves were measured to verify the operation voltage of the thin absorber SACM APD. The depletion width was estimated using the measured capacitance and the dielectric constant of AlInAsSb [30]. It shows that the charge layer is depleted at ~ -16 V where the electric field reaches into the absorber. It is worth noting that the measured punch through voltage is about 3 V higher than the designed value, which is suspected to be caused by dopant diffusion from the charge layer to the surrounding UID layers.

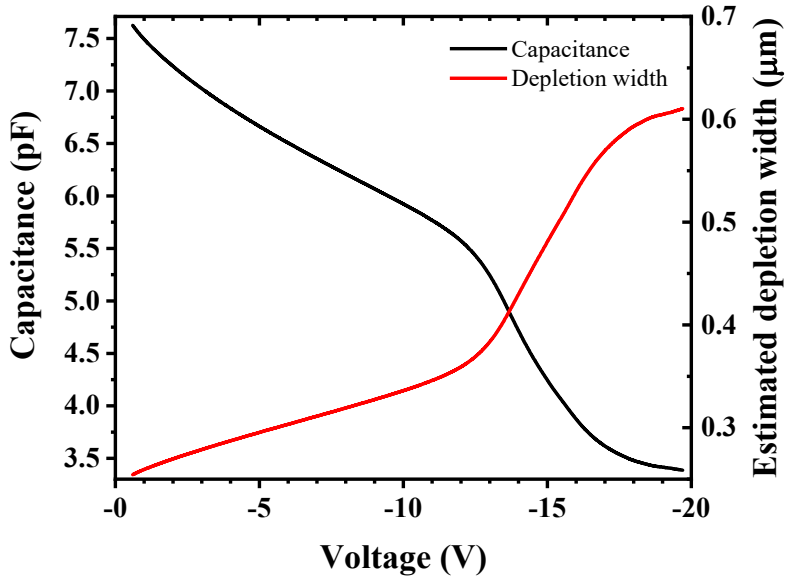

Fig. 2.4-2 measured capacitance-voltage curve of a 150 μm diameter device.

Fig. 2.4-3 (a) shows the room temperature current-voltage (I-V) curves of a 100 μm-diameter device under 2-μm laser illumination. The photocurrent punch through occurs at ~ -16V, consistent with the C-V measurement. It is worth noting that the gain at the punch through voltage is not necessarily unity gain and needs to be fitted by the excess noise measurement. Details regarding the fitting theory and method can be found in ref. [31]. After fitting with the excess noise measurement, the gain at the punch through voltage (-16 V) was determined to be ~ 4. Then, the absolute gain of the device can be calculated by multiplying the fitted gain at -16 V with the relative gain to that at -16 V. The calculated absolute gain curve is plotted in Fig. 2.4-3 (a) as indicated by the right vertical axis. To explore the maximum gain level of the device, the gain curve was also measured at 240 K to reduce dark current and using high optical attenuation to reduce gain saturation. As shown in Fig. 2.4-3 (b), the maximum gain of the device is ~ 1000 at 240 K with low optical intensity.

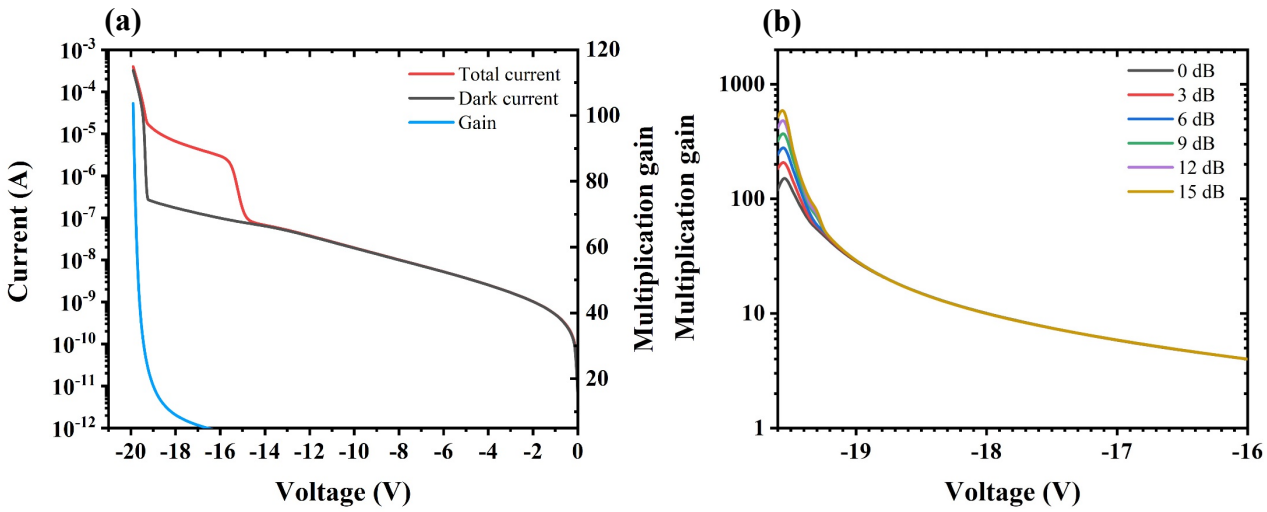

Fig. 2.4-3 (a) Measured current-voltage and gain curve of a 100 μm diameter device at room temperature. (b) Measured gain curves of the device at 240 K with different optical attenuations.

The next important performance characteristic is the excess noise. Fig. 2.4-4 shows the measured excess noise factor F(M) as a function of the multiplication gain M. The theoretical excess noise factors for k values from 0.01 to 0.2 was also calculated using the local-field model [32] and is plotted in Fig. 2.4-4 for reference. Under 2 μm illumination, the measured k value is approximately 0.01, consistent with previously measured AlInAsSb APDs [8, 9]. This value is extremely low compared with conventional III-V semiconductor APDs and is comparable to that of silicon APDs. As a result, the excess noise factor of this device is significantly lower compared to conventional III-V materials such as InP and InAlAs as shown in Fig. 2.4-5.

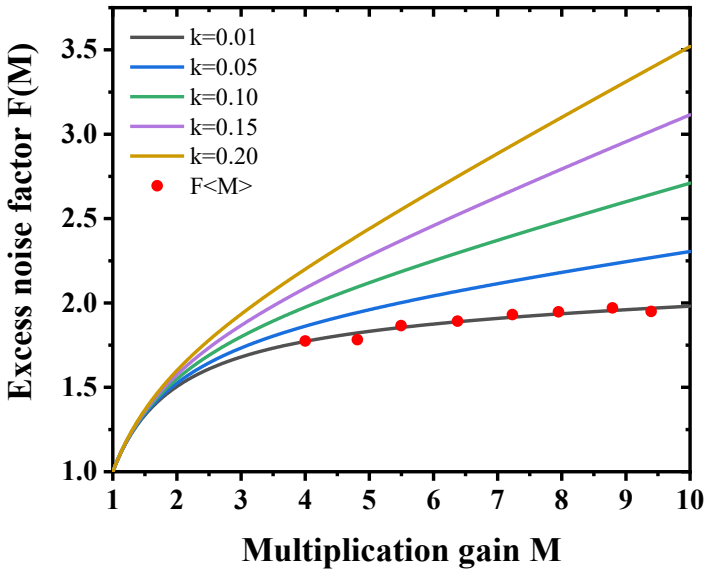

Fig. 2.4-4 measured excess noise factors of a 100 μm diameter device under 2 μm illumination.

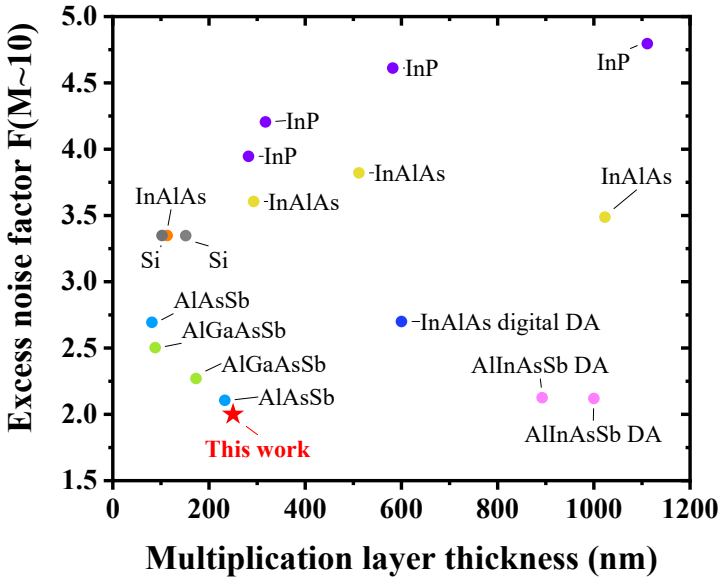

Fig. 2.4-5 Comparison of excess noise factors at gain of ~ 10 for common III-V APDs and Si APDs.

For the dark current performance, it is worth noting that the dark current curve shown in Fig. 2.4-3 (a) does not have an obvious punch through characteristic, i.e., there is no obvious increase in dark current after the electric field extends into the absorber. This indicates that the leakage in the narrow bandgap absorber is nearly comparable to that in the wide bandgap multiplication layer. Compared with the thick absorber design in ref. [8] where the dark current shows an obvious increase (~ 100 times higher) after the punch through, the absence of the dark current increase at the punch through indicates a significant suppression in the dark current by the thin absorber design. To further evaluate the dark performance, temperature dependent dark current density is shown in Fig. 2.4-6. A reference (dashed line) to a state-of-the-art HgCdTe APD [33] and an AlInAsSb APD [8] is also included for comparison. It is evident that the operating temperature of the thin SACM APD reaches ~ 135 K higher than the state-of-the-art HgCdTe APD [33] and even ~ 40 K higher than the AlInAsSb APD with a 1 μm thick absorber [8].

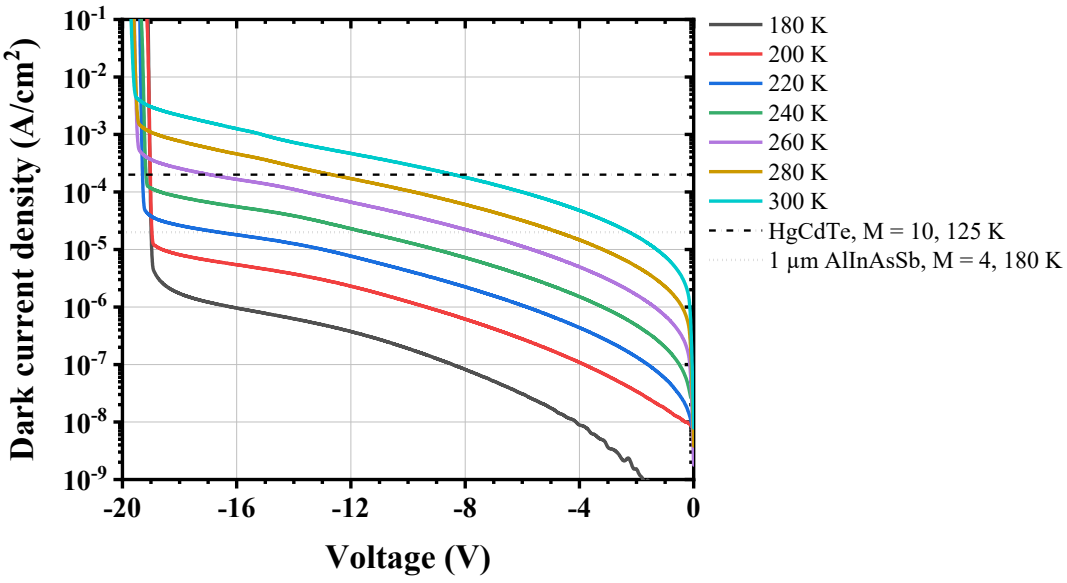

Fig. 2.4-6 Measured dark current density at various temperatures and reference curves of state-of-the-art HgCdTe APD [33] and AlInAsSb SACM APD [8] at 2 μm.

While the thin absorber SACM APD shows a high gain and low noise due to the largely suppressed dark current and low k value, there is a possible issue of low quantum efficiency that results from the very thin absorber, and this will limit the improvement in SNR performance. To verify this, the external quantum efficiency (EQE) was measured under surface-normal illumination. As shown in Fig. 2.4-7, the EQE at 2 μm is ~ 7%. The low EQE is consistent with the simulation. Nevertheless, as noted in section 2.2, efficient absorption enhancement approaches can be applied to boost the EQE to be comparable or even higher than the thick absorber design, and this will be discussed in the next section.

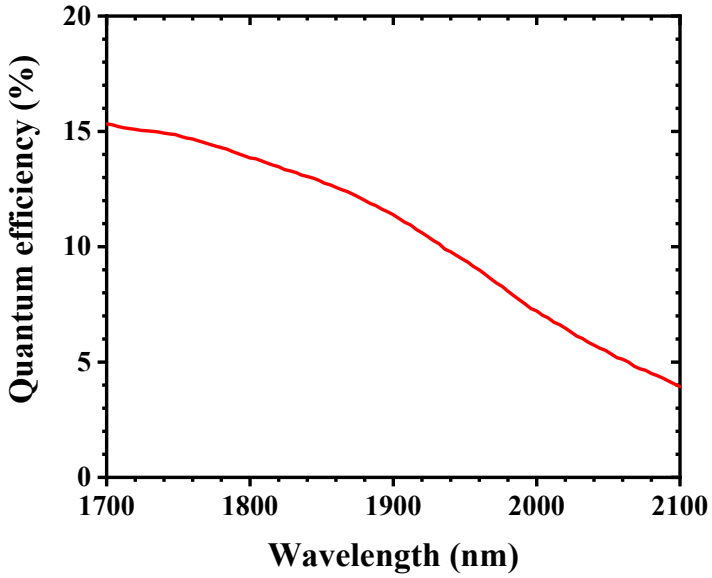

Fig. 2.4-7 Measured external quantum efficiency of a 150 μm diameter device at room temperature.

2.5. Quantum efficiency enhancement

2.5.1. Metal grating

As discussed in section 2.2, the metal grating is a promising approach to enhance the quantum efficiency of the thin absorber SACM APD. The metal grating was redesigned to satisfy the new

layer structure that has been designed in section 2.3. Fig. 2.5-1 shows the revised metal grating dimensions in one unit cell, and the simulated electric field profile and quantum efficiency spectrum are plotted in Fig. 2.5-2 (a) and (b), respectively. With these ideal dimensions, the EQE of the device could be improved to ~ 38 % at 2 μm, which is 6 times higher than a bare surface and is even 8 % higher than a 1 μm-thick absorber with an AR coating. Nevertheless, the actual dimensions of the grating may differ from the design values after fabrication, and the actual EQE would be lower. Therefore, to investigate the fabrication tolerance, EQE with grating dimensions differing from those of the ideal grating were simulated. The result is shown in Fig. 2.5-3 and will be used as the reference for the discussion after the grating fabrication and measurement.

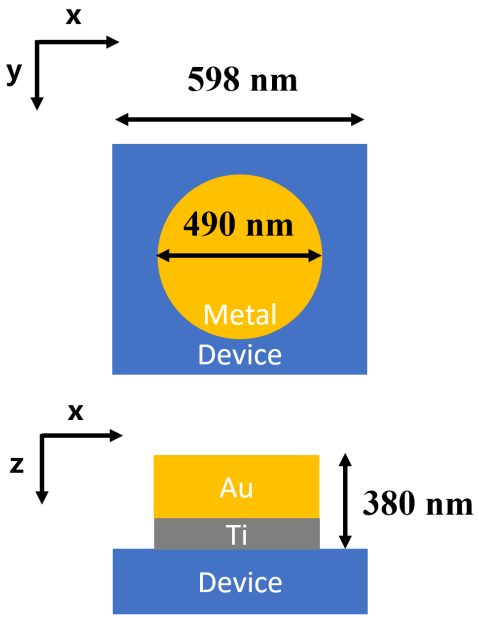

Fig. 2.5.1-1 Optimal dimensions of the metal grating in one unit cell.

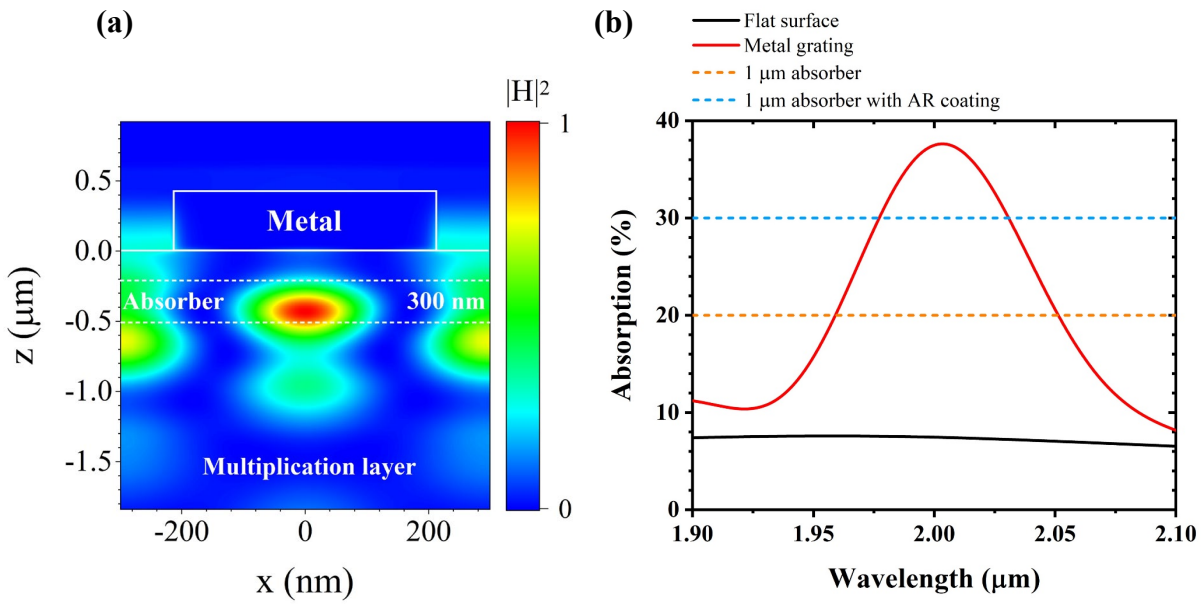

Fig. 2.5.1-2 (a) Simulated magnetic field profile at 2 μm and (b) absorption spectrum with the optimal grating dimensions.

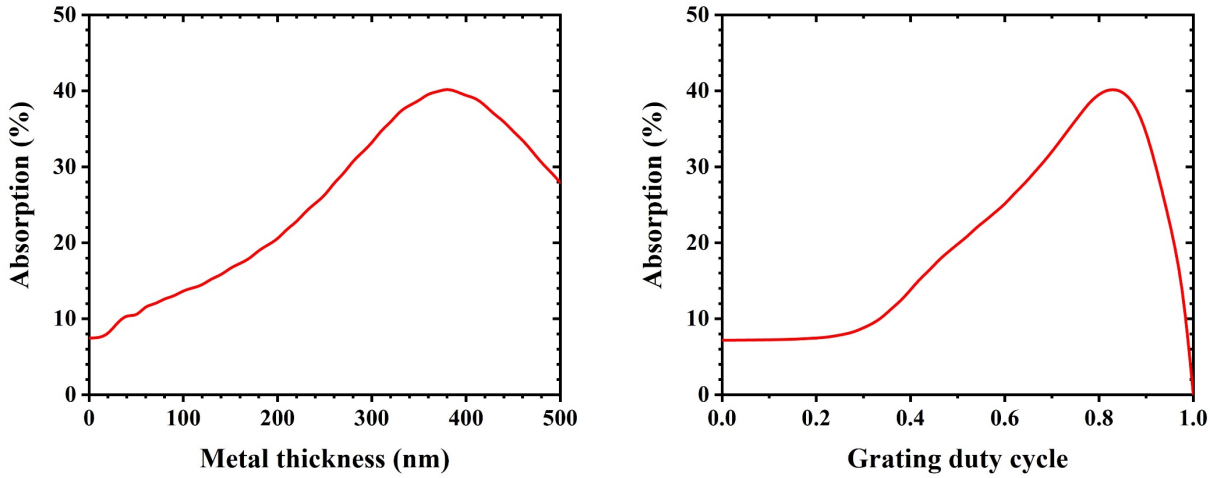

Fig. 2.5.1-3 Simulated absorption efficiency with different metal thicknesses and grating duty cycles.

In the following part of this section, the path of optimizing the fabrication recipe for the sub-micron metal gratings will be presented. Regarding the detailed step-by-step fabrication recipe and parameters, they are listed in the Appendix B and Appendix C at the end of the dissertation.

The dimensions of the metal grating are sub-micrometer in scale, which is beyond the resolution of the conventional lithography in our cleanroom. Instead, electron beam lithography is needed. For the work in this dissertation, a RAITH 150-2 e-beam writer system was used. Its minimum feature size is ~ 2 nm. More information regarding this system can be found in ref. [34]. Typically, e-beam lithography requires special photoresist (PR) that is different from optical lithography, among which PMMA (polymethyl methacrylate) is the most widely used. PMMA is a high resolution and thermally stable photoresist that is well-suited for e-beam exposure. It is usually provided in different dilutions for different PR thicknesses. I used two PMMA dilutions, one was PMMA 950 A4 for thin PR films, and the other one was PMMA 495 A11 for thick films. The thickness of these two PMMA resists at different spin speeds are listed in Table 2.5.1-1. More information regarding the PR thickness can be found in the factory datasheet [35].

Table 2.5.1-1 Thickness of PMMA photoresist with different spin speed

Spin speed	PMMA 950 A4	PMMA 495 A11
2000 rpm	~ 280 nm	~ 1400 nm
4000 rpm	~ 200 nm	~ 1200 nm
6000 rpm	~ 150 nm	~ 850 nm

Since e-beam lithography is highly sensitive to exposure time, careful dose tests are needed before the fabrication. To begin with, I performed dose tests on a thin PR layer. PMMA was spun on a polished silicon wafer at a speed of 4000 rpm and then soft baked on a hot plate at 180 ^{o}C for 90s. The PR thickness after baking was measured to be ~ 200 nm. Then, the e-beam exposure was performed on the photoresist with 30 keV e-beam energy, and the dose was varied from 10 uC/cm^2 to 100 uC/cm^2. The exposed sample was then developed for ~ 40 s using the MIBK (Methyl Isobutyl

Ketone) developer diluted by IPA (MIBK : IPA = 3 : 1). After characterizing under the scanning e-beam microscope (SEM), the correct dose was found to be ~ 45 μC/cm^2; the developed PR pattern is shown in Fig. 2.5.1-4 (a). Subsequently, a thin metal layer stack consisting of 10 nm Ti and 40 nm Au was deposited on the sample. Then, the sample was dipped in NMP (1-Methyl-2-pyrrolidinone) solution and heated to 70 ^{o}C to lift off the metal deposited on the PR. It is worth noting that although an ultrasonic bath may speed up the lift-off process, it may break the small grating patterns and thus should be avoided. After ~ 30 min, the metal was fully lifted off and the residual pattern is shown in Fig. 2.5.1-4 (b).

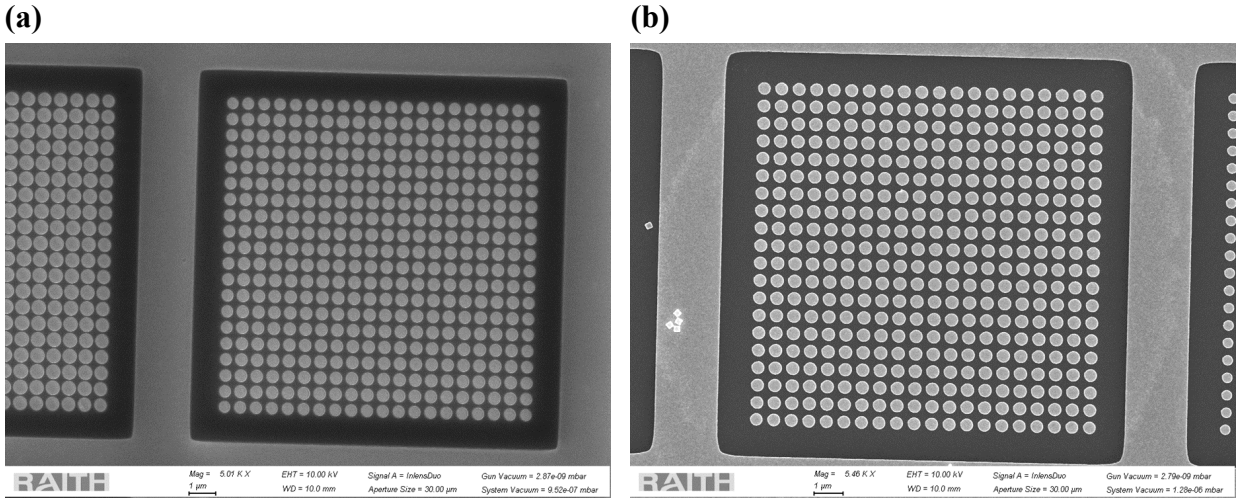

Fig. 2.5.1-4 Test grating patterns (a) on a thin PMMA layer after development and (b) after thin metal deposition and lift-off; The e-beam energy is 30 keV and the exposure does is 45 μC/cm^2.

So far, the dose and the metal lift-off test were successful on a thin PMMA layer. However, to lift off the designed 380 nm thick metal gratings, a much thicker photoresist is required. The reason for this is that the metal may be deposited on the side wall of the PR, and therefore to avoid adhesion of the sidewall metal to the bottom metal, a much thicker PR is needed. Generally, the rule of thumb for lift-off using a single PR layer is “1: 3”, which means that the PR needs to be at least three times

thicker than the metal to support a reliable lift-off. Therefore, for the designed 380 nm-thick metal grating, a photoresist layer of ~ 1.2 μm is needed. As shown in Table 2.5.1-1, PMMA 495 A11 dilution can provide PR thicknesses from 0.8 μm to 1.5 μm, therefore it was selected for the fabrication. The thick PMMA was spun on a polished Si sample with the same speed and baking process as used for thin PMMA. The PR thickness after baking was measured to be ~ 1.2 um, which is, in theory, enough to lift off a 380 nm-thick metal. Based on the design shown in Fig. 2.5.1-1, a metal stack consisting of 10 nm Ti and 370 nm Au was deposited on the sample, and the same lift-off process was performed. Fig. 2.5.1-5 (a) shows the metal grating features after lift-off. Unfortunately, most of the grating pattern fell off. The reason was revealed by the high resolution SEM image shown in Fig. 2.5.1-5 (b), which indicates that the metal was actually deposited on the residual photoresist and therefore was taken off together with the PR. Therefore, it appeared that the thick photoresist was not fully exposed by the e-beam, which resulted in the residual photoresist after development. In fact, this is an intrinsic drawback of the e-beam lithography because the scatting of the electrons will limit its injection length. The best way to solve this problem is to use higher e-beam energy which can increase the injection length of electrons before severe scattering occurs. However, the highest e-beam energy that can be provided by the RAITH 150-2 is 30 keV, which was the energy that was used. Nevertheless, there remains an alternative, i.e., reducing the thickness of the photoresist to make it fully exposed. To try this solution, the spin speed for the PR was increased from 6000 rpm to 8000 rpm, and correspondingly the PR thickness was reduced to ~ 700 nm. Fig. 2.5.1-6 (a) shows the fabricated metal grating using the thinner photoresist. It is evident that most of the grating pattern survived after lift-off, which is as expected from a thinner PR. However, a new problem arose in that some metal on the PR layer was not lifted off even with the help of ultrasonic bath. As shown in Fig. 2.5.1-6 (b), the problem was found to be caused by sidewall

deposition and so that the metal deposited on the PR layer was connected to the bottom grating pattern.

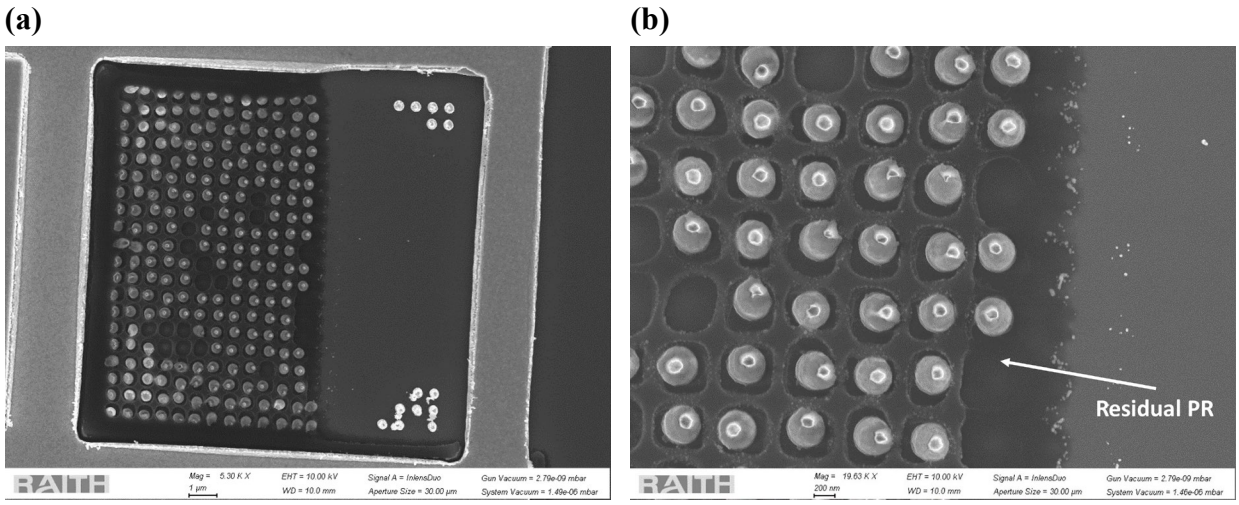

Fig. 2.5.1-5 Metal grating pattern after lift-off using a ~ 1.2 μm thick PMMA layer.

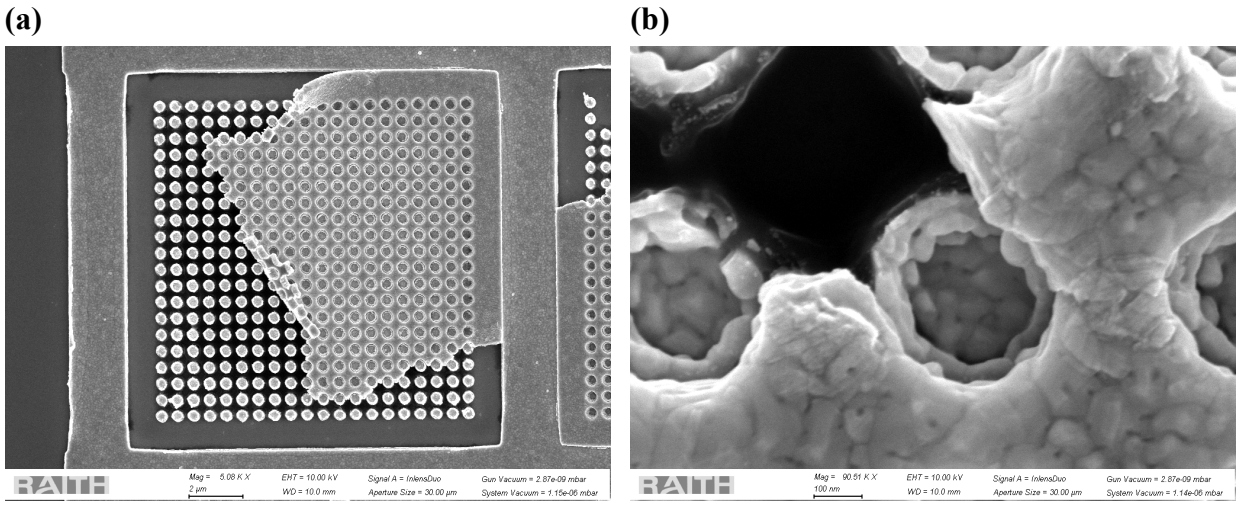

Fig. 2.5.1-6 Metal grating pattern after lift-off using a ~ 0.7 μm thick PMMA layer.

Therefore, lifting off the thick metal that is required for the grating appears to be very difficult. As illustrated in 2.5.1-7 (a), metal cannot be lifted off due to the adhesion of the sidewall metal if the PR layer is too thin. However, if the PR layer is thick, fabrication is still not feasible because the

PR cannot be fully exposed due to the electron scattering, as shown in 2.5.1-7 (b). There seemed to be no appropriate PR layer thickness that can work for the designed metal thickness. While this challenge comes intrinsically from the limited e-beam energy which seemed unsolvable, I developed another fabrication recipe that used a double layer lift-off. A typical process flow for double layer lift-off is shown in Fig. 2.5.1-8. First, two photoresist layers are spun onto the sample in sequence. The bottom layer is PMGI, which functions as undercut layer, and the top layer is PMMA, which is used as imaging layer. Then, the grating pattern is exposed on the thin PMMA imaging layer by e-beam lithography and is then developed by MIBK. It is worth noting that the MIBK developer does not attack the underlying PMGI layer, i.e., the development process is selective. After the imaging layer is developed, PMMA will work as a mask for the following etch step. As shown in Fig. 2.5.1-8 step 4, the lower PMGI layer is then wet etched by TMAH 0.26 N developer which does not attack the top PMMA layer. Therefore, using a selective wet etch process, an undercut structure with controllable length (through different etch times) can be created, and as a result, the adhesion of the side wall metal can be effectively prevented. Compared with the single layer lift-off, the double layer lift-off is superior for thick metal because: a. only a very thin PMMA layer is needed, so that the PR layer can be fully exposed even with low e-beam energy; and b. the complete absence of the sidewall adhesion can create an exceptionally clean pattern.

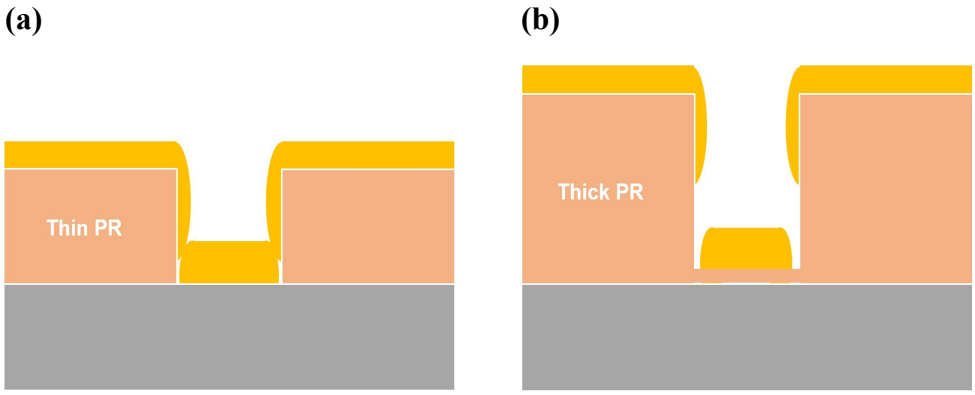

Fig. 2.5.1-7 Illustration of the challenge while using (a) a thin PR layer and (b) a thick PR layer to lift off thick metal by a single PR layer.

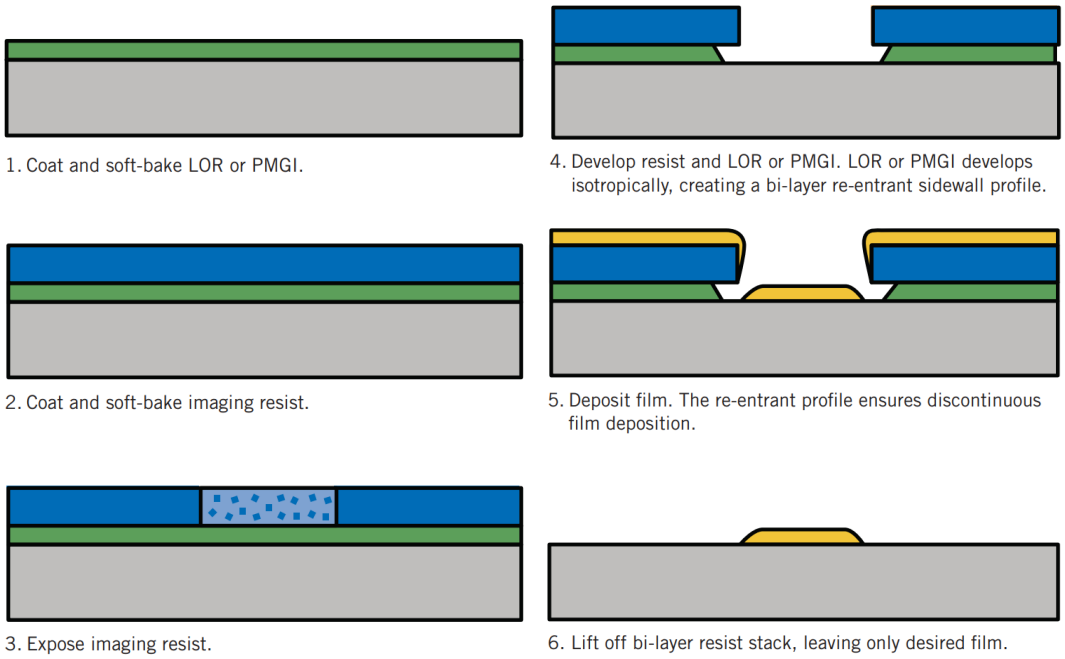

Fig. 2.5.1-8 General process flow of double layer lift-off [36].

Fig. 2.5.1-9 shows the grating pattern after the double layer lift-off. Unfortunately, the photoresist in the center region collapsed, and as a result, the metal on the PR stuck to the bottom grating and could not be lifted off. SEM images shown in Fig. 2.5.1-10 reveals the reason for the PR collapse. The undercutting of the bottom PMGI layer was excessive during the wet etch, causing the top PMMA layer to collapse due to insufficient mechanical support. One straightforward way to solve this problem is to reduce the wet etch time, and therefore the undercut length will be shorter. However, this solution is not feasible for thick metal lift-off because the wet etch of the PMGI layer is isotropic. As a result, the final undercut length will be equal to the thickness of the PMGI layer regardless of the etch time. Since the thickness of the PMGI layer needs to be at least the same as the metal layer, the final undercut length will be ~ 380 nm on each side and ~ 760 nm in total, which

is even larger than the lateral dimension of the grating (< 600 nm). It follows that the bottom PMGI layer will be totally removed, and the top PMMA layer will have no mechanical support.

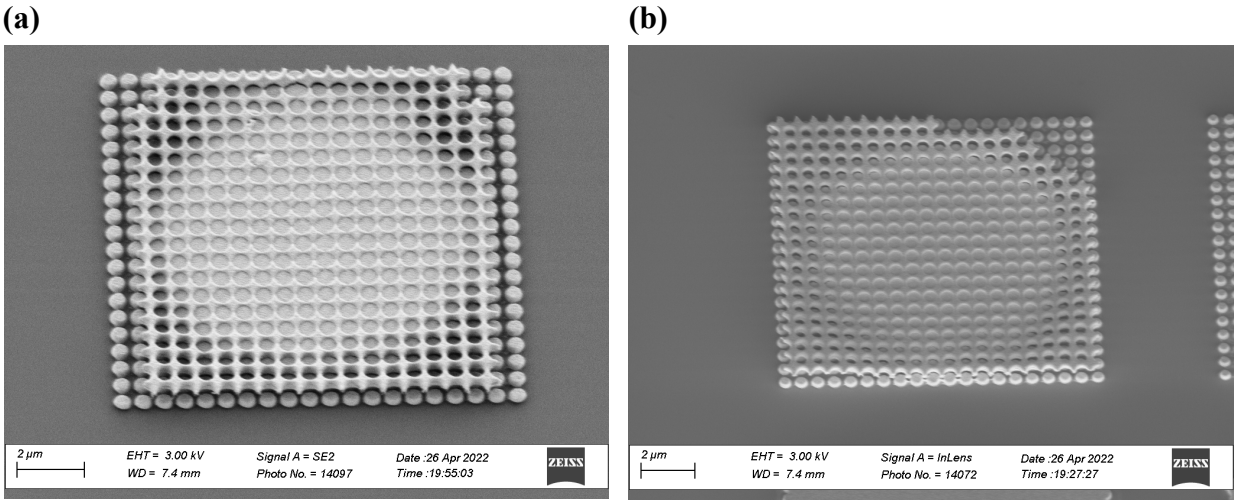

Fig. 2.5.1-9 Collapsed pattern after the double layer lift-off.

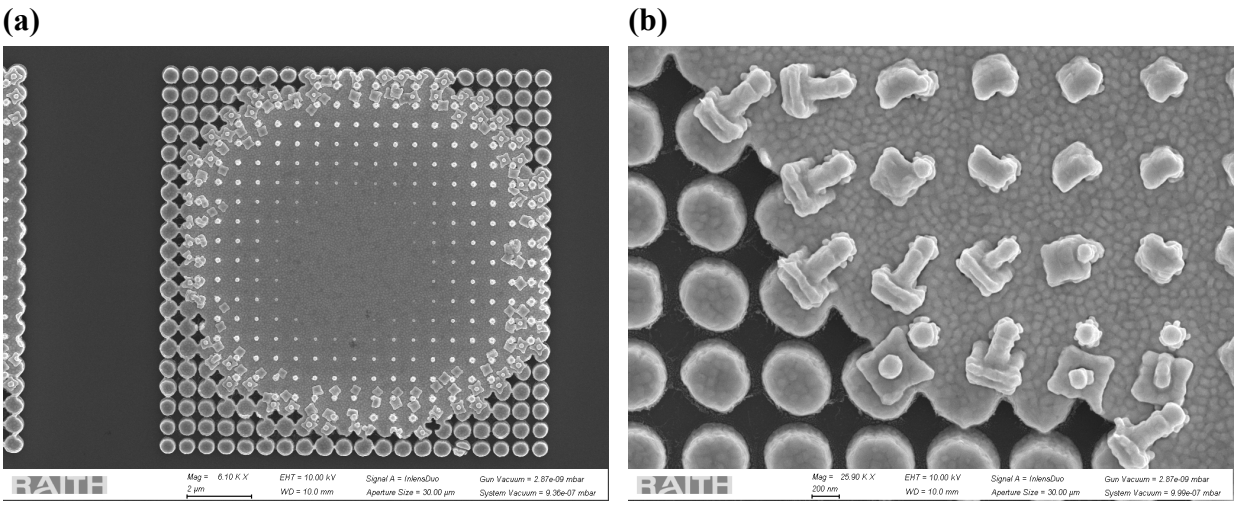

Fig. 2.5.1-10 Over-undercut structure shown in the collapsed pattern region after the double layer lift-off.

Therefore, the problem of using the double layer process to lift off thick metal cannot be avoided as long as the wet etch of the PMGI layer is isotropic. The key issue is how to make the wet etch anisotropic. To achieve this, I developed a new lithography recipe using the combination of high e-

beam energy, dose and short wet etch time. As shown in Fig. 2.5.1-11, a high energy e-beam was used to expose the imaging PMMA layer with an excessively high dose, which can minimize the electron scattering in the PMMA layer and inject the electrons into the bottom PMGI layer with sufficient energy. Therefore, the polymer chains of the PMGI will be broken by the high-energy electrons. This results that the etch rate in the exposed region is faster than the lateral surrounding regions, i.e., an anisotropic etch is achieved. Fig. 2.5.1-12 shows metal grating patterns achieved after using the optimized double layer e-beam lithography. It is evident that with the anisotropic etch and the reduced undercut length, almost all the grating patterns survive after lift-off, and the edge of the grating is exceptionally clean due to the absence of the side wall metal adhesion.

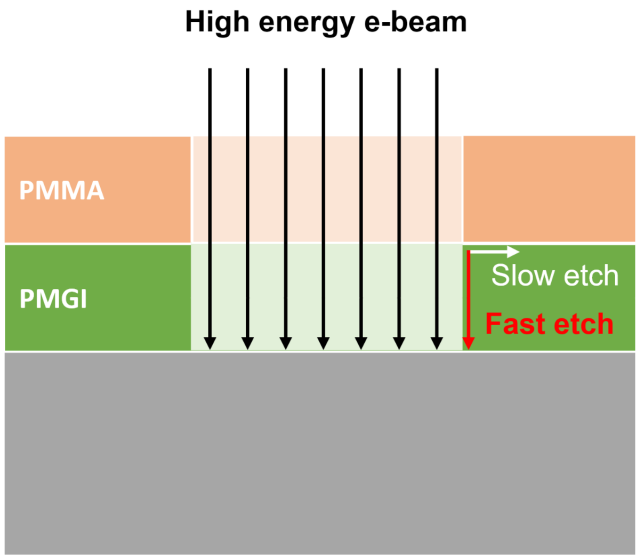

Fig. 2.5.1-11 Illustration of the optimized e-beam lithography process for lifting off thick metal by double photoresist layer.

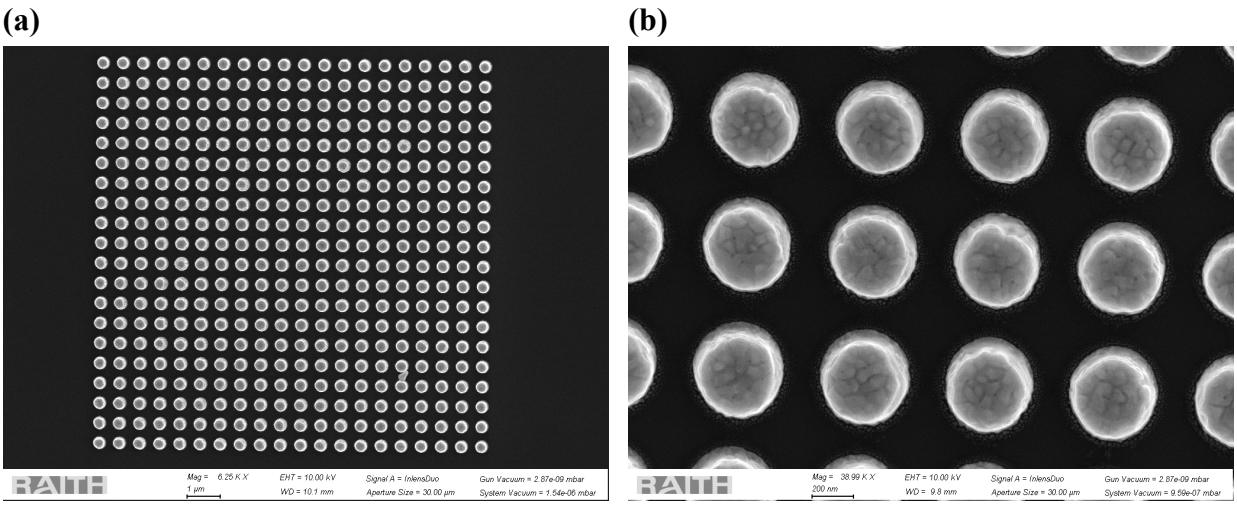

Fig. 2.5.1-12 Metal grating patterns fabricated by the optimized e-beam lithography for double layer lift-off.

Once metal gratings with designed dimensions have been successfully demonstrated, the next step was to fabricate the metal gratings on the top of the APD mesa. The fabrication flow, shown in Fig. 2.5.1-13, consists of the following: (a) fabricate metal gratings by e-beam lithography; (b) expose mesa patterns by normal optical lithography with alignment to the gratings region; (c) etch the mesa; and (d) deposit metal contacts. However, lifting off metal gratings over a large area appears to be very difficult. As shown in Fig. 2.5.1-14, more than half of the grating region was not lifted off even with the help of an ultrasonic bath. This is due to the large area of the grating region. For the dose test patterns, the grating region was 10 μm × 10 μm, but that on the actual mesa is 100 μm × 100 μm. Therefore, the metal patterns connect together over a large area and form a solid aggregate, which made the lift-off more difficult. To solve this problem, I produced a mask design by breaking the large area grating to discrete small blocks with gaps added between, as shown in Fig. 2.5.1-15. It is worth noting that the gap between the blocks is an integer multiple of grating spacings. Therefore, the overall periodicity of grating is unchanged so that the coupling efficiency can, to a large extent, be maintained. Fig. 2.5.1-16 shows the comparison of the large area grating patterns

with and without introducing periodic gaps. It is evident that the fabrication yield of the gratings is significantly improved.

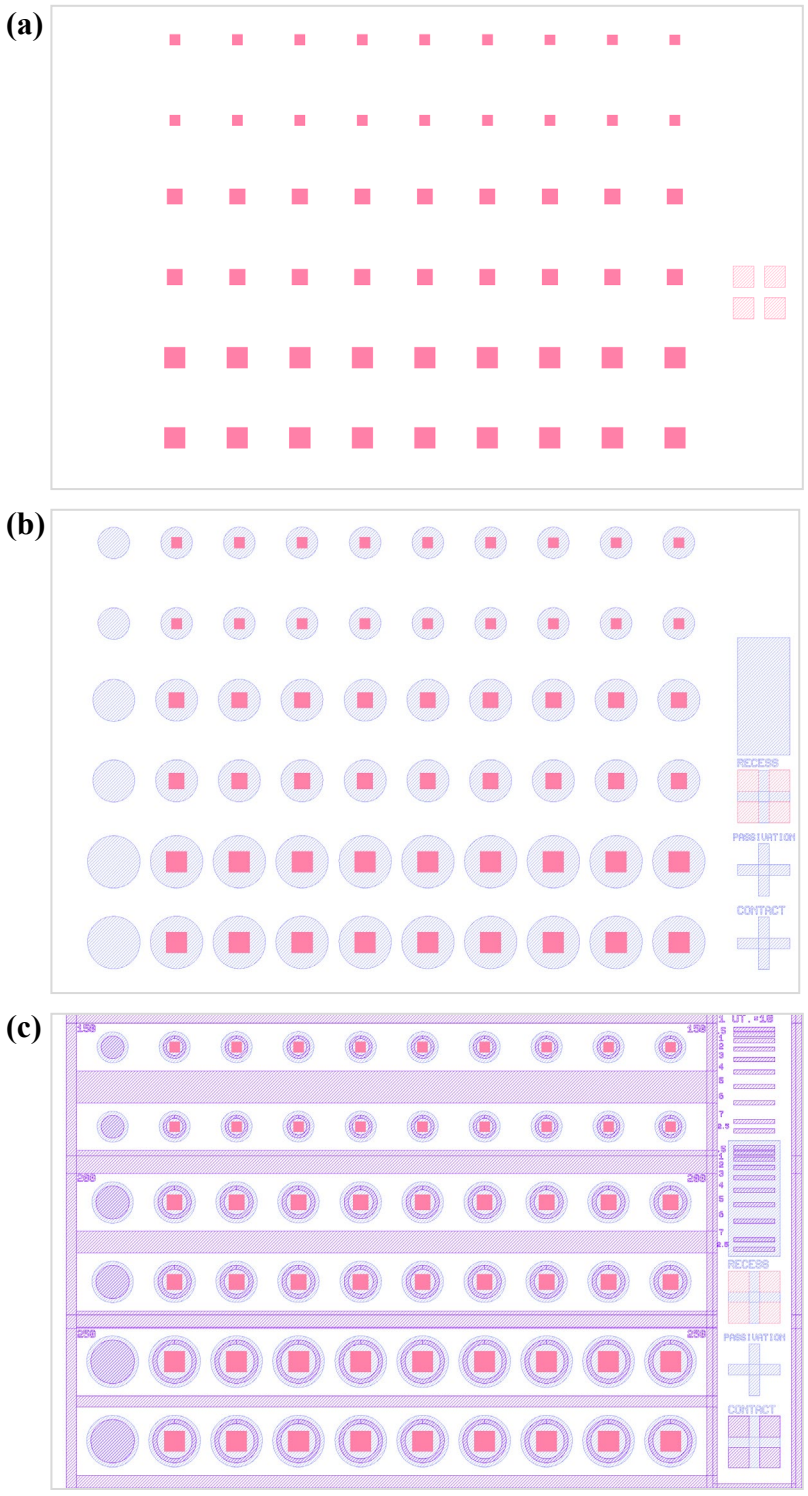

Fig. 2.5.1-13 Process flow for fabricating metal gratings on the top of APD devices.

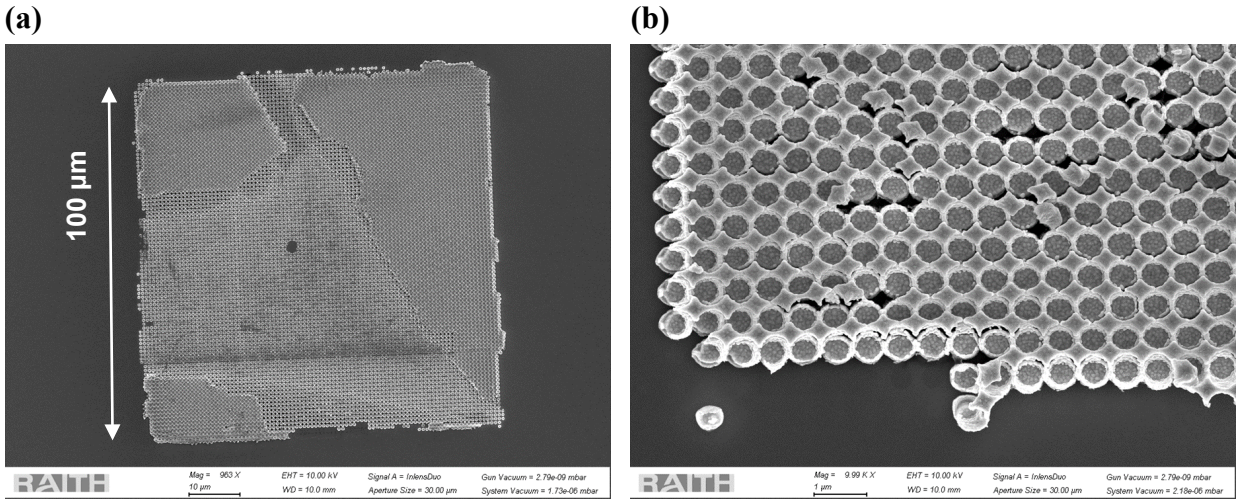

Fig. 2.5.1-14 Lift-off problem for large area metal gratings.

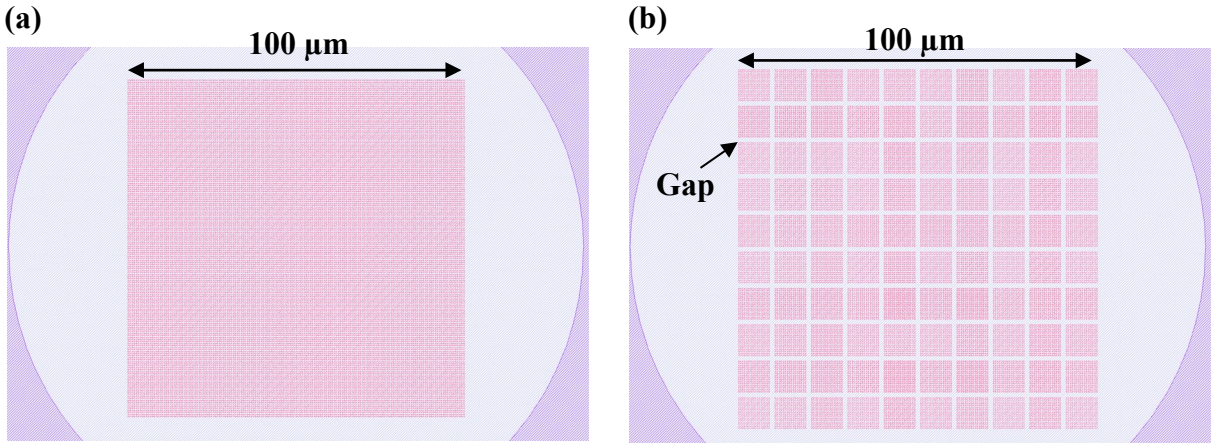

Fig. 2.5.1-15 Illustration of (a) original grating layout and (b) improved discrete blocks design.

(a) **(b)**

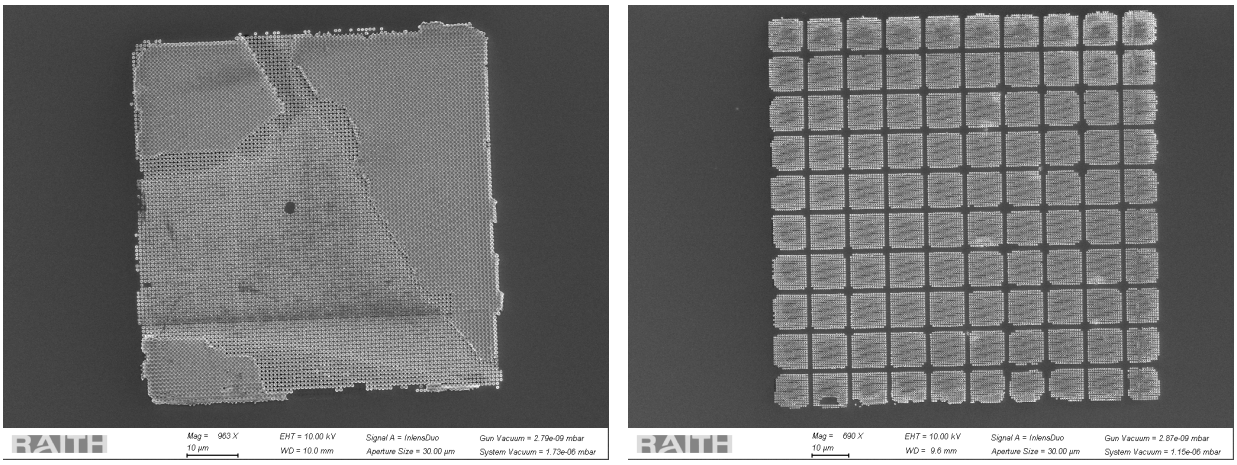

Fig. 2.5.1-16 Comparison of large area metal grating patterns (a) without gap added and (b) with gap added.

After the large area metal gratings were successfully fabricated, step (a) in the APD process flow was completed as shown in Fig. 2.5.1-13. This was followed by mesa etching and contact deposition shown as steps (b) and (c) in Fig. 2.5.1-13. The completed APD devices with metal gratings on the top are shown in Fig. 2.5.1-17. A bevel is observed on the edge of the mesa, which is likely caused by the fast lateral etch of the InAs cap layer. Nevertheless, this should not affect the quantum efficiency performance of the device.

(a) **(b)**

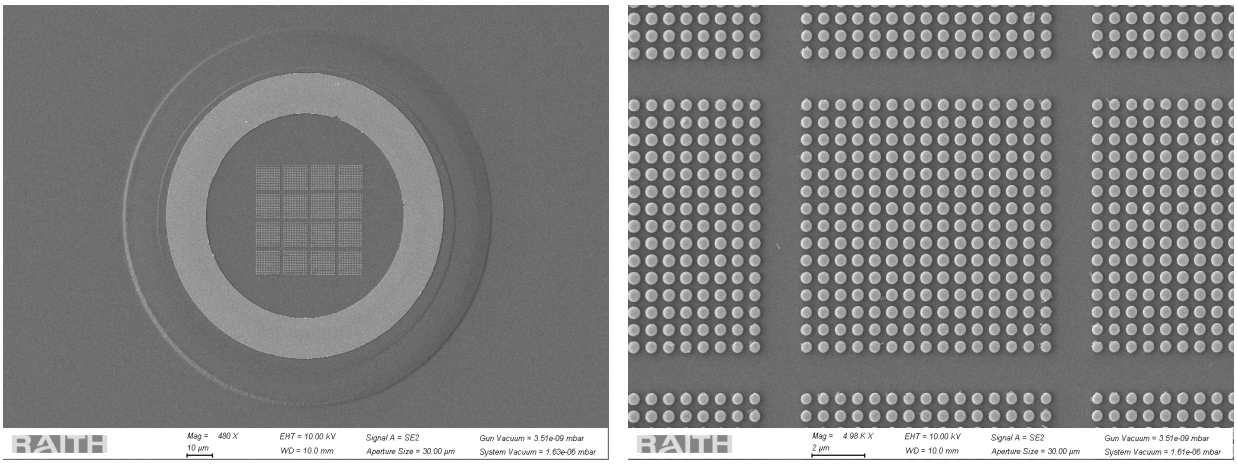

Fig. 2.5.1-17 SEM image of the fabricated thin SACM APD with sub-micron metal gratings on the top surface.

After the photon-trapping APD was fabricated, the external quantum efficiency was measured to characterize the effectiveness of the grating approach. To get a comprehensive characterization of the QE performance, the measurement was performed by two different methods. The first one was to measure the quantum efficiency using a monochromator setup, where the light is generated from a broad-band lamp source and then filtered by a monochromator. The advantage of using this setup is that it can perform a broad wavelength sweep and generate an absorption spectrum, as shown by the red curve in Fig. 2.5.1-18. It shows that the efficiency peak is at 2 μm with a grating spacing of 596 nm, which is close to the simulation prediction (~ 598 nm), but it is also worth noting that the efficiency curve has a wide line width and a much lower peak efficiency than the simulation result. This is due to the fact that the light from the monochromator setup is wide band, and therefore the measured efficiency is actually an integration over a relatively wide wavelength range. Additionally, the spot size of the monochromator setup is larger than the grating region, which may also decrease the overall efficiency. Therefore, to characterize the correct peak efficiency, the device was measured by a 2 μm semiconductor laser to reduce the spectrum linewidth and spot size. The laser response result is shown in Fig. 2.5.1-18 (a) by the purple point. As expected, the quantum efficiency measured by the laser is much higher than that by the monochromator setup, which reaches ~ 22% at 2 μm.

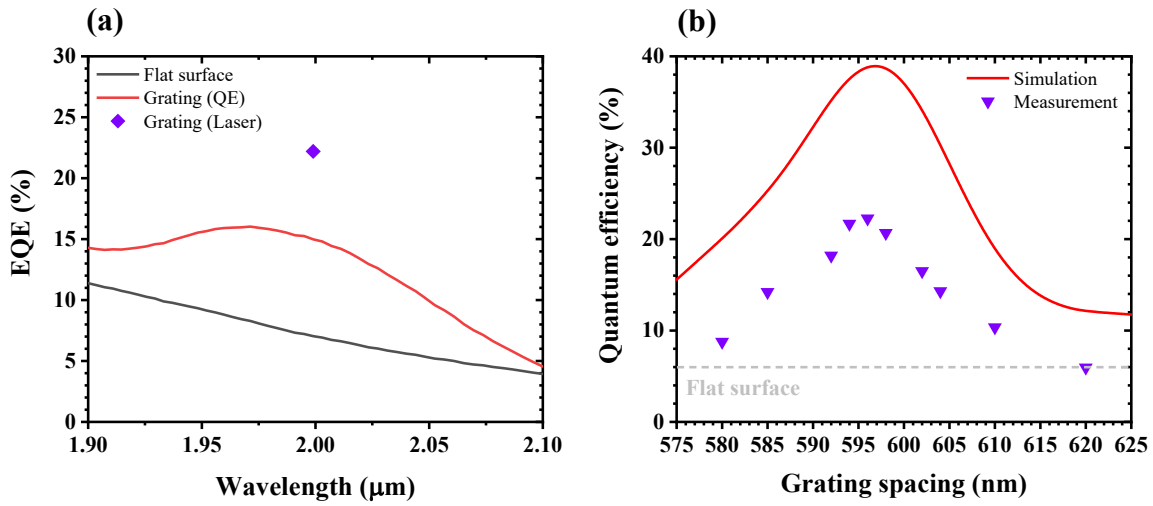

Fig. 2.5.1-18 Measured quantum efficiency of the thin SACM APD with surface metal gratings versus (a) wavelength and (b) grating spacing.

As discussed in section 2.2.2, the metal grating should work as a grating coupler to couple the normal incidence light into the absorber waveguide. Therefore, the peak wavelength and the grating spacing should follow the relationship:

$$a = \frac{\lambda_{peak}}{n_{eff}} \qquad (2.5.1-1)$$

where a is the spacing of the grating, λ_{peak} is the peak wavelength and n_{eff} is the effective index of the waveguide mode in the absorber. This is known as the Bragg condition which also indicates that the coupling efficiency will decrease when the spacing is away from the optimal value. To verify whether the grating works as a grating coupler or not, the quantum efficiency was measured with different grating spacings, and the result is shown in Fig. 2.5.1-18 (b) by the purple points. It is clear that the measured efficiency decreases when the spacing differs from 596 nm, which follows the trend predicted by the simulation. This result proved the photon-trapping mechanism of the grating as discussed in section 2.2.2.

Although the efficiency of the grating follows the correct trend predicted by the simulation, the peak value, 22%, is still lower than the simulated value of ~ 38%. The difference between the simulated and the measured efficiency is probably caused by fabrication errors. As shown by the high resolution SEM image in Fig. 2.5.1-19, the shape of the fabricated grating is not exactly the circle shape as designed on the mask. Moreover, the side wall of the grating shows a bevel angle which is probably due to the deposition angle of the e-beam evaporator. These fabrication errors may all decrease the coupling efficiency of the grating to some extent. Additionally, as shown in Fig. 2.5.1-15, the grating region on the device is designed to be discrete blocks with gaps added. This design can provide more reliable lift-off as discussed in the previous section, but the drawback is that the coupling efficiency will be lower within the gap region. Another possible reason is that a Ti layer is deposited on the surface before the Au layer to enhance the metal adhesion to the semiconductor surface. However, Ti oxidizes quickly in air. The oxidation of Ti could be critical to the quantum efficiency performance because the high coupling efficiency of the metal grating relies on the surface plasmon effect [37] which will be reduced if the metal surface become oxidized. Therefore, all these reasons including fabrication errors, mask design, and metal oxidation may contribute to the lower measured efficiency compared with the simulated value. Nevertheless, the achieved 22% external quantum efficiency is still more than 3 times higher than the bare surface and is even 2% higher than the previously reported quantum efficiency with a 1 μm thick absorber (20%) [8].

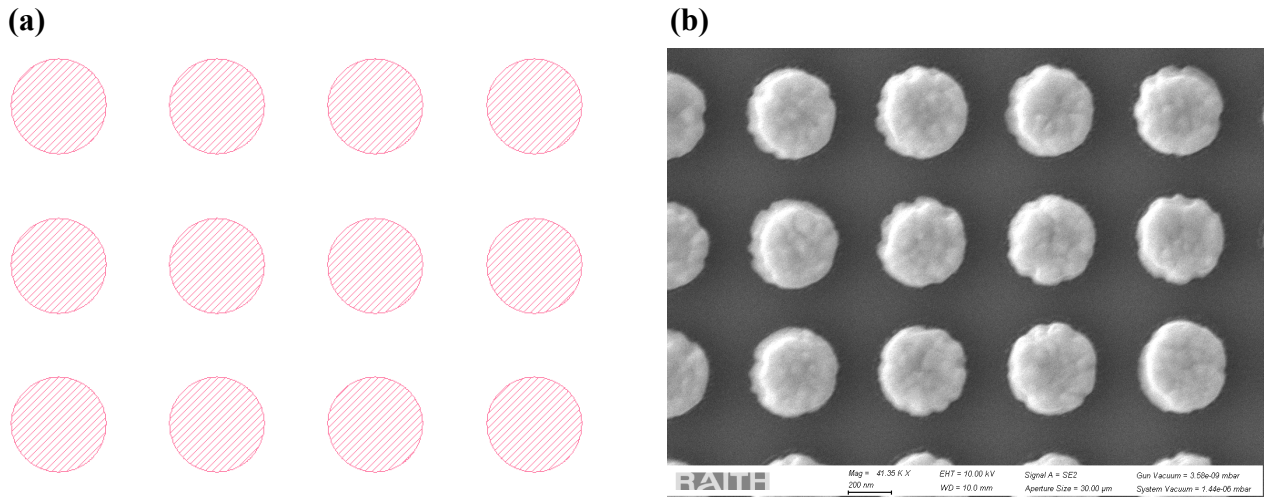

Fig. 2.5.1-19 Comparison of (a) the designed metal grating pattern and (b) fabricated metal grating pattern.

2.5.2. Edge coupling

While a surface metal grating has been demonstrated to be an effective approach to enhance the quantum efficiency, an alternative solution is to couple to the absorber waveguide through the edge of the device, as schematically illustrated in Fig. 2.5.2-1 (a). The condition for this approach is shown in Fig. 2.5.2-1 (b), i.e., a waveguide structure needs to exist in the absorber. Therefore, although the mechanisms behind this approach and the metal grating are different, the effect is similar where the light is coupled into the absorber waveguide, and the quantum efficiency is enhanced by photon trapping. This approach can be highly efficient and moreover, it may be more compatible to applications like a fiber array packaged device or waveguide-based chip.

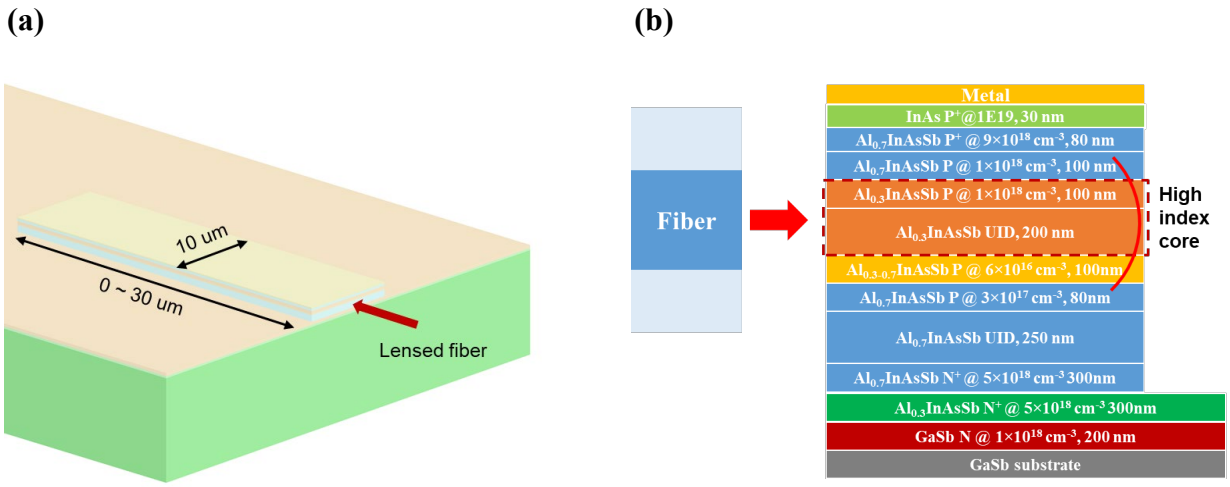

Fig. 2.5.2-1 (a) Schematic of the edge coupled waveguide APD. (b) Cross section views the thin absorber SACM APD.

Fig. 2.5.2-2 shows the simulated internal and external quantum efficiency of the edge coupled waveguide APD at 2 µm. Internal quantum efficiency (IQE) reaches ~ 70% with device length > 20 µm. However, if we assume a detector of sufficient length, the theoretical IQE should be nearly 100%. The 30% IQE loss is then found to be caused by the mode leaking into the high refractive index GaSb substrate (n ~ 4). My colleague at the University of Texas is working on the growth of AlInAsSb materials system on InP substrate, which would alleviate the mode leaking problem. As for the external quantum efficiency (EQE), a lensed fiber with spot size of 2 µm was used in the simulation and the EQE was calculated to be ~ 38% without an anti-reflection coating. The coupling loss was calculated to be ~ -3.4 dB.

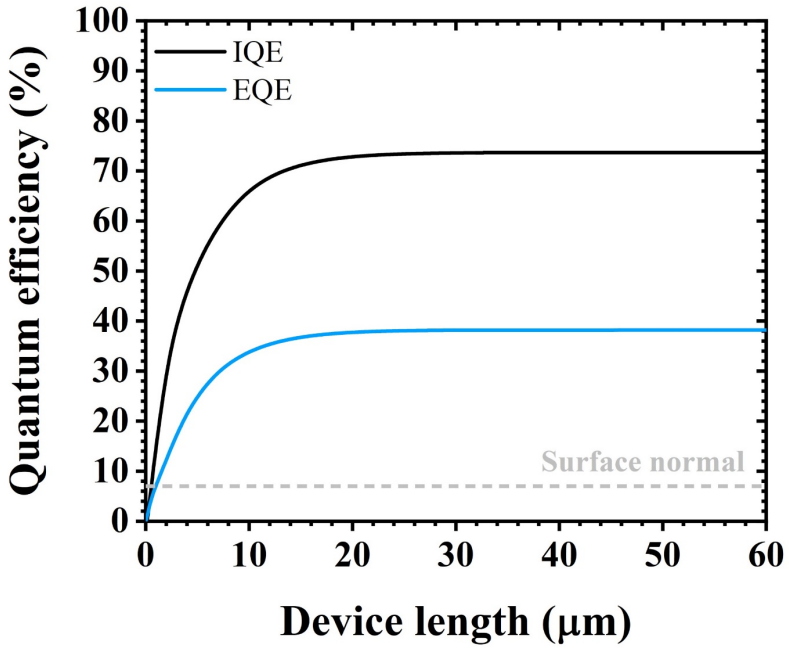

Fig. 2.5.2-2 Simulated internal and external quantum efficiency of the edge coupled waveguide SACM APD at 2 μm; the grey dashed line shows the reference efficiency measured by surface normal illumination.

Since the simulation result of the edge coupling approach was encouraging, the next step was to design the photomask for waveguide fabrication. Because the GaSb substrate has higher refractive index than $Al_{0.7}InAsSb$, no passive waveguide structure can exist in the multiplication layer. Therefore, it is not possible to couple the light from the edge of the chip and then guide it to the device by passive waveguides like in previously reported waveguide photodetectors [38-40]. An alternative way is to directly cleave the device and then couple the light from the edge, as shown in Fig. 2.5.2-3. This method is easy and straightforward, but the drawback is that that the coupling loss cannot be directly measured.

Cleaving can be performed after the fabrication of the waveguide, but the biggest challenge is to control the relatively random cleaving process, i.e., how to make sure the cleave line crosses the

small device and creates a waveguide with desired length. To address this challenge, I designed a special photomask that can create waveguide APDs with different lengths regardless of the cleaving position.

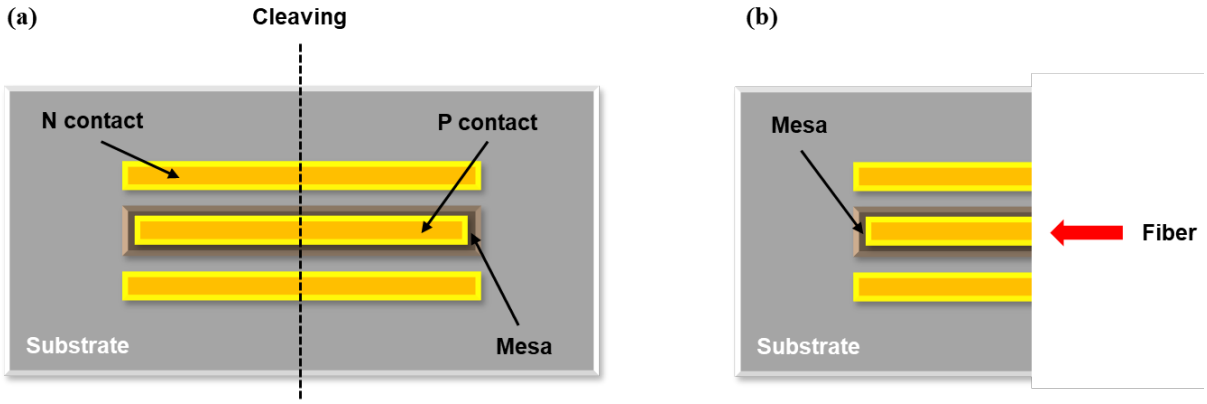

Fig. 2.5.2-3 Illustration of the device structure of waveguide APD (a) before cleaving (b) after cleaving.

First, to make sure the active waveguide can always be cleaved, the most straightforward way is to place the devices next to each other with almost no gap in the horizontal direction, as shown in Fig. 2.5.2-4 (a). Therefore, if cleaving along the vertical direction (shown by the dash line in the figure), there should be at least one device cleaved no matter where the cleave position is. However, this design assumes minimal gaps between adjacent devices, which is clearly not feasible in practice. To take the advantage of this design but still leave feasibility for fabrication, I introduced a vertically misaligned layout design as shown in Fig. 2.5.2-4 (b). With this design, the devices still have no gap along the horizontal direction to ensure the cleaving line crosses the waveguide, but physical separation is created along the vertical direction to satisfy the limited accuracy of photolithography.

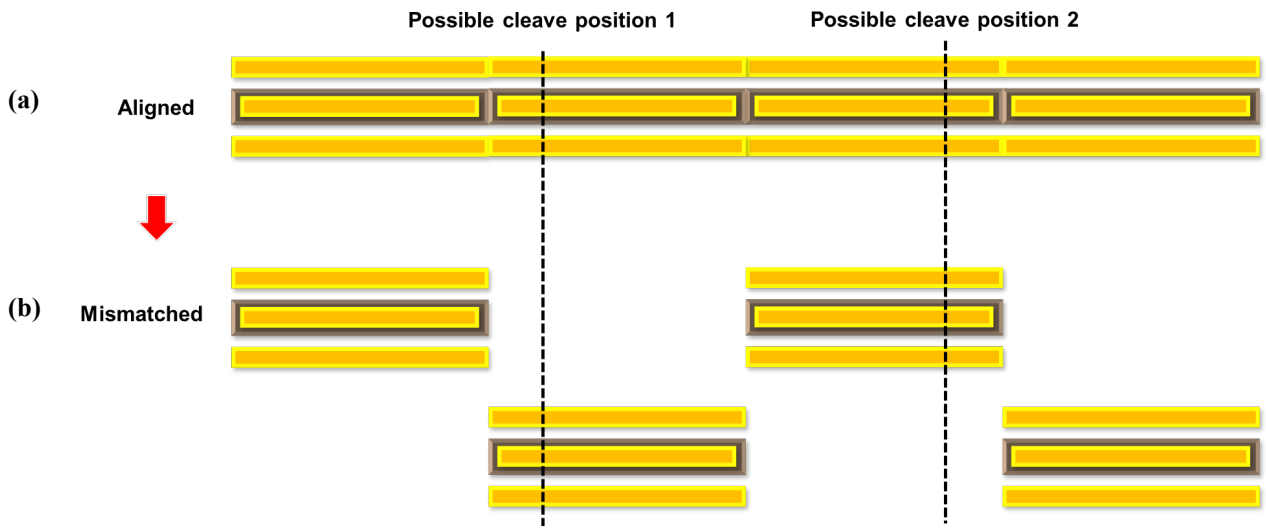

Fig. 2.5.2-4 Illustration of (a) the vertically aligned design and (b) the vertically mismatched design of waveguide APD devices .

The layout design shown in Fig. 2.5.2-4 can make sure there is at least one device cleaved regardless of position. Nevertheless, this is not enough because we also need to create waveguides with different lengths in order to verify the quantum efficiency saturation with waveguide length. Therefore, to create various waveguide lengths through one cleave process, I introduced a horizontally mismatched design as shown in Fig. 2.5.2-5. Fig. 2.5.2-5 (a) is the original layout where all the devices are perfectly aligned in the horizontal direction, and the result is that all the waveguides created by the vertical cleaving line (shown by black dash) will have the same length. In order to create different lengths on one line, I misaligned the waveguides with a certain shift distance in the horizontal direction as shown in Fig. 2.5.2-5 (b). It is evident that with this design, various lengths of waveguide can be created on one cleaving line regardless of where the cleaving position is.

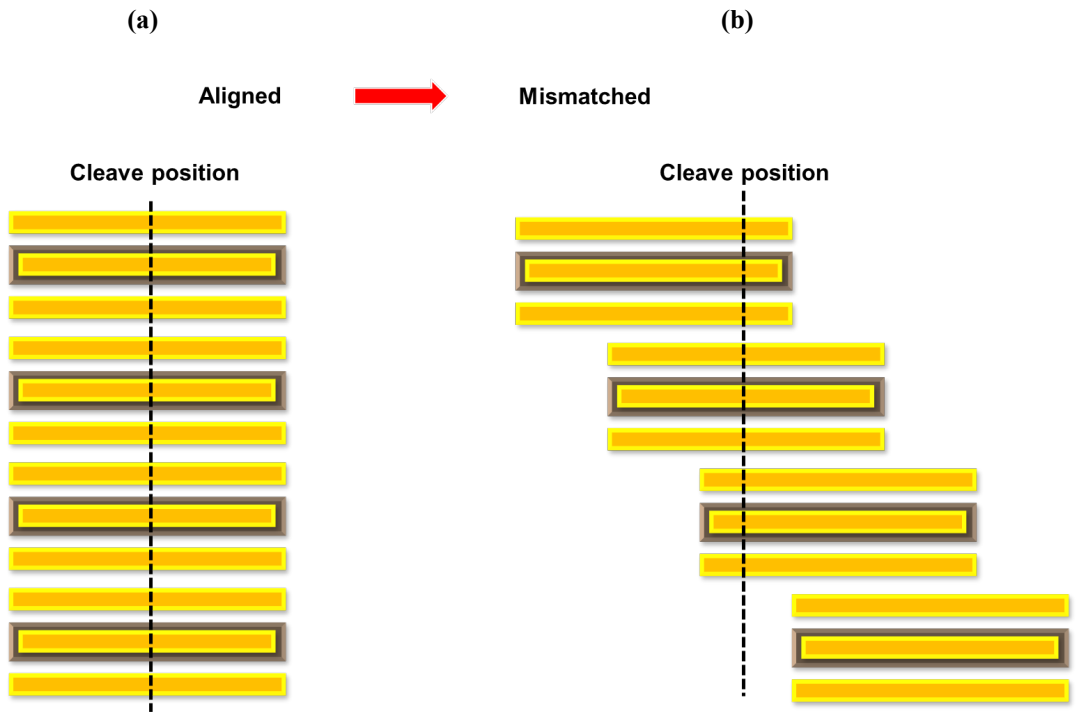

Fig. 2.5.2-5 Illustration of the horizontal mismatch layout of waveguide APD devices

By combing the vertical and the horizontal mismatched design introduced, the layout becomes the form shown in Fig. 2.5.2-6, where the black dash shows the possible cleaving positions. It is clear that no matter where the cleaving position is, waveguides with different lengths can be created. Moreover, the devices are created in four groups in the vertical direction with different widths. As shown in Fig. 2.5.2-7, not only different waveguide lengths but also different waveguide widths can be created with a single cleave. I also added alignment markers, capacitance test pads and TLM patterns to the mask as shown in Fig. 2.5.2-7. It is worth noting that no coplanar waveguide (CPW) pads were used because the GaSb substrate is highly conductive. Instead, measurements were performed by directly probing the top and bottom contacts.

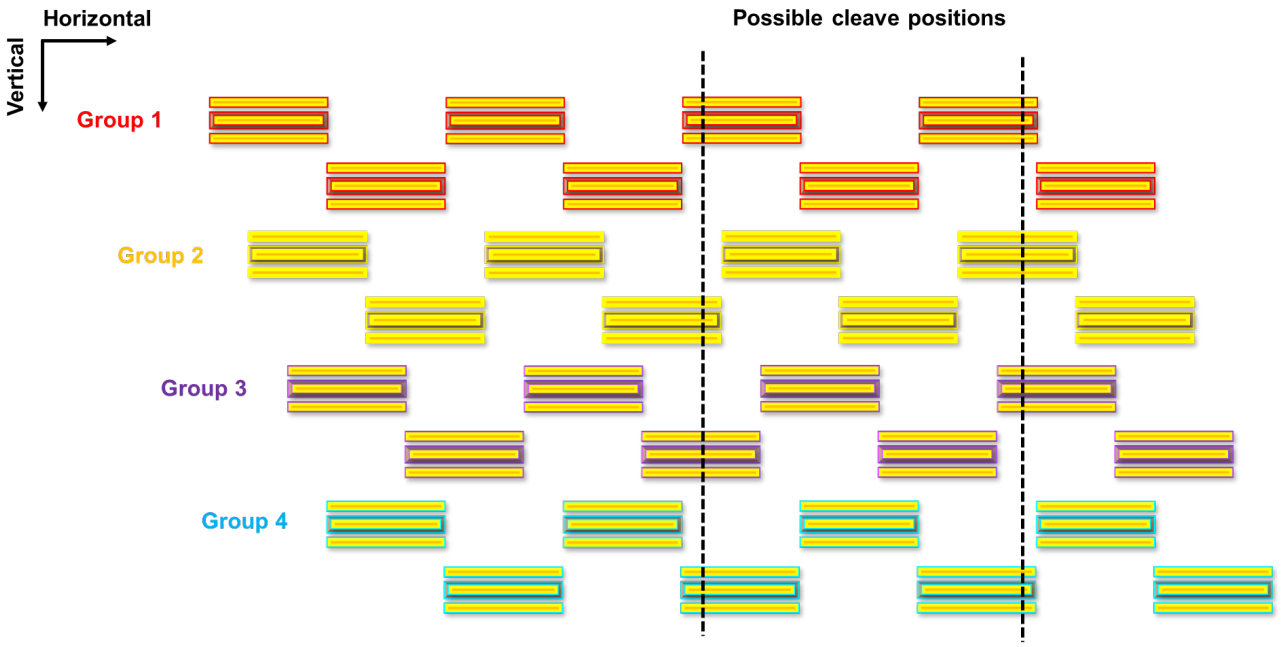

Fig. 2.5.2-6 Illustration of the mismatched design for waveguide APD devices.

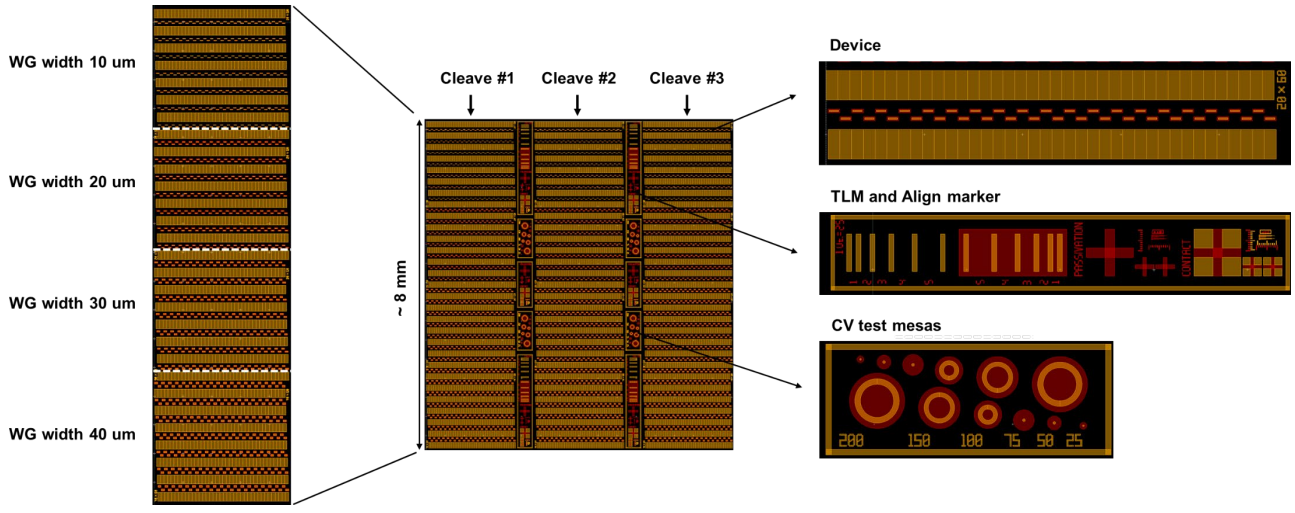

Fig. 2.5.2-7 Illustration of the final photomask layout for waveguide APDs.

Based on the designed photomask, the thin SACM APD layers were fabricated into waveguide structures by normal wet etch processing as described in Appendix A. A microscope view of the fabricated waveguide devices is shown in Fig. 2.5.2-8 (a). The devices were then cleaved along the direction vertical to the waveguide, as shown by the microscope image in Fig. 2.5.2-8 (b). A high resolution microscope image and an SEM image were taken to evaluate the quality of the cleaved surface, as shown in Fig. 2.5.2-9 (a) and (b), respectively. It is evident that a clean and smooth surface was created by cleaving.

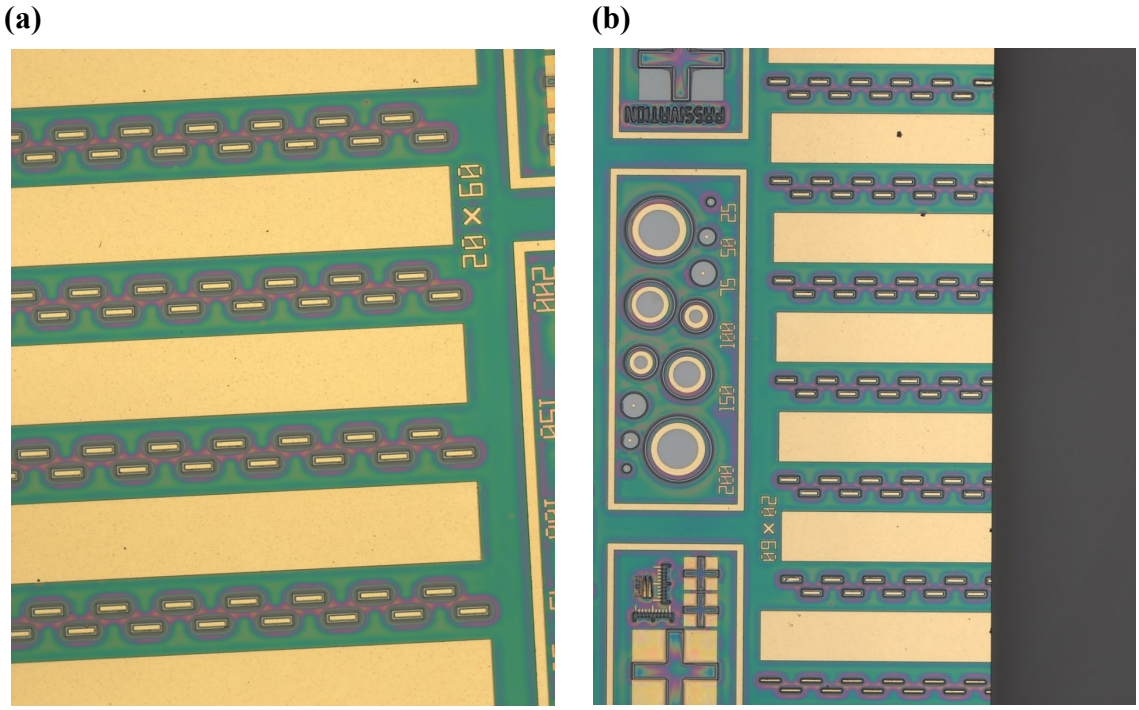

Fig. 2.5.2-8 Microscope view of the waveguide APDs (a) before cleaving and (b) after cleaving.

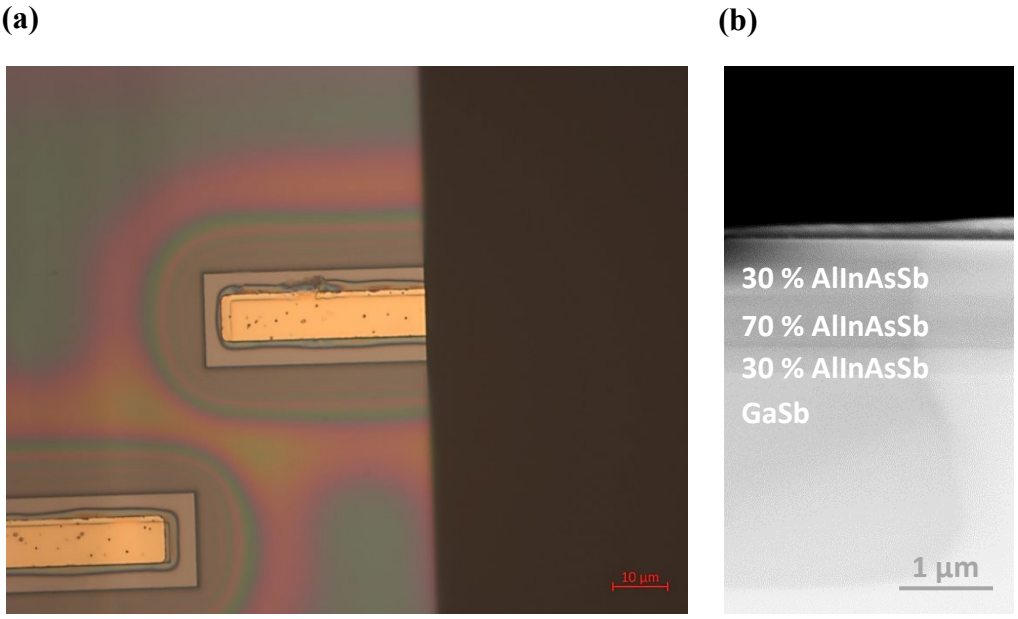

Fig. 2.5.2-9 (a) Microscope image of the cleaved waveguide APDs from the top and (b) high resolution SEM image of the cleaved edge of the waveguides.

After cleaving, the edge of the waveguide was exposed, and the device was ready for the coupling test. A schematic of the setup for measuring the quantum efficiency is shown in Fig. 2.5.2-10. A CW optical input from a temperature stabilized 2 µm semiconductor laser polarized by a polarization controller and was coupled into the device through a lensed fiber. The photoresponse was collected by directly probing the device with a ground-signal-ground (GSG) probe and the photocurrent was measured with a source meter. A picture of the photodiode with a fiber input is shown in Fig. 2.5.2-11.

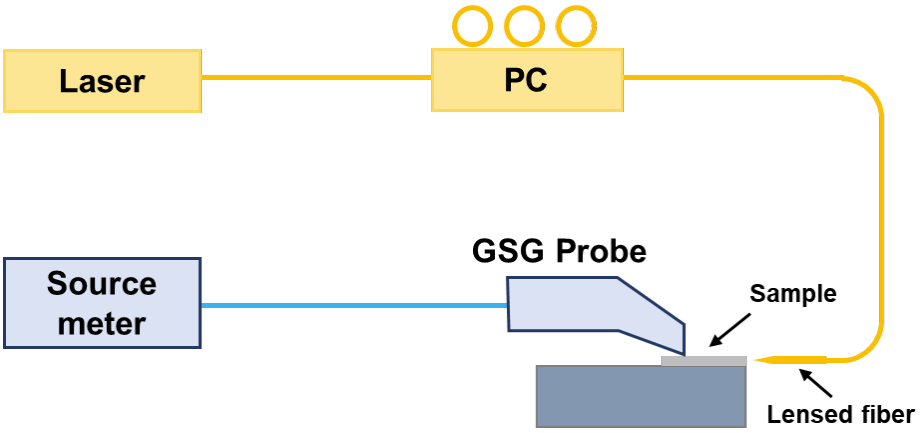

Fig. 2.5.2-10 Schematic setup for the waveguide APD measurement.

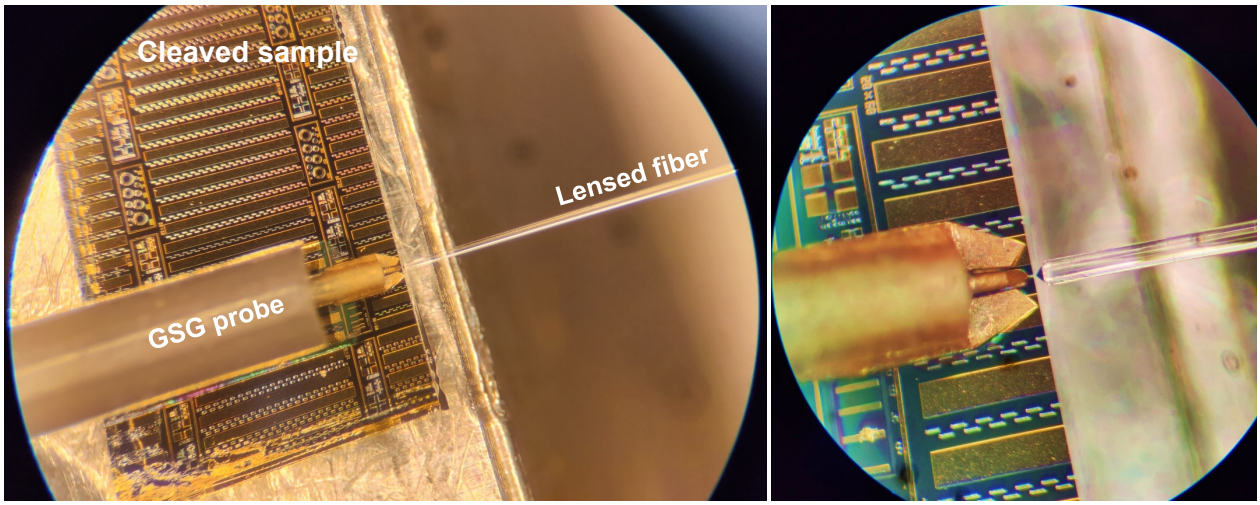

Fig. 2.5.2-11 Microscope picture of the waveguide APD measurement setup.

The steps for the quantum efficiency measurement are described as follows. First, the cleaved device was probed by a GSG probe, and the DC bias was fixed at the punch through voltage, i.e., -16V as discussed in section 2.4. Then, light was coupled from the edge of the device, while the polarization, positions and the angles of the lensed fiber were adjusted to provide the highest

photocurrent. The lensed fiber was then removed from the device under inserted to an optical power meter with an integrating sphere to measure the input optical power. The responsivity was calculated using the expression

$$R = \frac{I_{total} - I_{dark}}{P} \qquad (2.5.2-1)$$

where I_{total} and I_{dark} are the measured total current and dark current, respectively, and P is the measure optical power. It is worth noting that at -16 V, the gain of the device is not unity but is 4 as discussed in section 2.4. Therefore, the quantum efficiency can be calculated by equation

$$\eta = \frac{R \cdot 1.24}{M \cdot \lambda} \qquad (2.5.2-2)$$

where M is the multiplication gain of the device at the measured bias, λ is the wavelength (unit in μm) and R is responsivity. Fig. 2.5.2-12 shows the measured external quantum efficiency of devices with different waveguide lengths. The waveguide width is found to have no effect on EQE, which is reasonable because the minimum waveguide width (10 μm) is much larger than the spot size of the lensed fiber (~ 2 μm). Fig. 2.5.2-12 shows that the EQE quickly saturates with waveguide length after ~ 20 μm, as expected by simulation, and reaches ~ 24 %. This value is more than 3 times higher than the surface normal EQE (~ 7%) as noted in section 2.4, and is even 4 % higher than a 1 μm-thick absorber device [8]. Since there is no AR coating on the edge, the EQE could be further improved to ~ 35%.

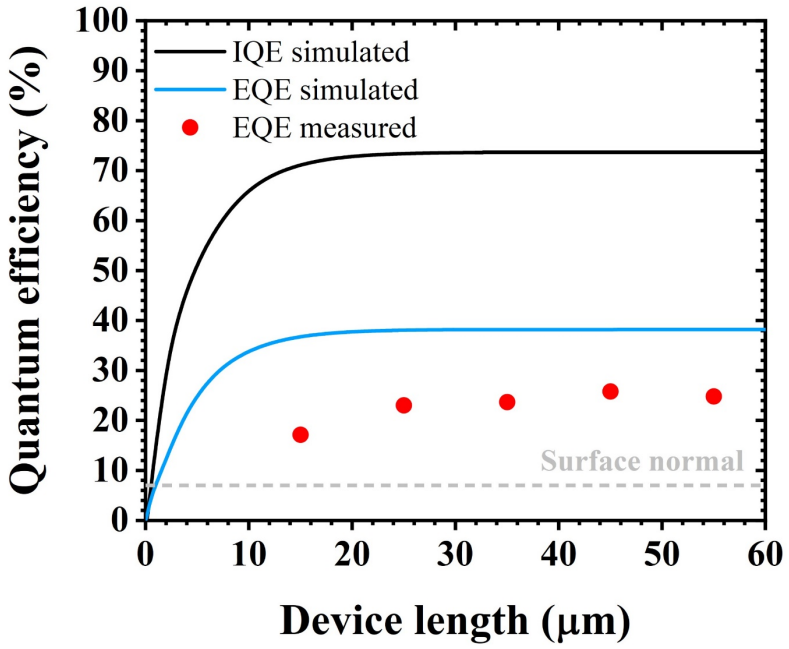

Fig. 2.5.2-12 Measured external quantum efficiency of the edge coupled waveguide SACM APD at 2 μm; simulated result is plotted for reference.

In summary, I demonstrated two effective approaches to enhance the quantum efficiency of the thin absorber SACM APD. The 2D metal grating approach achieved ~ 22% EQE through surface normal coupling, and the waveguide APD approach achieved ~ 24% EQE through edge coupling. By each approach, the EQE is more than 3 times higher than normal incidence on a bare surface and is even higher than the previous reported SACM APD (~ 20 %) with a 1 μm-thick absorber [8]. Together with the significantly suppressed dark current by the thin absorber design, at room temperature the SNR of the thin SACM device could be more than 2 orders of magnitude higher than the previously reported AlInAsSb SACM at 2 μm wavelength [8].

2.6. Bandwidth characterization and analysis

In addition to suppressing the dark current, another promising potential of the thin absorber design is to achieve high transit-time bandwidth, and therefore a high-speed device is possible utilizing a small device area to provide high RC bandwidth. The waveguide APD structure discussed in section 2.5.2, which has a minimum lateral dimension of ~ 10 μm, is promising to achieve high bandwidth. To measure the bandwidth of the waveguide APD, the frequency response measurement setup shown in Fig. 2.6-1 was assembled with edge coupling capability. The CW optical signal from a temperature-stabilized 2-μm semiconductor laser was directed through a polarization controller and then modulated by a $LiNbO_3$ Mach-Zehnder modulator (MZM). The modulator was biased at the quadrature point and driven by a vector network analyzer (VNA). The modulated optical signal was modulated by another MZM and then coupled into the waveguide APD device with a lensed fiber, and the photoresponse was collected through a GSG probe. The RF photoresponse was measured by the VNA using a bias-tee. Circuit and probe loss have been calibrated for the measurement.

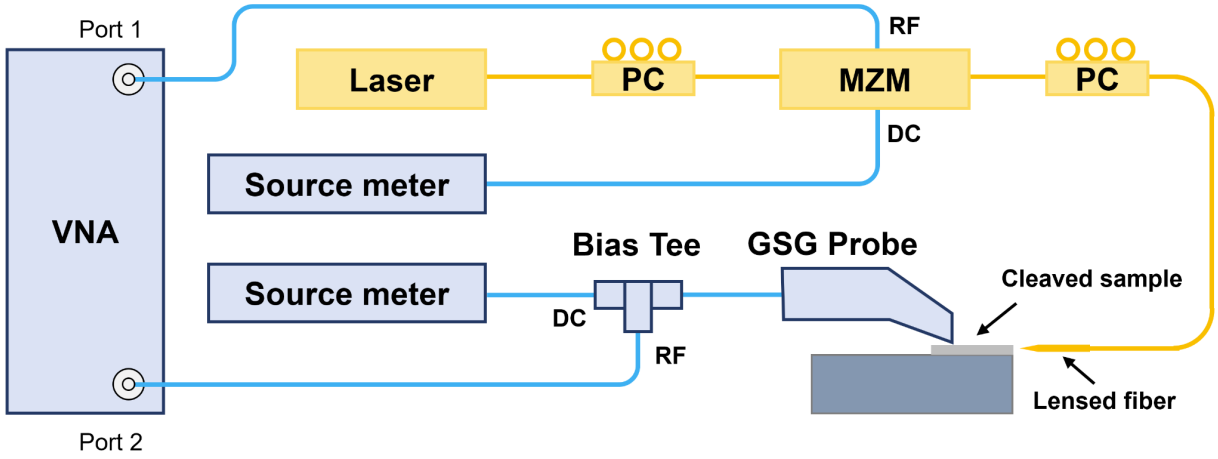

Fig. 2.6-1 Experimental setup for waveguide APD bandwidth measurement.

Fig. 2.6-2 shows the normalized frequency response ((a-1) to (e-1)) and the extracted 3-dB bandwidth and gain-bandwidth product ((a-2) to (e-2)) of the waveguide APDs with dimensions of 40 × 45 μm, 40 × 25 μm, 20 × 40 μm, 10 × 55 μm and 10 × 35 μm, respectively. For each device, the bandwidth first increases with gain, peaks at ~ 10 and then starts to decrease. The increase in the bandwidth prior to gain of 10 is due to the insufficient voltage to fully deplete the absorber at punch through. As indicated by the C-V curve shown in Fig. 2.4-2, the absorber is not fully depleted at -16 V. Therefore, photogenerated carriers have to diffuse out of the absorber, resulting in a low transit-time bandwidth until the absorber is fully depleted at ~ -17 V, where the gain is ~ 10. The decrease in the bandwidth at higher gain is caused by the avalanche build-up time. The gain-bandwidth product (GBP), defined as bandwidth multiplied by the gain, increases and then saturates. Comparing waveguide devices with different dimensions, as plotted in Fig. 2.6-3, smaller devices tend to have higher maximum bandwidth and gain-bandwidth product, which probably indicates an RC time bandwidth limit as opposed to a constant gain-bandwidth limit originating with the avalanche buildup time. As shown by the purple curve in Fig. 2.6-3, the smallest waveguide device with dimension of 10 × 35 μm reaches a maximum 3-dB bandwidth of ~ 7 GHz and a gain bandwidth product over 200 GHz. Both of these values are more than 4 times higher than the previously record bandwidth for 2 μm APD [20].

A trend that is worth noting in Fig. 2.6-3 is that the bandwidth of the waveguide APDs shows a clear area dependence. Generally, this may indicate a RC time bandwidth limit because the junction capacitance is proportional to the device area. To further understand the bandwidth limit, microwave scattering parameters (S_{11}) were measured using the same setup shown in Fig. 2.6-1 but with only port 1 active. Fig. 2.6-4 shows the measured S_{11} curves of the waveguide APDs with different dimensions and at various bias voltages. For all device dimensions, the S_{11} curves do not converged

directly after the punch through voltage (-16V) but gradually become less capacitive and then converge at ~ - 17 V. The reason is consistent with the increase in bandwidth prior to -17 V, because the absorber is not fully depleted at – 16 V, and therefore higher voltage is needed to converge the capacitance.

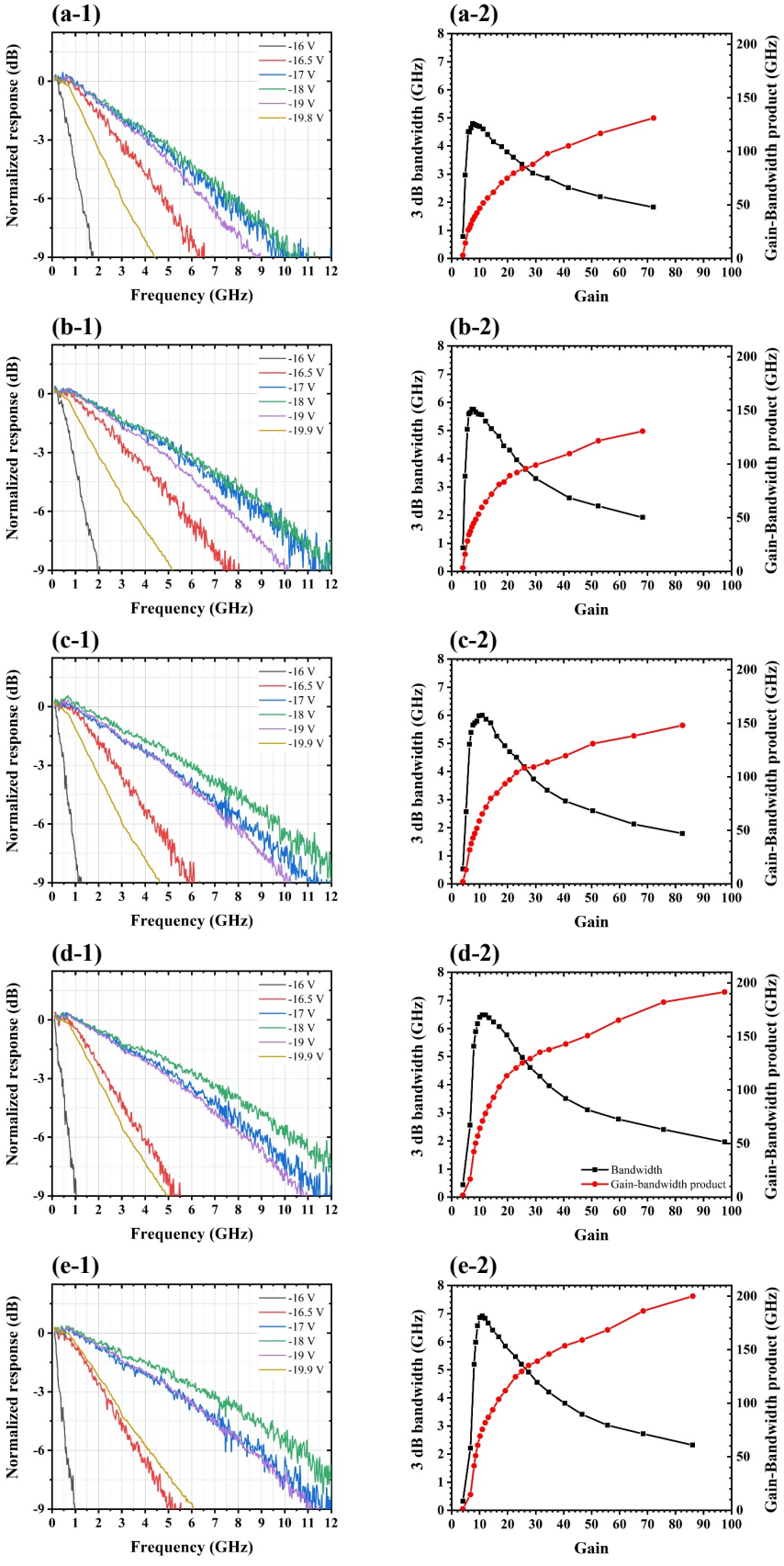
(a-1)
(a-2)
(b-1)
(b-2)
(c-1)
(c-2)
(d-1)
(d-2)
(e-1)
(e-2)
Normalized response (dB)
Frequency (GHz)
-16 V
-16.5 V
-17 V
-18 V
-19 V
-19.8 V
-19.9 V
3 dB bandwidth (GHz)
Gain-Bandwidth product (GHz)
Gain
Bandwidth
Gain-bandwidth product

Fig. 2.6-2 (a-1) ~ (e-1) Measured frequency response and (a-2) ~ (e-2) extracted 3-dB bandwidth and gain bandwidth product of waveguide APDs with dimensions of (a-#) 40 × 45 μm (b-#) 40 × 25 μm (c-#) 20 × 40 μm (d-#) 10 × 55 μm and (e-#) 10 × 35 μm, respectively.

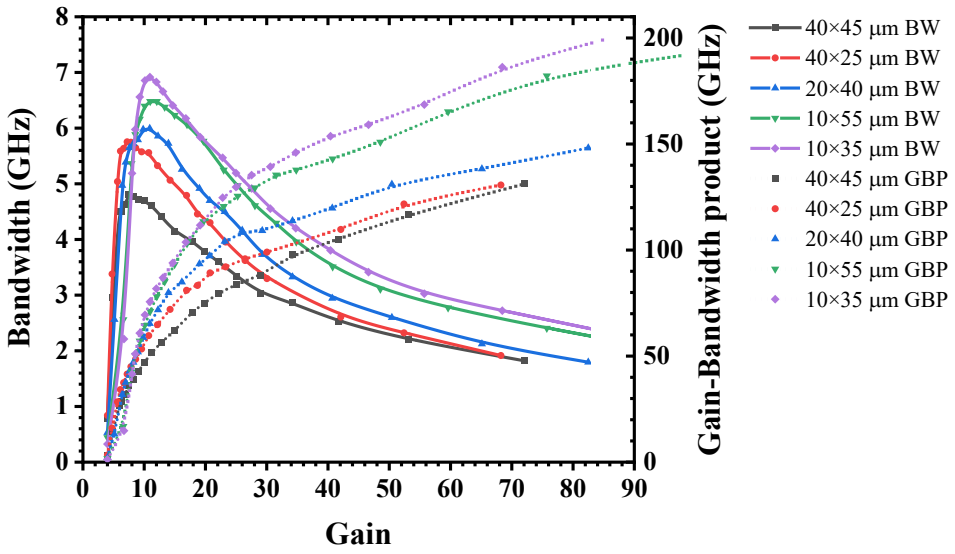

Fig. 2.6-3 Summary of the measured bandwidth (BW) and gain-bandwidth product (GBP) of waveguide APDs with different dimensions.

The equivalent circuit of a typical P-I-N photodiode is shown in Fig. 2.6-5, with the RC bandwidth expressed as:

$$f_{RC} = \frac{1}{2\pi C_j (R_s + R_L)} \qquad (2.6-1)$$

where C_j is the junction capacitance, R_s is the series resistance and R_L is the load resistance. To fit each lumped element in the equivalent circuit model and calculate the theoretical bandwidth of the device, S_{11} simulation was performed by Keysight Advanced Design System (ADS) and then fitted to the measured S_{11} curves.

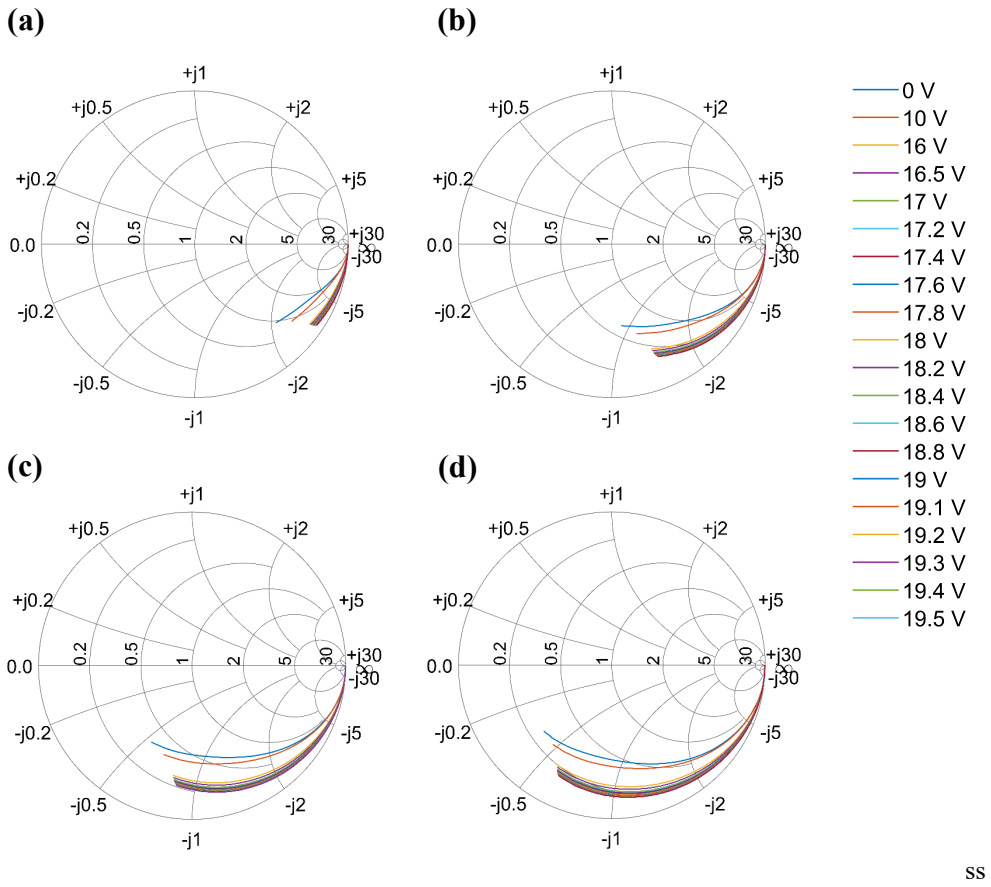

Fig. 2.6-4 Measured S_{11} curves of waveguide APDs with dimensions of (a) 10 × 60 μm (b) 20 × 60 μm (c) 30 × 60 μm and (d) 40 × 60 μm and at various bias voltages.

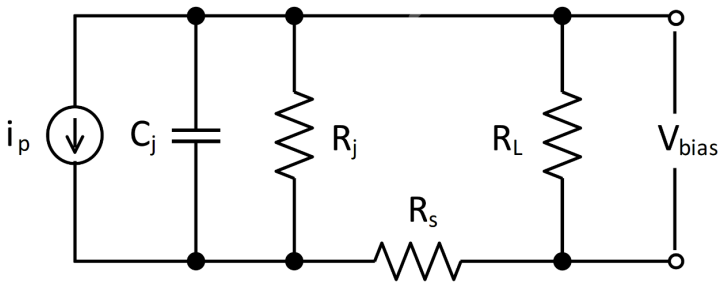

Fig. 2.6-5 Equivalent circuit model of P-I-N photodiode.

As shown in Fig. 2.6-6, the simulated S_{11} curves fit well with the measured results, and the fitted value of the lumped elements in the circuit model are listed in Table 2.6-1. Based on equation (2.6-

1), the theoretical RC bandwidth was calculated and listed in Table 2.6-2. The S_{11} values were measured on uncleaved devices, and therefore the fitted capacitance has been scaled slightly by device area to fit the cleaved waveguides used in bandwidth measurement. As shown in Table 2.6-2, the fitted RC time bandwidth is significantly higher than the measured 3-dB bandwidth, which indicates that the bandwidth is not limited by the RC time constant. Generally, the total 3-dB bandwidth of a PIN photodiode is determined by the RC bandwidth and transit-time bandwidth, as expressed by equation:

$$f_{3dB} = \sqrt{\frac{1}{\frac{1}{{f_{RC}}^2} + \frac{1}{{f_{TR}}^2}}} \qquad (2.6-2)$$

where f_{3dB} is the total 3-dB bandwidth, f_{RC} is the RC time limit bandwidth and f_{TR} is the transit-time bandwidth. If no third contributor to the total bandwidth exists, the transit-time bandwidth can be determined from this equation, the measured 3-dB bandwidth, and the fitted RC time bandwidth listed in Table 2.6-1. As shown in Table 2.6-2, the calculated transit-time bandwidth that fits the measurement is lower than 10 GHz, which is apparently in conflict with the simulated result discussed in section 2.3 (~ 31.6 GHz at unit gain). Consequently, it is very likely that a third contributor other than f_{RC} and f_{TR} dominate the bandwidth of the waveguide APDs.

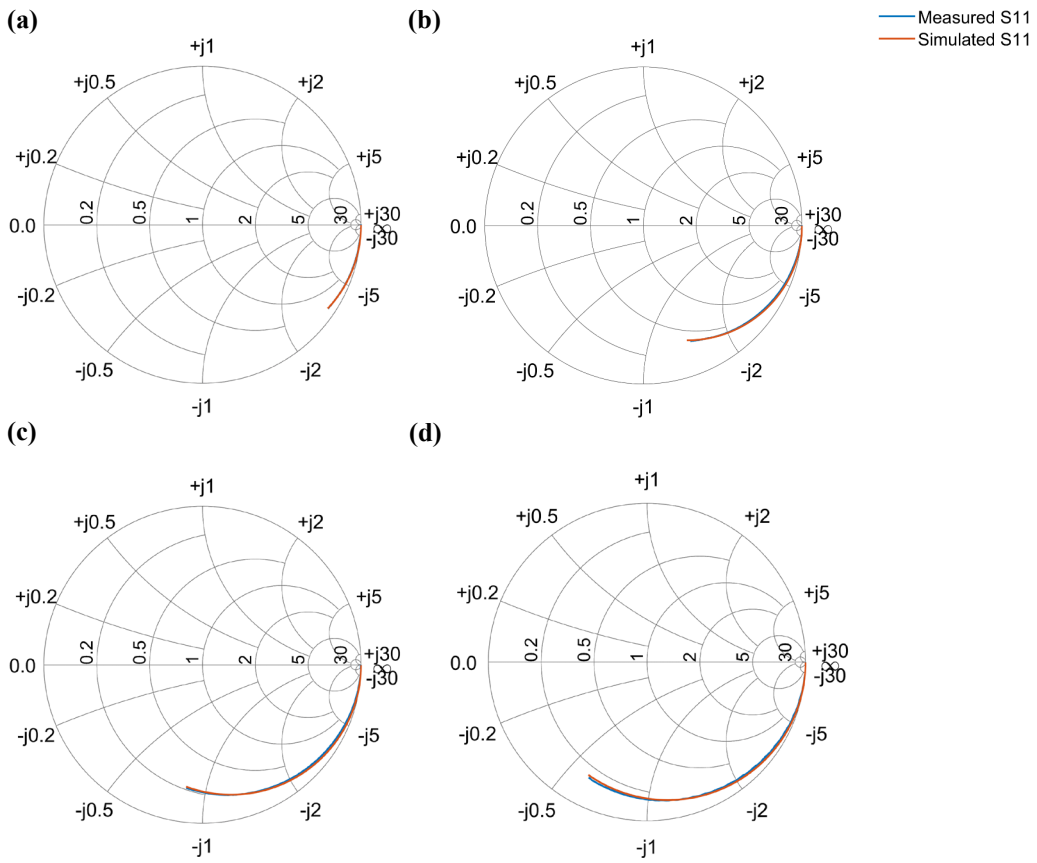

Fig. 2.6-6 Simulated S_{11} curves of waveguide APDs with dimensions of (a) 10 × 60 μm (b) 20 × 60 μm (c) 30 × 60 μm and (d) 40 × 60 μm and at bias voltages of -19V.

Table 2.6-1 Fitted parameters in the equivalent circuit model of P-I-N photodiode

Device dimensions	C_j	R_s	R_L
10 × 60 μm	0.075 pF	15 Ω	50 Ω
20 × 60 μm	0.178 pF	13 Ω	50 Ω
30 × 60 μm	0.288 pF	11 Ω	50 Ω
40 × 60 μm	0.410 pF	7.5 Ω	50 Ω

Table 2.6-2 Measured 3-dB bandwidth and the theoretical RC bandwidth calculated by the fitted resistances and capacitances.

Device dimensions	f_{3dB}	f_{RC}
10 × 35 μm	6.9 GHz	55.9 GHz
10 × 50 μm	6.4 GHz	35.6 GHz
20 × 40 μm	5.9 GHz	19.4 GHz
40 × 25 μm	5.7 GHz	16.2 GHz
40 × 45 μm	4.8 GHz	9.0 GHz

To investigate the third bandwidth contributor, the first thing that is worth noting is that the thin absorber SACM APD structure is grown on a GaSb substrate which is a well-known conductive substrate with a doping level of 1×10^{17} to 9×10^{17} cm^{-3}. This high doping level in the substrate may cause very complex RF effects. In fact, a strong bandwidth limit has been observed in many other photodetectors grown on GaSb substrate, such as GaInAsSb [41] and InAs/GaSb T2SL [42, 43] MWIR photodetectors. What these devices have in common is that the measured 3-dB bandwidth never exceeds 10 GHz regardless of the device diameter and the depletion layer thickness. It is suspected from these references that the bandwidth is likely limited by the RF loss from the conductive GaSb substrate. Recently, a group at Northwestern University did a study on the influence of the GaSb substrate on the bandwidth of a photodetector. As described in ref. [44], a transfer printing technique was used to peel off the photodetector grown on GaSb substrate, and then the device was bonded onto an insulating sapphire substrate. With exactly the same device structure, the 3-dB bandwidth improved from ~ 6 GHz to ~ 18 GHz by replacing the substrate. This research confirms that the GaSb substrate may limit the bandwidth of photodetectors. Moreover, by comparing the bandwidth with and without the GaSb substrate, the substrate limited bandwidth factor f_{sub} is estimated to be ~ 8 GHz [44]. Therefore, by assuming the substrate limiting factor also

exists for my thin absorber SACM APD, f_{sub} can be extracted by adding the substrate factor to equation (2.6-2), and the bandwidth equation becomes:

$$f_{3dB} = \sqrt{\frac{1}{\frac{1}{{f_{RC}}^2} + \frac{1}{{f_{TR}}^2} + \frac{1}{{f_{sub}}^2}}} \qquad (2.6-3)$$

where f_{sub} is the bandwidth factor caused by the conductive GaSb substrate. By substituting the fitted RC bandwidth f_{RC} in Table 2.6-2 and the simulated transit-time bandwidth f_{TR}, f_{sub} can be calculated using equation (2.6-3) and the result is shown in Table 2.6-3. The substrate limited bandwidth is ~ 7 GHz, which is comparable to the value observed in ref. [44]. Therefore, the bandwidth of the thin SACM APD is strongly limited by the conductive GaSb substrate.

Table 2.6-3 Measured 3-dB bandwidth, theoretical RC bandwidth, simulated transit-time bandwidth and the calculated substrate limiting bandwidth.

Device dimensions	f_{3dB}	f_{RC}	f_{TR}	f_{sub}
10 × 35 μm	6.9 GHz	55.9 GHz	31.6 GHz	7.0 GHz
10 × 50 μm	6.4 GHz	35.6 GHz	31.6 GHz	6.6 GHz
20 × 40 μm	5.9 GHz	19.4 GHz	31.6 GHz	6.3 GHz
40 × 25 μm	5.7 GHz	16.2 GHz	31.6 GHz	6.1 GHz
40 × 45 μm	4.8 GHz	9.0 GHz	31.6 GHz	5.7 GHz

In summary, this section described the characterization of the bandwidth performance of the thin absorber SACM APD. The frequency response measurement shows that the maximum 3-dB bandwidth of the device reaches ~ 7 GHz, and the gain-bandwidth product is over 200 GHz, both of which are more than 4 times higher than previously reported 2 μm APDs. The improved speed performance of this device can enable high speed applications of APDs at 2 μm, such as MWIR

communication as described in the introduction section. Additionally, it is also revealed that the bandwidth of the device is strongly limited by the conductive GaSb substrate. Therefore, by growing the device on a semi-insulating InP substrate in the future, the bandwidth of the device can be substantially improved, offering the potential to reach over 30 GHz.

2.7. Future work

In this chapter, the idea of using the combination of an ultra-thin absorber and photon trapping structures has been demonstrated, which improved both the SNR and the bandwidth performance of 2 μm APDs significantly. Therefore, it is very promising that we can further apply this approach to longer cut-off wavelength APDs in the MWIR range. However, difficulties of using the photo-trapping approach will also rise when moving to the longer wavelengths. For example, Fig. 2.7-1 shows a possible structure for a long-wavelength cut-off SACM APD based on AlInAsSb materials system, where a narrow bandgap InAsSb is used as the absorber material to reach cut-off wavelength beyond 4 μm. However, in order for the photon-trapping structure to work, a waveguide structure needs to be supported. As described by equation (2.3-6), the minimum absorber thickness that can support a waveguide mode is around half wavelength, i.e., ~ 300 nm for 2 μm and ~ 600 nm for 4 μm. It is clear that for longer wavelength, a thicker absorber is needed to support a waveguide mode. This is evidently conflict with the benefit of using photon-trapping structure which is designed to achieve high QE with an ultra-thin absorber so that the dark current can be suppressed. Thus, how to solve the thickness limit will be the critical problem for extending the photon-trapping approaches to longer wavelengths.

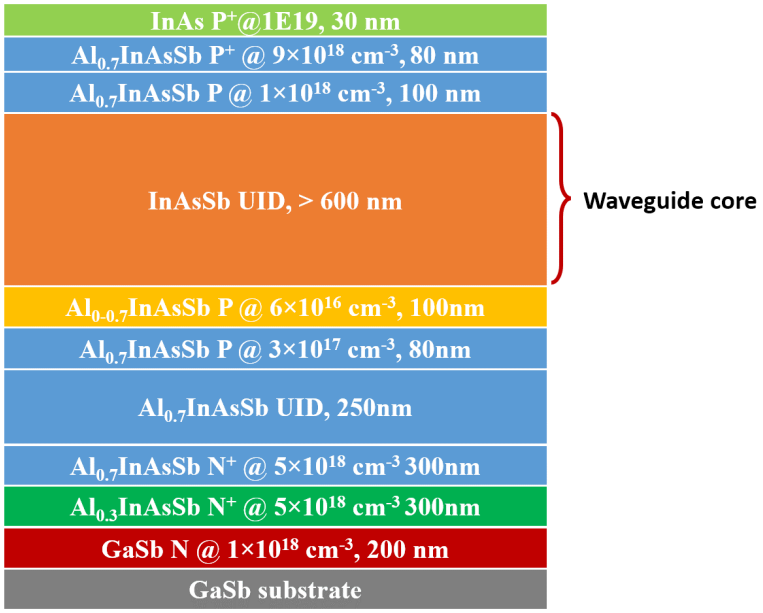

Fig. 2.7-1 Possible layer structure of a ~ 4 μm cut-off SACM APD using an InAsSb absorber.

To better understand how to solve this challenge, it needs to be clarified first that the condition for a waveguide mode to exist is that the core refractive index is higher than that of the cladding, and at the same time the core is at least half wavelength thick. The core does not necessarily need to be the narrow bandgap material but only needs to have higher refractive index than the cladding layer. Therefore, we can use a wider bandgap material to support a waveguide mode instead of increasing the InAsSb layer thickness. For example, Fig. 2.7-2 shows a "sandwich" absorber design to solve the thickness limit, where the narrow-bandgap InAsSb is placed between two mid-bandgap $Al_{0.5}InAsSb$ layers with wide-bandgap $Al_{0.7}InAsSb$ layers as the cladding layers. The combined region of the InAsSb and the $Al_{0.5}InAsSb$ layers have higher effective refractive index than the cladding $Al_{0.7}InAsSb$ layers, and therefore they serve as the core of the waveguide. As a result, the minimum core thickness here, which needs to be ~ 600 nm at 4 μm, will be the total thickness of the InAsSb layer plus the $Al_{0.5}InAsSb$ layers, so that the narrow bandgap InAsSb could be, in theory, very thin while still supporting a waveguide mode. Since $Al_{0.5}InAsSb$ has a much wider bandgap

than that of InAsSb, increasing its thickness will give rise to less dark current compared with using InAsSb. Consequently, the thickness limit associated with photon-trapping approaches can be relaxed by the "sandwich" absorber design.

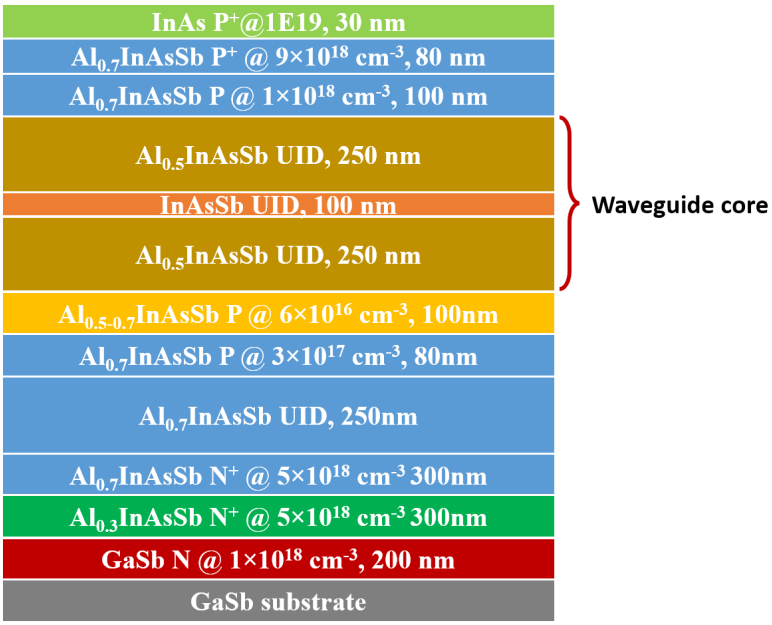

Fig. 2.7-2 "Sandwich" absorber design for releasing the absorber thickness limit for photon-trapping SACM APDs.

Nevertheless, Fig. 2.7-2 merely shows a basic idea of designing layers for a long-wavelength photon-trapping APDs. Other designs, such as optimizing bandgap variation and doping to minimize the barrier to carrier transport, optimizing the InAsSb/$Al_{0.5}$InAsSb layer thickness fraction for trade-off between the dark current and the device length, optimizing InAsSb layer position (it does not have to be in the center) and optimizing photon-trapping structure dimensions, still need to be considered in the future after the target wavelength is determined. I am confident that this solution is feasible and believe it could achieve significantly high SNR and high-speed long-wavelength APDs in the future.

3. Infrared nBn photodetectors

3.1. Motivation

Instead of boosting the signal level by using an APD, another direction for improving SNR performance is to reduce the dark current and thus to decrease the noise power level of MWIR detectors. Since the bandgap of the MWIR absorbing material is small, avoiding a high electric field is critical. Therefore, the n-barrier-n (nBn) photodetector design has been developed to significantly reduce the dark current by suppressing the Shockley-Read-Hall (SRH) generation currents. An nBn photodetector usually consists of a narrow bandgap undepleted, n-type absorber followed by a wide bandgap barrier layer. The large conduction band offset at the barrier layer effectively blocks the diffusion of majority carriers (electrons) but allows minority carriers (holes) to pass through. Since the nBn photodetector operates with low voltage across the narrow bandgap absorber the SRH generation and tunneling are moderated to a great extent.

To date, substantial progress has been made with nBn photodetectors fabricated from a wide range of materials, including type-II superlattice (T2SL) [45, 46] and type-II strained-layer superlattice (T2SLS) [47-50]. Compared to the T2SL, the T2SLS is easier to grow [51] and has longer minority carrier lifetimes [52]. However, the quantum efficiency of T2SLS nBn photodetectors in the long-wave infrared (LWIR) range is limited by the low absorption coefficients [53, 54], especially in n-type absorbers, due to the longer superlattice period of the T2SLS [53]. While efforts toward enhancing T2SLS quantum efficiency and reducing dark current are ongoing [47, 53], another promising approach lies in new materials systems that have the potential to overcome the intrinsic limitations of conventional superlattices. Recently, high-performance avalanche photodiodes (APDs) have been demonstrated in the $Al_xIn_{1-x}As_ySb_{1-y}$ (referred to as Al_xInAsSb below) digital alloy material system [8, 55-57]. These devices show high gain, low dark current, extremely low

excess noise and high temperature stability compared to conventional III-V materials. AlInAsSb is also a promising candidate for MWIR nBn photodetectors with the unique characteristic of a minimal valence band discontinuity within a wide range of bandgap energies (from 0.247 eV to 1.3 eV) [58]. This eliminates hole trapping at the absorber/barrier valance band discontinuity giving rise to longer hole diffusion length, higher quantum efficiency, lower turn-on voltage, and higher detectivity.

3.2. Device simulation and design

The target wavelength for the nBn photodetector reported in this chapter was chosen to be 2 μm where high performance AlInAsSb APDs have been previously demonstrated. Fig. 3.2-1 shows a schematic cross section of the AlInAsSb structure. The absorber is $Al_{0.3}InAsSb$ (E_g = 0.58 eV) and the barrier is $Al_{0.7}InAsSb$ (E_g = 1.16 eV). XPS characterization indicates that the AlInAsSb materials system has near-zero valence band discontinuity. Therefore, the conduction band offset should be approximately the bandgap difference between $Al_{0.3}InAsSb$ and $Al_{0.7}InAsSb$, i.e., 0.58 eV, which is sufficient to suppress the thermionic emission of majority carriers over the barrier. The active layers (absorber, barrier, and buffer layer) were sandwiched by two highly-doped N $Al_{0.3}InAsSb$ contact layers. A buffer layer was inserted beneath the barrier layer to avoid possible dopant diffusion from the N contact layer. The band diagram has been modeled using Lumerical CHARGE solver and is plotted in Fig. 3.2-2 at equilibrium (a), under reverse bias (b), and under forward bias (c).

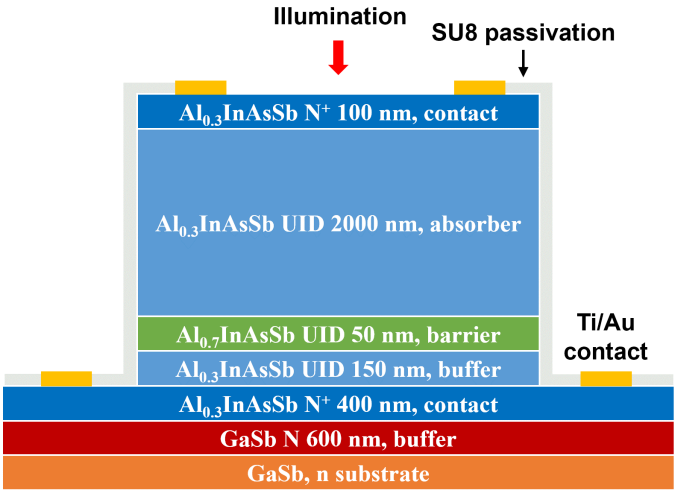

Fig. 3.2-1 Schematic cross-section of the AlInAsSb nBn photodetector.

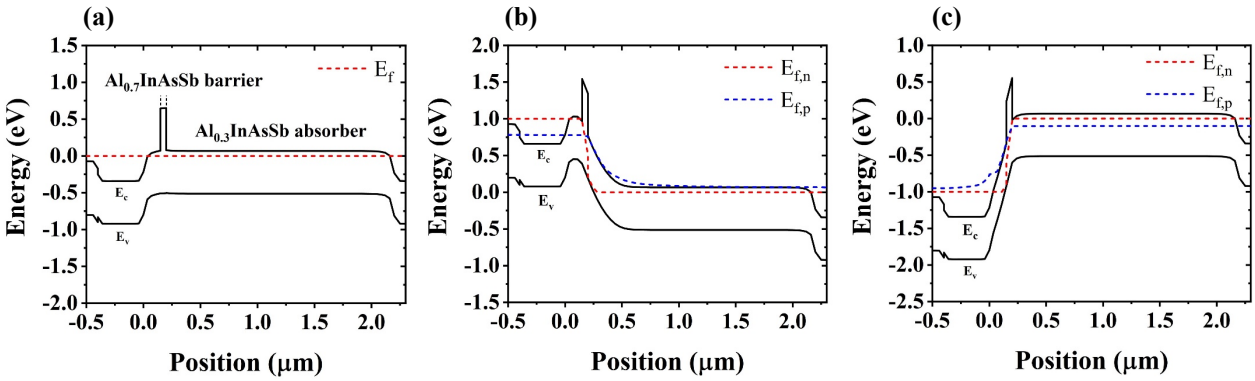

Fig. 3.2-2 Simulated energy band diagram of the AlInAsSb nBn photodetector (a) at equilibrium, (b) under a reverse bias of -1V, and (c) under a forward bias of 1V.

Two of the primary design parameters are the thickness and the doping concentration of the absorber. Since the nBn photodetector has very low electric field applied across the absorber, the photocurrent is primarily a diffusion current. A thicker absorber will achieve higher absorption, however, collection of the photogenerated carriers may be limited by the diffusion length. Fig. 3.2-3 (a) shows the simulated absorption and responsivity versus the absorber thickness. While the absorption increases with thickness, the responsivity peaks and then decreases for thickness greater

than ~3 μm. The reason for this behavior is revealed by the simulated carrier collection efficiency shown in Fig. 3.2-3 (b). Below an absorber thickness of 2 μm, the increase in the carrier collection efficiency is due to more light being absorbed in the absorber than in the buffer layer where electrons are blocked by the wide bandgap barrier layer. Above 2 μm, the collection efficiency decreases due to the diffusion-length limitation. As a result, there is an optimum thickness that balances these opposing effects, which in this case is ~ 3 μm.

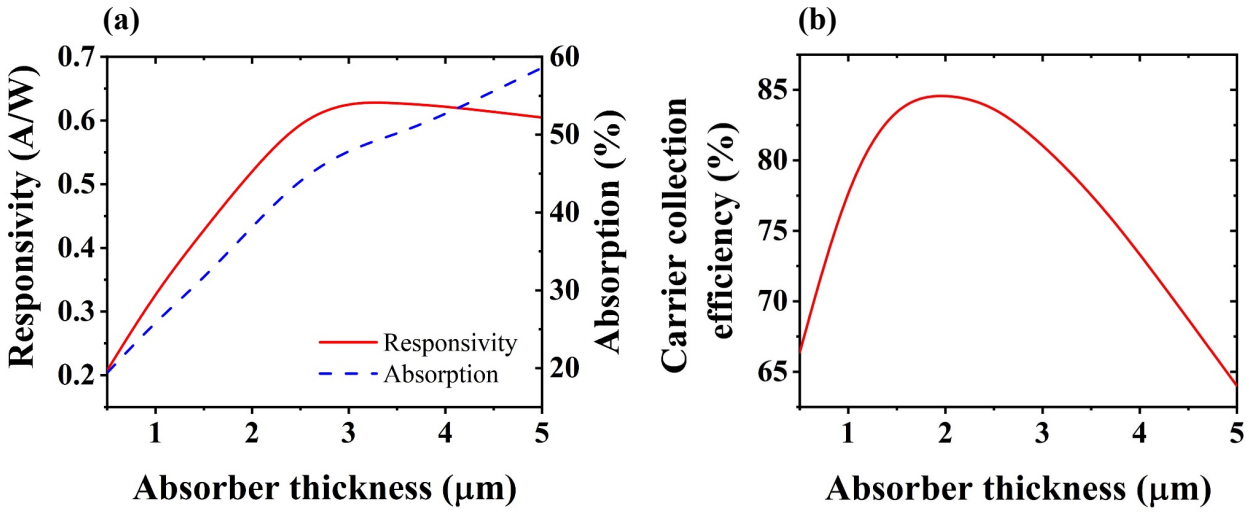

Fig. 3.2-3 (a) Simulated responsivity and absorption and (b) carrier collection efficiency of the AlInAsSb nBn photodetector versus absorber thickness under 2-μm illumination. The absorber, barrier and buffer layer are assumed to be unintentionally doped with an n-type background doping concentration of 1×10^{16} cm^{-3}; the simulation temperature is 300 K.

The doping concentration in the absorber affects the depletion width, electric field, carrier lifetime, and the dark current. Fig. 3.2-4 shows the simulated responsivity of the device with different n-type doping concentrations in the $Al_{0.3}InAsSb$ absorber and the buffer layer. The barrier layer is unintentionally doped. The responsivity decreases as the doping concentration increases, which is primarily due to the decreased depletion width when the doping concentration in the absorber is high.

As a result, the electric field intensity will be higher on one side, which will give rise to SRH recombination and tunneling, and a decreased responsivity as a result of reduced carrier lifetime. High n-type doping may also decrease the carrier lifetime of holes through band-to-band recombination in the undepleted region. Therefore, lower doping concentration in the absorber and buffer layers is preferred and is designed to be unintentionally doped. For the device reported here the n-type background doping concentration was approximately 1×10^{16} cm^{-3}. Modifying the doping polarity and concentration in the barrier layer has been reported to minimize the valence band discontinuity, so as to increase the hole diffusion length and reduce the turn-on voltage.[59] However, since AlInAsSb has minimal valence band discontinuity, the barrier layer doping was not considered.

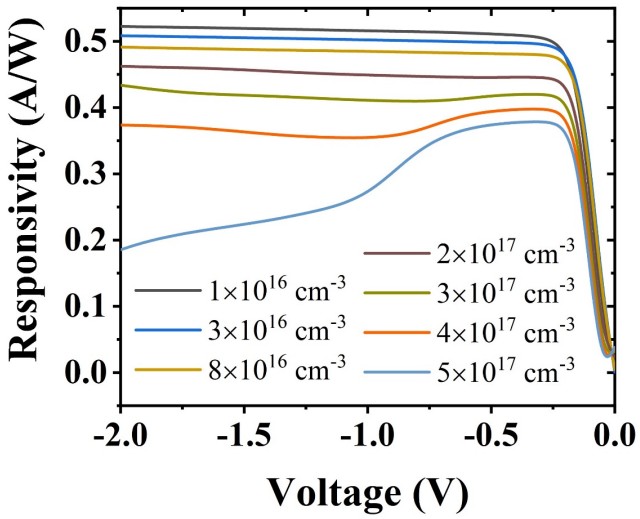

Fig. 3.2-4 Simulated responsivity versus voltage of the AlInAsSb nBn photodetector with different n-type doping concentrations in the absorber and the buffer layer.

3.3. Fabrication and characterization

The structure shown in Fig. 3.2-1 was grown by MBE as a digital alloy of three binary constituents: AlSb, InAs, and InSb lattice matched to an n-type GaSb substrate. Devices were

fabricated into circular mesa structures by citric acid wet etching using standard photolithography techniques, and SU-8 was used for surface passivation. Finally, current-voltage (I-V), capacitance-voltage (C-V), external quantum efficiency (EQE), and low-temperature dark current measurements were performed to characterize the performance of the device.

Fig. 3.3-1 (a) shows the room-temperature I-V characteristics of the AlInAsSb nBn photodetector. The photoresponse is measured under 2-μm laser illumination. The dark current density is ~ 2.6×10^{-3} A/cm^2 at -0.5 V and ~ 2.7×10^{-3} A/cm^2 at -1 V. Based on the I-V measurement, the detectivity was determined from the differential-resistance-area product, 1/RA, to be 1.7×10^{10} Jones at room temperature.. It also worth noting that the forward dark current is lower than the reverse dark current at low bias but shows a faster rise with bias. This can be understood by comparing Fig. 3.2-2 (b) and (c). Due to the asymmetric design of the nBn photodetector, the buffer layer is much thinner than the absorber. Therefore, at low bias, the forward dark current, determined by the thin buffer later, should be lower than the reverse dark current, determined by the thick absorber. However, as shown in Fig. 3.2-2 (c), the depletion is confined in the thin buffer layer even when the forward bias increases. As a result, the electric field is high, which finally leads to a rapid increase in SRH-generated dark current. This trend is consistant with the C-V measrement shown in Fig. 3.3-1 (b) where the forward capacitance is much higher than the reverse capacitance, which is caused by the narrower depletion width under forward bias. Similarly, the forward photocurrent is also lower than the reverse photocurrent since the majority of the light is absorbed in the thick absorber but the generated photocarriers are blocked by the barrier layer.

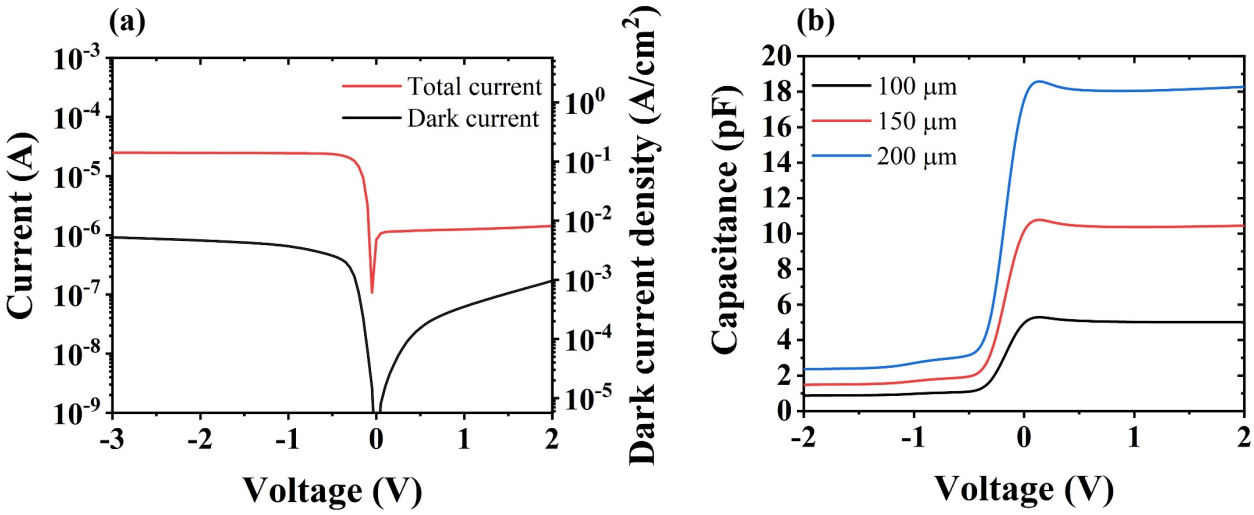

Fig. 3.3-1 (a) Measured I-V curves of a 150-µm diameter AlInAsSb nBn photodetector at room temperature; total current was measured under 2-µm laser illumination. (b) Measured C-V curves of AlInAsSb nBn photodetectors with different mesa diameters.

Fig. 3.3-2 (a) shows the measured room-temperature EQE. The device exhibits a cutoff wavelength of ~ 2.1 µm, consistent with previous work on 2-µm AlInAsSb APDs using the same absorber material [8]. The fast decrease of the EQE around 2 µm is primarily due to the decreasing absorption coefficient as the photon energy approaches the bandgap energy of $Al_{0.3}InAsSb$, which is similar to the behavior of T2SL detectors near cutoff. The saturated EQE at 2-µm is ~ 28%, close to the simulated EQE of ~32%. Note that there is no anti-reflection (AR) coating on the device surface. Since the top $Al_{0.3}InAsSb$ layer should have a reflectivity of ~ 31% at 2-µm, the EQE could be increased to ~ 40 % with a 1%-reflectivity AR coating. Moreover, by comparing the simulation shown in Fig. 3.2-3, the EQE could also be further enhanced by increasing absorber thickness to ~ 3 µm, which with an AR coating would yield an EQE of ~ 50% at 2-µm.

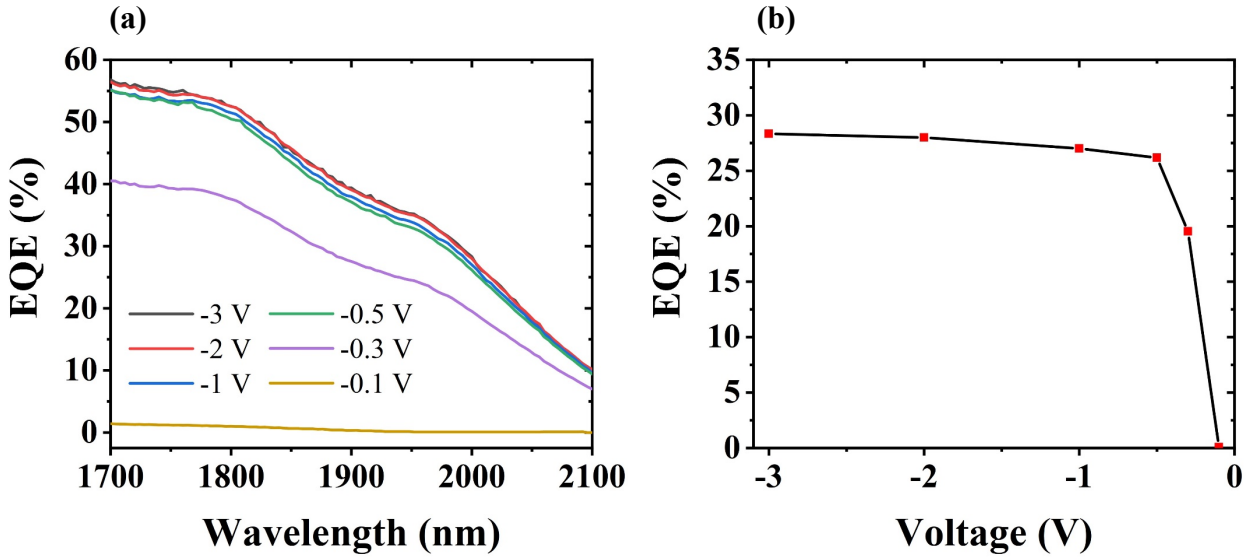

Fig. 3.3-2 (a) Room temperature measured EQE of a 250-µm diameter AlInAsSb nBn photodetector versus wavelength for reverse bias from -0.1V to -3V. (b) EQE at 2-µm versus reverse bias voltage.

Fig. 3.3-2 (b) shows a clear turn-on behavior at approximately -0.5 V. This turn-on characteristic reflects the voltage needed to overcome carrier trapping, especially in the valence band. [59] Since AlInAsSb has a minimal valence band discontinuity with different Al compositions, the turn-on characteristic shown here is likely caused by the barrier formed by the interface of the UID buffer layer and the highly doped N contact layer, as shown in Fig. 3.2-2 (b). This is different from a conventional nBn detector where the valence band discontinuity at the barrier layer also plays an important role. The turn-on voltage can be reduced, which will enable zero-bias operation, by modifying the doping concentrations in the contact layer and the buffer layer.

To better compare the dark current of the AlInAsSb nBn detector to conventional nBn detectors, the low temperature dark current was measured in a cryogenic chamber from 80 K to 340 K. Fig. 3.3-3 (a) shows the dark current density versus bias voltage and the dark current density versus the

inverse temperature in Fig. 3.3-3 (b). The dashed line in Fig. 3.3-3 (b) shows a fit to the diffusion-current-limited regime using the relation,

$$J_{diff} \propto T^3 \exp\left(\frac{-\Delta E}{kT}\right)$$

where T is temperature, k is Boltzmann constant, and ΔE is the activation energy. Fitting to this equation reveals background-limited infrared photo-detection (BLIP) temperatures of 180 K and 200 K and activation energies of ~ 0.41 eV and ~ 0.37 eV at -0.1 V and -0.3 V, respectively. These activation energies are between $E_g/2$ (0.29 eV) and E_g (0.58 eV) of $Al_{0.3}InAsSb$. For these devices the mesa was etched down to the bottom contact layer, resulting in a 2-µm deep sidewall. Compared with conventional nBn photodetectors, where the absorber and barrier layers are usually un-etched or partially un-etched with contact made to the absorber, the observed activation energies are most probably the result of the large sidewall exposure. Hence, lower dark current can be expected with an etch that does not fully extend through the absorber. While dark current densities lower than those of T2SL and T2SLS nBn detectors are observed, this is due in part to the larger bandgap energy of the AlInAsSb absorber. Further research with narrower bandgap AlInAsSb absorbers is left for future work.

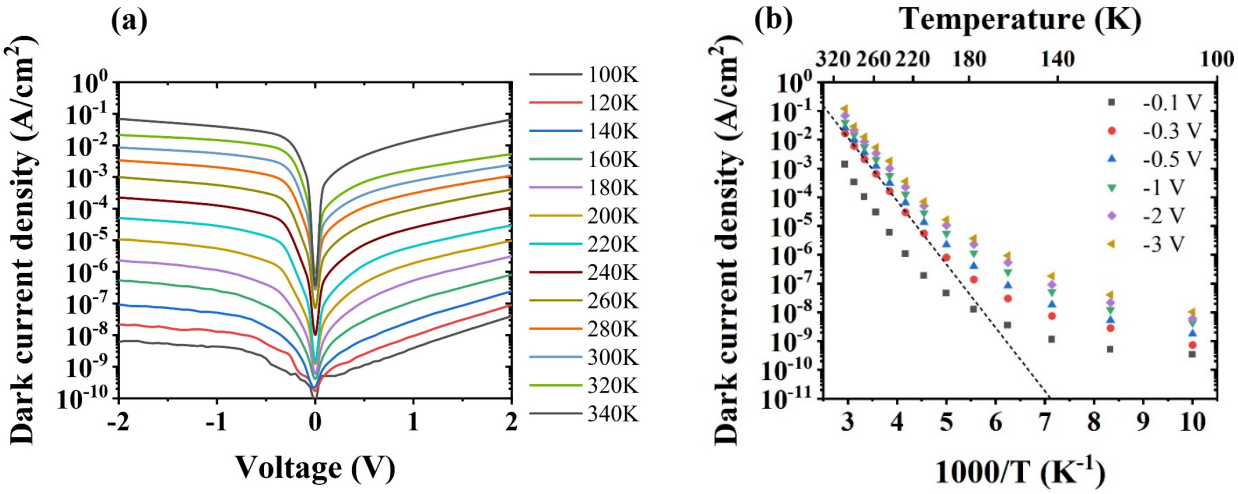

Fig. 3.3-3 (a) Measured dark current density of a 150-μm diameter AlInAsSb nBn photodetector at different temperature. (b) Measured dark current density as a function of inverse temperature. The dashed line shows the fitting to the diffusion-current-limited regime.

In summary, the first nBn photodetectors based on AlInAsSb digital alloy is demonstrated in this work. This new material system has the benefit of near-zero valence band offset, which is highly favorable for the hole transport required to achieve high detectivity and low turn on voltage. For 2 μm illumination the external quantum efficiency is 28%. The dark current densities are 2.6×10^{-3} A/cm^2 at 300 K and 1.8×10^{-9} A/cm^2 at 100 K with -0.5 V bias, and detectivity is 1.7×10^{10} Jones at room temperature. Work on extending the device to a longer operating wavelength is left for future work.

3.4. Bandwidth characterization and analysis

Much of the research on nBn photodetectors has focused on achieving lower dark current, higher quantum efficiency and longer detection wavelength. However, there have not been studies of the frequency behavior and bandwidth of nBn photodetectors except for a few pulse response reports [60, 61]. With rapidly expanding applications in the MWIR and LWIR spectral ranges, device speed is attracting more and more attention [62], such as for high-speed imaging [63, 64], MWIR frequency combs [3, 65, 66] and LIDAR systems [67]. Therefore, a thorough understanding of the frequency behavior of the nBn photodetector is important.

In this section, I investigate the frequency characteristics of the AlInAsSb nBn photodetectors reported in reference [68], by bandwidth, capacitance-voltage and microwave scattering parameters (S-parameters) measurements. Subsequently, a new equivalent circuit model is developed for the nBn photodetector to further understand its frequency behavior and the limiting factors of its

bandwidth. To my knowledge, this is the first detailed analysis of the frequency behavior of nBn photodetectors. This work provides a framework for understanding the bandwidth performance of nBn photodetectors, which can be used for further optimization of nBn photodetectors for high-frequency applications in the MWIR and LWIR spectral range.

The epitaxial structure of the $Al_{0.3}InAsSb/Al_{0.7}InAsSb$ nBn photodetector is shown in Fig. 3.4-1. The structure was grown by MBE as a digital alloy of four binary constituents: AlAs, AlSb, InAs, and InSb lattice matched to an n-type GaSb substrate [69]. Details regarding the fabrication of the device are included in reference [68]. It is worth noting that no coplanar waveguide (CPW) pad was designed for these devices. The frequency response was measured by directly probing the top and bottom metal contacts using a ground-signal (G-S) probe, as shown in Fig. 3.4-1.

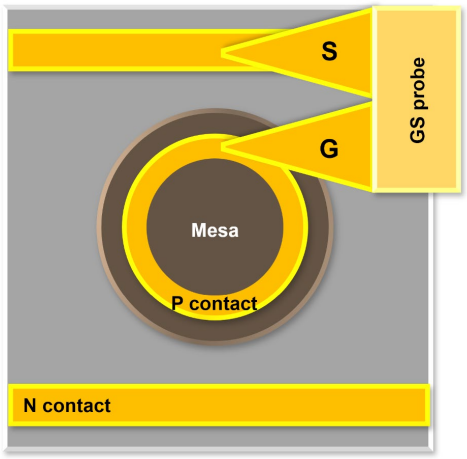

Fig. 3.4-1 Schematic of directly probing the nBn photodetectors using a G-S probe.

Fig. 3.4-2 shows a schematic of the experimental setup for the frequency response measurement. The setup is basically identical to the setup discussed in section 2.6, with the only difference that the coupling is through surface normal rather than edge coupling. The S_{11} of the device was measured

by the same setup without laser illumination to further study the equivalent circuit model of the nBn photodetector. Circuit and probe loss have been calibrated for the measurement.

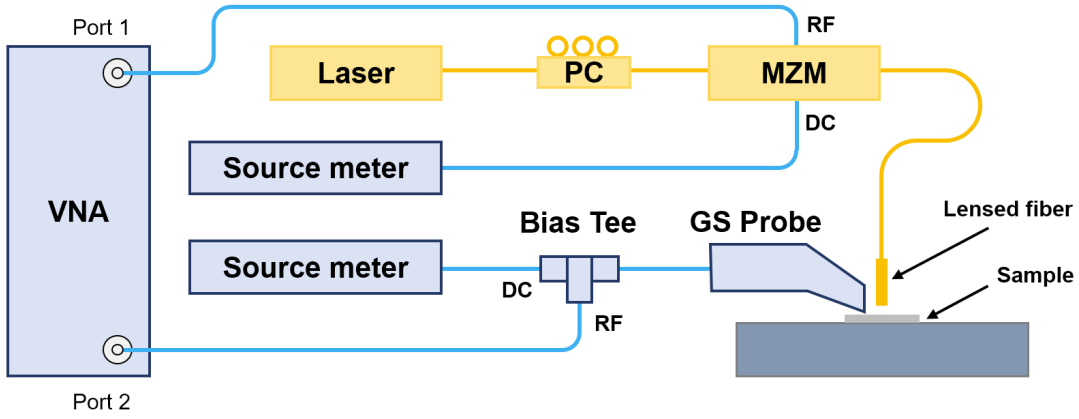

Fig. 3.4-2 Setup schematic of the frequency response measurement

Fig. 3.4-3 shows the normalized response of the nBn photodetectors measured from 20 MHz to 3 GHz. The 3-dB bandwidth was extracted and plotted in Fig. 3.4-4. Devices with varying device diameters show a similar bandwidth saturation phenomenon, where the bandwidth initially increases with bias voltage but then quickly saturates beyond ~ -0.5 V. It is worth noting that the bandwidth saturation voltage is exactly equal to the turn-on voltage of the nBn photodetectors as discussed in [68], which reflects the voltage needed to overcome carrier trapping [59, 70]. Therefore, it appears that the bandwidth of the nBn photodetector saturates immediately after the device turns on.

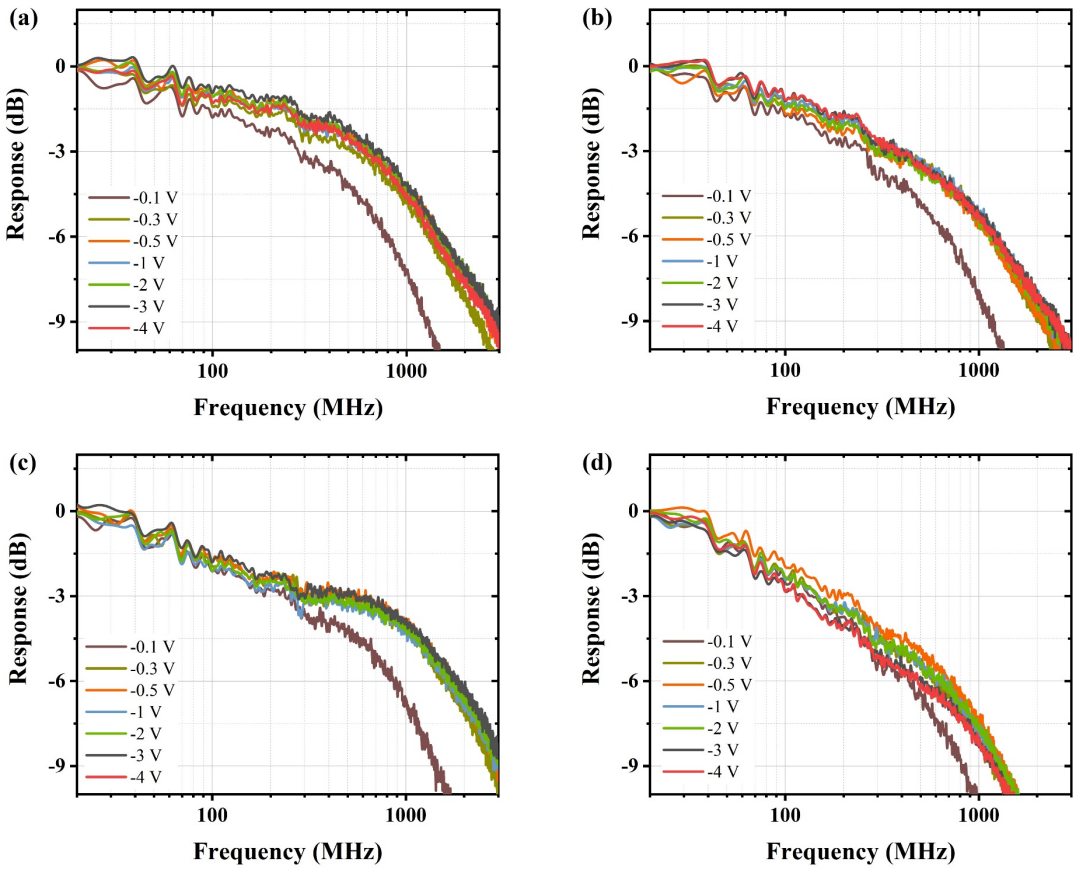

Fig. 3.4-3 Frequency response of AlInAsSb nBn photodetectors with device diameters of (a) 80 µm (b) 100 µm (c) 150 µm (d) 200 µm at various bias voltages. Photocurrent is set to 10 µA.

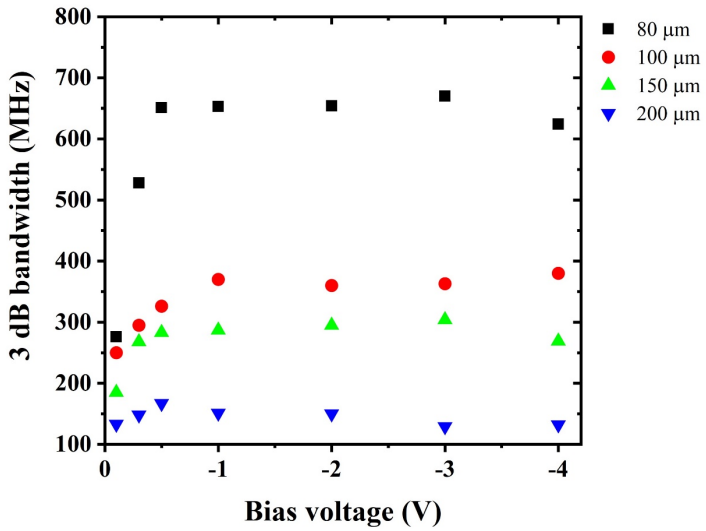

Fig. 3.4-4 3-dB bandwidth of AlInAsSb nBn photodetectors with various device diameters and bias voltages. Photocurrent is set to 10 μA.

Theoretically, the bandwidth of a photodiode is limited by the carrier transit-time and the resistance-capacitance (RC) time constant, as expressed by the equation

$$f_{3dB} = \sqrt{\frac{1}{\frac{1}{{f_{RC}}^2} + \frac{1}{{f_{TR}}^2}}} \quad (1)$$

where f_{3dB} is the total 3-dB bandwidth of the device, f_{TR} is the transit-time limit bandwidth, and f_{RC} is the RC bandwidth [71]. One of the factors that can limit the bandwidth of an nBn photodetector is the long transit-time due to slow carrier diffusion through the thick absorber. However, as shown by the band diagram and electric field simulation in Fig. 3.4-5, more than half of the absorber remains undepleted when the device is turned on at ~ -0.5 V. As the depletion width and electric field extend further into the absorber, the transit-time bandwidth should increase since more photogenerated carriers begin to drift rather than diffuse. To verify this, the transit-time bandwidth of the nBn photodetector was simulated using the Lumerical Charge solver [72], and the result is shown in Fig. 3.4-6. As expected, the transit-time bandwidth continues to increase with bias voltage even beyond the turn-on voltage. It is also worth noting that the value of the simulated transit-time bandwidth is far above the measured 3-dB bandwidth. Therefore, it appears that the bandwidth of the nBn photodetector is not limited by transit-time.

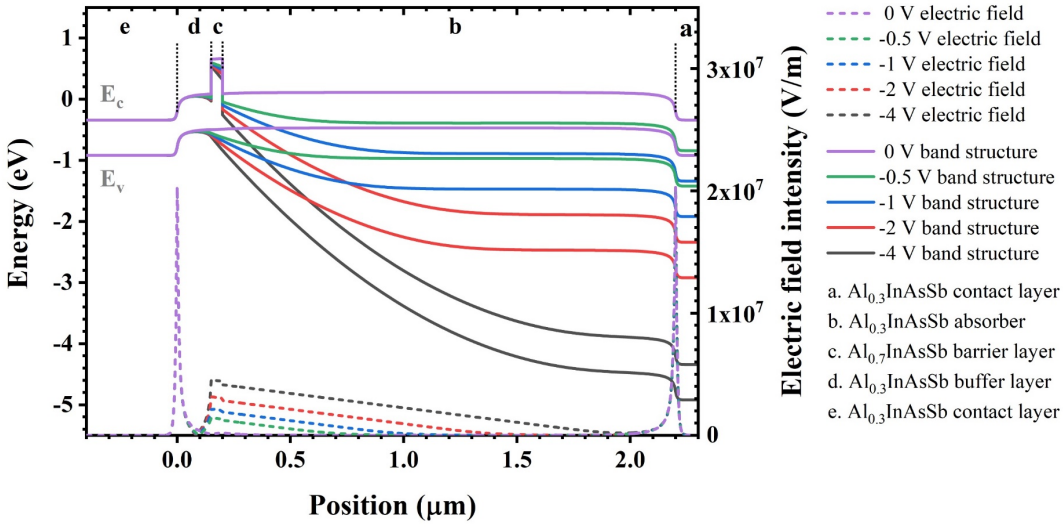

Fig. 3.4-5 Band diagram and electric field profiles of AlInAsSb nBn photodetectors at various bias voltages. The simulation is performed under dark condition.

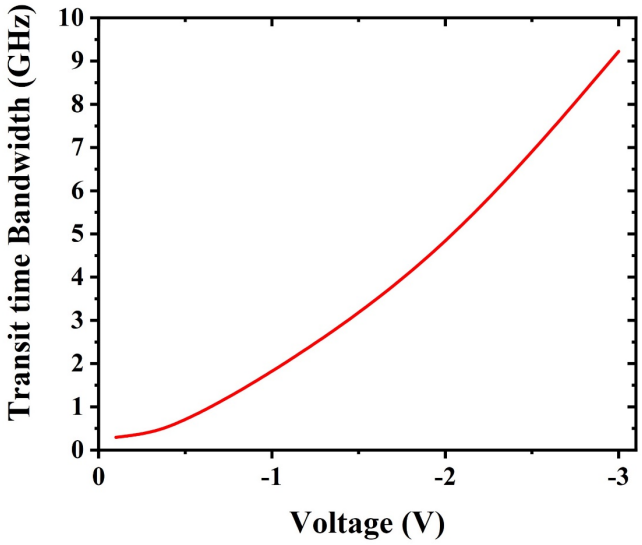

Fig. 3.4-6 Simulated transit-time bandwidth versus bias voltage curve for AlInAsSb nBn photodetectors.

Another possible limiting factor is the RC-limited bandwidth. The equivalent circuit of a typical P-I-N photodiode is as shown in Fig. 3.4-7, and the RC-limited bandwidth is expressed by the

equation

$$f_{RC} = \frac{1}{2\pi C_j (R_s + R_L)} \tag{2}$$

where C_j is the junction capacitance formed in the depleted intrinsic region, R_j is the junction resistance which is hundreds of megaohms and can be regarded as an open circuit, and R_s and R_L are the series resistance and the load resistance, respectively. To study the RC-limited bandwidth of the nBn photodetector, capacitance-voltage (C-V) curves were measured using an LCR meter at a frequency of 10 kHz. Theoretical junction capacitance was also calculated by assuming a parallel plate capacitor model as expressed by equation

$$C = \frac{\varepsilon \pi \left(\frac{d}{2}\right)^2}{w_d} \tag{3}$$

where C is the theoretical junction capacitance, ε is the permittivity, d is the device diameter, and w_d is the depletion width [73]. As shown in in Fig. 3.4-8, the measured total capacitance and the theoretical junction capacitance show good agreement. Then, by assuming a load resistance of 50 Ω and negligible series resistance, the theoretical RC bandwidth of the nBn photodetectors was calculated based on the photodiode circuit model (equation (2)) and the measured capacitance (Fig. 3.4-8). However, as shown in Fig. 3.4-8, the theoretical RC bandwidth calculated using this model is significantly higher than the measured 3-dB bandwidth. The discrepancy indicates that the nBn photodetector is likely to have a different equivalent circuit model compared to a P-I-N photodiode. A new equivalent circuit model is needed to understand the bandwidth of the nBn photodetector.

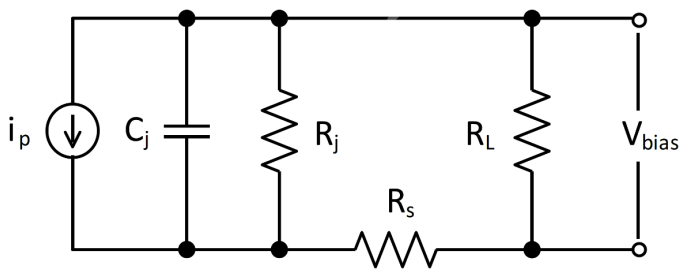

Fig. 3.4-7 Equivalent circuit model of a typical P-I-N photodiode

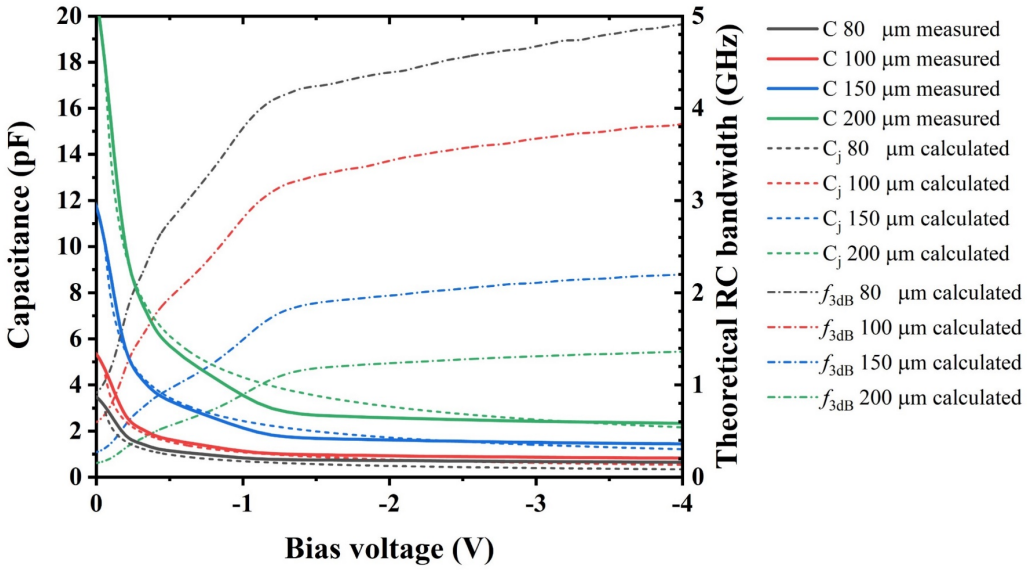

Fig. 3.4-8 Measured capacitance-voltage curves by a LCR meter at a frequency of 10 kHz and calculated theoretical junction capacitance of AlInAsSb nBn photodetectors with different device diameters.

Recall in Fig. 3.4-1 that the nBn photodetector is an N-I-N structure composed of an unintentionally doped (UID) region (buffer, barrier, and absorber layers) sandwiched between two n-type contact layers. As shown in Fig. 3.4-5 (a), this structure is similar to a phototransistor where one forward-biased junction is connected to a reverse-biased junction in series. Therefore, it is likely that the equivalent circuit model of an nBn photodetector is similar that of a phototransistor. As

studied in reference [74], the equivalent circuit model of a phototransistor is shown in Fig. 3.4-9 (a) , and the RC-limited bandwidth is expressed by the equation

$$f_{RC} \cdot (G+1) = \frac{1}{2\pi\left[R_e(C_e + C_c) + (R_L + R_s)C_j\right]} \tag{4}$$

where C_e and C_c are emitter diffusion capacitance and collector junction capacitance, respectively; R_e is the diffusion resistance between the emitter and the base; and R_L is the load resistance. Since phototransistors have internal gain, the left part of the equation expresses the gain-bandwidth product where G is the photogain.

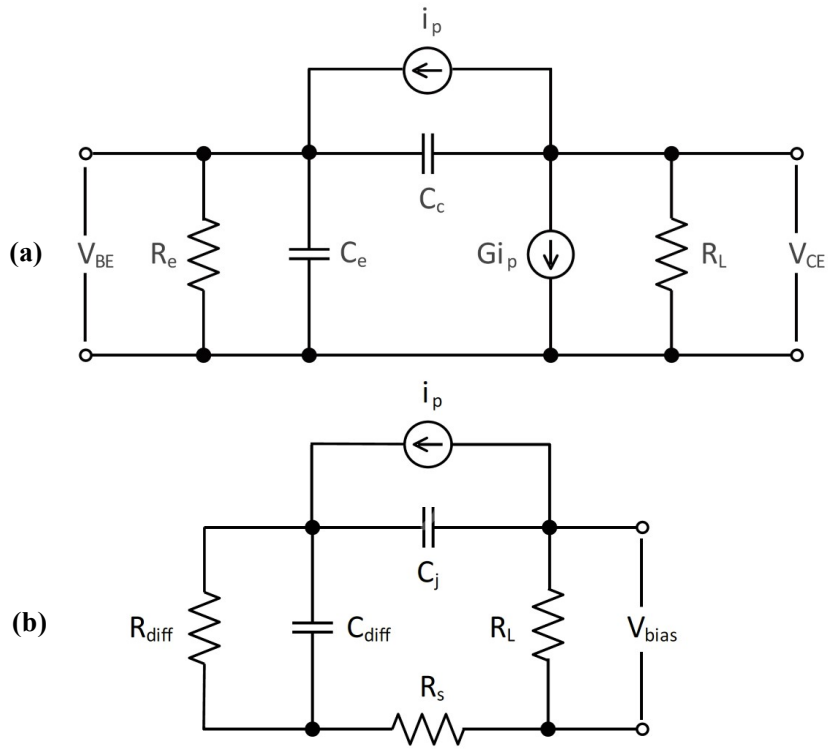

Fig. 3.4-9 Equivalent circuit model of (a) an N-P-N phototransistor [74] and (b) an nBn photodetector

Although the band structures are similar, nBn photodetectors are intrinsically different from phototransistors due to the barrier layer that blocks the majority carriers from diffusing into the absorber. As a result, the multiplied photocurrent Gi_p that results from these majority carriers in a phototransistor does not contribute to the total current in an nBn photodetector and therefore should be left open in the circuit model. Correspondingly, the gain-bandwidth product $f_{RC} \cdot (G+1)$ in equation (4) should be reduced to the RC bandwidth f_{RC}. Based on these modifications, the equivalent circuit model of an nBn photodetector is shown in Fig. 3.4-9 (b) with the RC bandwidth expressed as

$$f_{RC} = \frac{1}{2\pi\left[R_{diff}\left(C_{diff}+C_j\right)+\left(R_L+R_s\right)C_j\right]} \quad . \tag{5}$$

The lumped elements in the equivalent circuit model of the nBn photodetector serve similar roles as in a phototransistor, but physically they originate from different sources and need to be discussed and re-defined as follows. Correspondence between the band structure and the equivalent circuit model is schematically plotted in Fig. 3.4-10 (a) to make the following discussion more understandable.

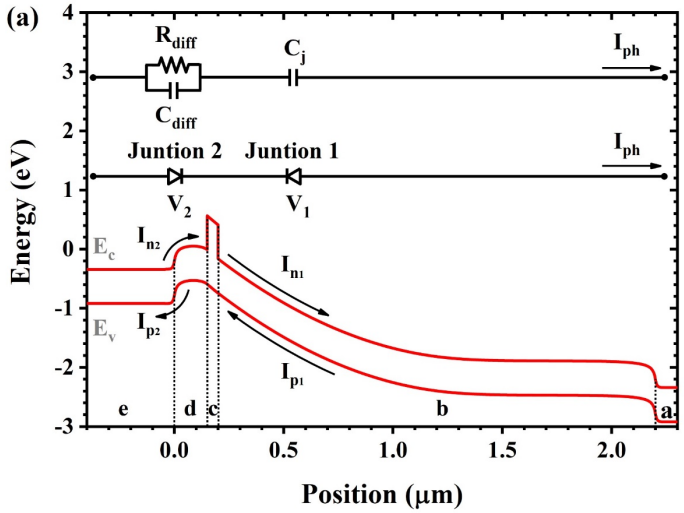

a. $Al_{0.3}InAsSb$ contact layer
b. $Al_{0.3}InAsSb$ absorber
c. $Al_{0.7}InAsSb$ barrier layer
d. $Al_{0.3}InAsSb$ buffer layer
e. $Al_{0.3}InAsSb$ contact layer

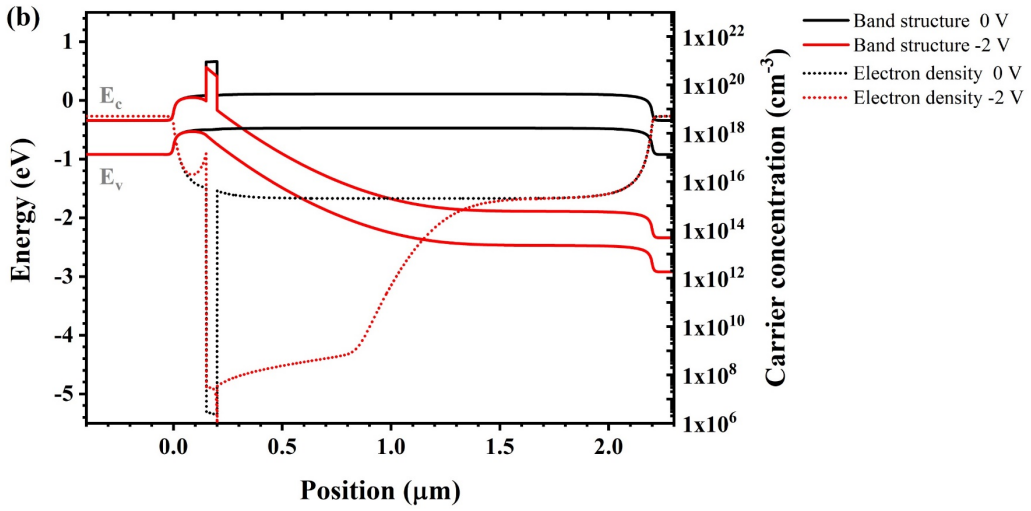

Fig. 3.4-10 (a) Correspondence between the band structure and the new equivalent circuit model for nBn photodetectors. (b) Band diagram and electron carrier density distribution of AlInAsSb nBn photodetectors at equilibrium and under reverse bias. The simulation is performed under dark condition.

C_{diff}: diffusion capacitance formed by the stored charge near the bottom edge of the barrier layer. In a typical N-P-N phototransistor, the emitter diffusion capacitance exists due to the fact that the injected minority carriers accumulate under forward bias voltage. This leads to charge stored near both sides of the depletion region and forms a diffusion capacitance [74]. In an nBn photodetector, there is no p-type base region but a UID barrier layer instead. Nevertheless, the barrier layer has a similar effect on creating a diffusion capacitance. Since the barrier layer has a large conduction band offset, electrons that diffuse from the bottom contact layer to the absorber will be blocked. As shown in Fig. 3.4-10 (b), blocked electrons accumulate near the bottom edge of the barrier layer. Since it takes time for the stored electrons to recombine with holes, these carriers create a diffusion capacitance. It is worth noting that the kink around 0.8 μm indicates the edge of the depletion region.

$\boldsymbol{R_{diff}}$: diffusion resistance of the forward biased junction between the bottom contact later and the UID region. In a typical N-P-N phototransistor, the diffusion capacitance is associated with the slope of current-voltage (I-V) curve for the forward-biased emitter-base junction. As shown in Fig. 3.4-10 (a), the junction between the bottom contact layer and the UID region in an nBn photodetector is forward biased and therefore the diffusion resistance in an nBn photodetector is similar to that of an N-P-N phototransistor.

$\boldsymbol{C_j}$: junction capacitance in the depleted absorber under reverse bias. This is similar to the junction capacitance in a P-I-N photodiode. According to the equivalent circuit model in Fig. 3.4-9 (b), the total capacitance C measured with an LCR meter is a series connection of C_j and C_{diff} if the measuring frequency is low:

$$\frac{1}{C} \cong \frac{1}{C_{diff}} + \frac{1}{C_j} \tag{6}$$

where C is the total measured capacitance. I found that the total capacitance C measured with an LCR meter stabilizes when the frequency is lower than ~ 100 kHz. As shown in Fig. 3.4-8, the measured total capacitance at 10 kHz fits well with the theoretical junction capacitance. This agreement indicates that C_{diff} is likely to be much larger than C_j. Accurate characterization of C_j and C_{diff} will be addressed by the S-parameter fitting and will be discussed in the next section.

$\boldsymbol{R_s}$: series resistance of the device.

$\boldsymbol{R_L}$: load resistance in the measurement setup, set as 50 Ω in this work.

To accurately determine the value of each lumped element in the new equivalent circuit model, S_{11} parameters of the devices were measured. Fig. 3.4-11 shows the measured S_{11} parameters of the nBn photodetectors with different device diameters at various bias voltages, plotted on Smith Charts from 20 MHz to 5 GHz.

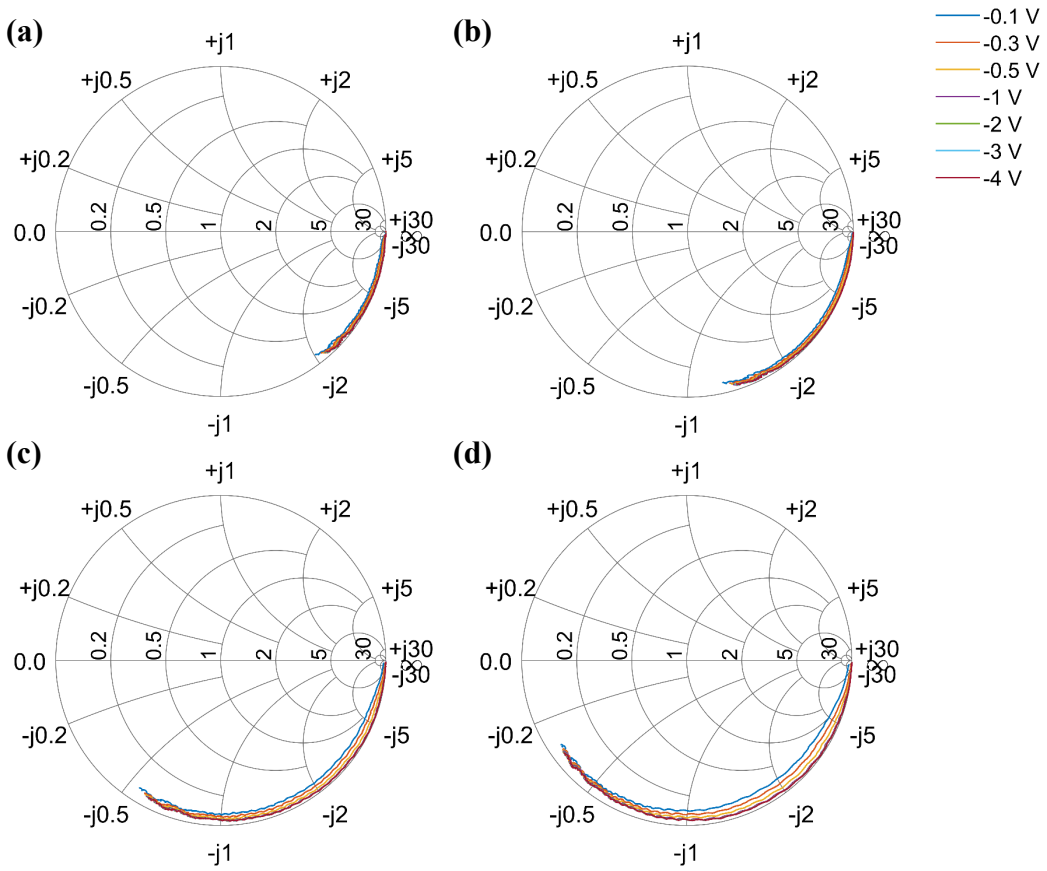

Fig. 3.4-11 Measured S_{11} curves of AlInAsSb nBn photodetectors with device diameters of (a) 80 μm (b) 100 μm (c) 150 μm (d) 200 μm at various bias voltages.

The measured S_{11} parameters show a similar saturation phenomenon as the bandwidth measurement, where S_{11} curves converge quickly after the turn-on voltage (~ -0.5 V). At the same time, a strong device area dependence also appears when comparing Fig. 3.4-11 (a) to (d), where larger devices have higher capacitance. To fit each lumped element, S-parameter fitting was performed using Keysight Advanced Design System (ADS) based on the equivalent circuit model shown in Fig. 3.4-9 (b). As shown in Fig. 3.4-12, simulated S_{11} curves show good agreement with the measured results. The fitted parameters at -2 V are summarized in Table 3.4-1 for different device diameters. Fitted parameters at other voltages are not listed since the measured S_{11} parameters converge beyond the turn-on voltage. To further verify the circuit model, the theoretical 3-dB

bandwidth of the nBn photodetectors was calculated using equation (5) and the fitted parameters in Table 3.4-1. As shown in Table 3.4-2, the theoretical 3-dB bandwidth also agrees well with the measured results.

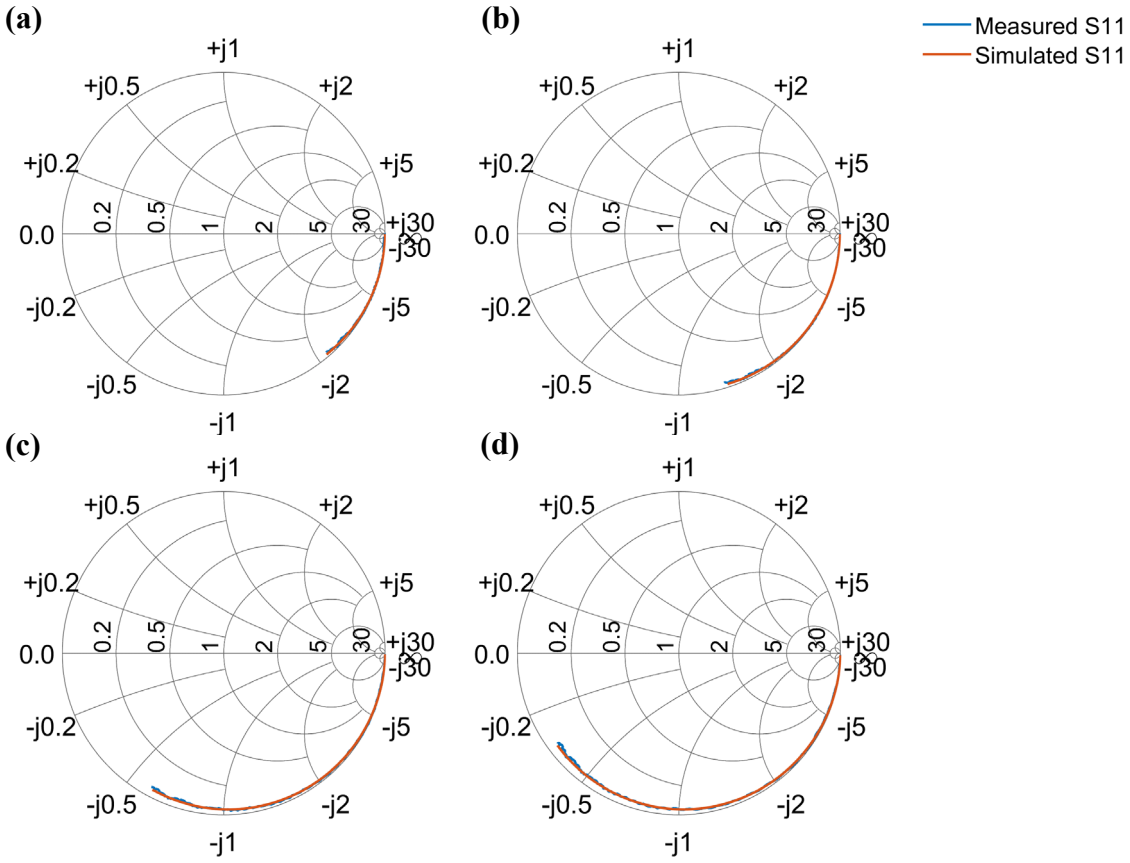

Fig. 3.4-12 Simulated S_{11} curves of AlInAsSb nBn photodetectors with device diameters of (a) 80 μm (b) 100 μm (c) 150 μm (d) 200 μm at a bias voltage of -2 V.

Table 3.4-1 Fitted parameters in the equivalent circuit model of an nBn photodetector

Device diameter	C_j	C_{diff}	R_s	R_{diff}
80 μm	0.30 pF	15 pF	2.1 Ω	14 Ω
100 μm	0.47 pF	25 pF	1.9 Ω	16 Ω
150 μm	1.08 pF	41 pF	1.6 Ω	12 Ω
200 μm	1.95 pF	65 pF	1.6 Ω	15 Ω

Table 3.4-2 Theoretical 3-dB bandwidth calculated by equation (5) and the fitted parameters in Table 1

Device diameter	f_{3dB} calculated	f_{3dB} measured
80 μm	678 MHz	654 MHz
100 μm	353 MHz	360 MHz
150 μm	283 MHz	295 MHz
200 μm	144 MHz	150 MHz

So far, the equivalent circuit model developed for the nBn photodetectors fits well with both the bandwidth and S_{11} measurements. However, it is worth noting that the fitted parameters in Table 3.4-1 show a different trend compared to a phototransistor, i.e., the diffusion capacitance of an nBn photodetector is proportional to the device area. For a typical N-P-N phototransistor, diffusion capacitance is proportional to photocurrent and carrier lifetime as expressed by equation

$$C_{diff} \propto I_{ph}\tau \tag{7}$$

where I_{ph} is the photocurrent and τ is the minority carrier lifetime. It is evident that C_{diff} is independent of device area because the diffusion capacitance is determined by the total current flow through the forward bias junction, which, in a phototransistor, is continuous with the photocurrent. However, nBn photodetectors have a barrier layer that blocks the diffusion of electrons into the absorber. As a result, the electron current is no longer continuous across the whole device; the electron current between the bottom contact layer and the barrier layer is the diffusion current of the majority carriers and should be much larger than the minority electron current in the absorber. On the contrary, hole current is still continuous since no barrier exists on the valence band. Based on this new current continuity condition, the diffusion capacitance and resistance of the nBn photodetectors can be qualitatively explained as follows.

As shown in Fig. 3.4-10 (a), assume voltage applied on the reversed biased absorber (junction 1) is V_1, and the electron and hole currents flowing through the junction are I_{n_1} and I_{p_1}, respectively. Likewise, voltage applied across the forward biased junction between the bottom contact layer and the UID region (junction 2) is V_2, and the electron and hole currents flowing through the junction are I_{n_2} and I_{p_2}, respectively; the photocurrent is I_{ph}. The hole current through the entire device is continuous. As a result,

$$I_{p_2} = I_{p_0}(e^{\frac{qV_2}{kT}} - 1) = I_{p_1} = I_{ph} \tag{8}$$

where I_{p_0} is the dark saturation hole current, q is absolute value of electron charge, k is Boltzmann's constant and T is absolute temperature.

Therefore, V_2 can be expressed as

$$V_2 = \frac{kT}{q}\ln\left(\frac{I_{ph}}{I_{p_0}} + 1\right) \tag{9}$$

Diffusion resistance of a forward biased junction is defined as the derivative of the voltage to current, therefore R_{diff} is expressed as

$$R_{diff} = \frac{dV_2}{dI_{ph}} \cong \frac{kT}{q}\frac{I_{p_0}}{I_{ph}} \propto \frac{1}{I_{ph}} \tag{10}$$

which shows that R_{diff} is inversely proportional to photocurrent I_{ph}.

Diffusion capacitance in a forward biased junction is expressed by equation (7). However, since electron current in an nBn photodetector is not continuous, current blocked at the barrier layer is no longer equal to photocurrent but is a majority current from the forward biased junction 2, and the electron current density J_{n_2} is

$$J_{n_2} = J_{n_0}(e^{\frac{qV_2}{kT}} - 1) \tag{11}$$

where J_{n_0} is the dark saturation electron current density.

It is worth noting that V_2 is still determined by the photocurrent, as shown in equation (9), to make the hole current continuous. Therefore, by substituting equation (9) into equation (11), we get

$$J_{n_2} \cong J_{n_0} \frac{I_{ph}}{I_{p_0}} \propto I_{ph} \tag{12}$$

which shows that electron current density at junction 2 is proportional to photocurrent.

The total electron current at junction 2 should be electron current density multiplied by the device area. Therefore, the expression of the diffusion capacitance in equation (7) should be modified to

$$C_{diff} \propto I_{n_2} \tau = J_{n_2} A \tau \tag{13}$$

where A is the area of the device.

Since electron current density J_{n_2} is proportional to I_{ph}, C_{diff} can be further modified by substituting equation (12) to be

$$C_{diff} \propto I_{ph} A \tau \tag{14}$$

which shows that the diffusion capacitance in an nBn photodetector is proportional to photocurrent, carrier lifetime, and device area.

In summary, the area dependence of the diffusion capacitance in an nBn photodetector originates from its barrier structure in the conduction band. As a result, the electron current is no longer continuous through the entire device, and therefore the electron current blocked at the barrier layer is not equal to the photocurrent (the minority current in the absorber). Instead, it is a majority current from the forward biased junction 2 that is proportional to the junction area and therefore results in the area-dependent diffusion capacitance. It is worth noting that photocurrent still affects the diffusion capacitance. However, it is not due to the photocurrent limiting the majority electron current blocked at the barrier layer but results from the photocurrent determining the voltage applied

on the forward biased junction 2 to make the hole current continuous. Therefore, the photocurrent affects the majority electron current blocked at the barrier layer indirectly. This process is similar to the origin of the photogain in a phototransistor, but the difference in an nBn photodetector is that the majority electron current from the forward biased junction no longer results in photogain. Instead, it is blocked by the barrier layer, stores charges there, and ultimately increases the diffusion capacitance.

After deriving the expression of the diffusion resistance and diffusion capacitance, the limiting factor of the bandwidth of the nBn photodetector can be deduced. As shown in Table 3.4-1, the diffusion capacitance in an nBn photodetector is significantly larger than the junction capacitance. Therefore, the limiting factor of the bandwidth, as shown in equation (5), should be the product of R_{diff} and C_{diff}. By substituting equation (10) and (14) into equation (5), the bandwidth expression of nBn photodetector can be simplified to

$$f_{RC} = \frac{1}{2\pi\left[R_{diff}\left(C_{diff} + C_j\right) + (R_L + R_s)C_j\right]} \cong \frac{1}{2\pi R_{diff} C_{diff}} \propto \frac{1}{A\tau} \tag{15}$$

It is worth noting that the influence of the photocurrent is canceled in equation (15), indicating that the bandwidth of an nBn photodetector should be unaffected by photocurrent level. This conclusion is clearly different from a phototransistor whose bandwidth is inversely proportional to the total photocurrent—described as the gain-bandwidth product—since the total photocurrent in a phototransistor is multiplied by the photogain [74]. To verify this conclusion, the frequency response of the AlInAsSb nBn photodetectors with diameters of 80 μm, 100 μm, 150 μm, and 200 μm are plotted in Fig 13 (a) to 13 (d), respectively at different photocurrent levels. As shown in Fig. 3.4-13, with a photocurrent that is two times higher, the frequency response curves of the AlInAsSb nBn photodetectors are almost the same, which agrees well with the prediction from equation (15).

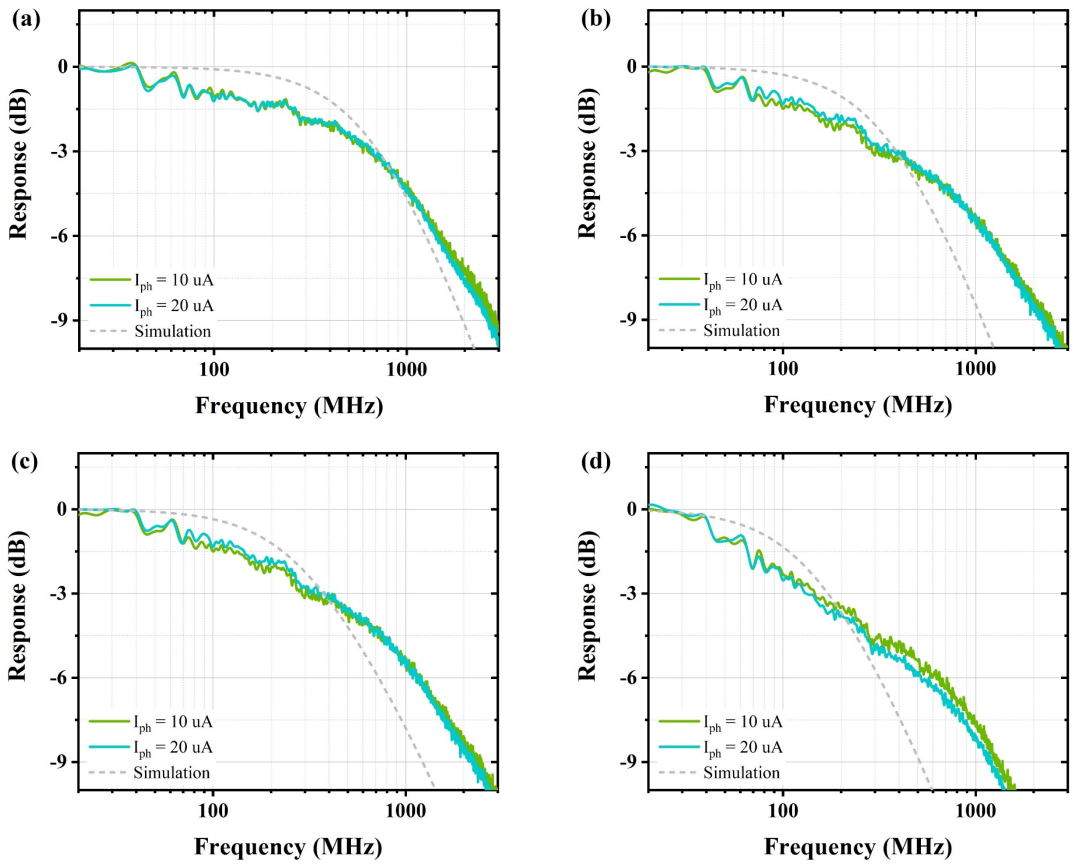

Fig. 3.4-13 Frequency response of AlInAsSb nBn photodetectors with device diameters of (a) 80 μm (b) 100 μm (c) 150 μm (d) 200 μm measured at different photocurrent levels; simulated frequency response is plotted in dash grey for reference; bias voltage is set at -2V.

Equation (15) also suggests possible means for improving the bandwidth of nBn photodetectors. The most straightforward method is to reduce the device area, which can reduce the majority electron current that diffuses to the barrier layer and therefore reduce the diffusion capacitance. The other possible method is reducing the minority carrier lifetime, which results in fast recombination of the accumulated carriers and therefore reduces diffusion capacitance. However, there can also be a negative aspect to this since long carrier lifetimes are preferred in an nBn photodetector in order to maintain enough diffusion length [68, 75]. Consequently, reducing carrier lifetime may result in lower quantum efficiency if the diffusion length drops below the absorption length. Therefore,

although the principles behind the bandwidth characteristic of an nBn photodetector and a normal-incidence photodiode are different, they have a similar intrinsic problem, i.e., the trade-off between the bandwidth and the quantum efficiency. Therefore, approaches such as waveguides [38-40] and surface photon trapping structures [11, 14, 76] that can improve the quantum efficiency without requiring a longer absorption length may be promising methods for achieving higher efficiency-bandwidth products for nBn photodetectors.

In summary, I report the frequency response of $Al_{0.3}InAsSb/Al_{0.7}InAsSb$ nBn photodetectors. The 3-dB bandwidth shows a strong RC time limit and saturates with bias voltage right after the device turn on. A new equivalent circuit model is developed for nBn photodetectors due to the discrepancy between their frequency behavior and the conventional photodiode equivalent circuit model. The theoretical bandwidth predicted by the new equivalent circuit model and the S-parameter fitting agree well with the measured results. Subsequent analysis further reveals that the limiting bandwidth factor of nBn photodetectors are carrier recombination lifetime and device area. Additionally, the bandwidth of nBn photodetectors is barely affected by photocurrent level, which is shown to result from the barrier structure in the conduction band. This work provides valuable insights into optimizing the frequency response of nBn photodetectors, which enable the expansion of its applications in high-speed scenarios in the MWIR and LWIR spectral range.

3.5. Future work

As discussed in section 3.3, a thin absorber is beneficial for nBn photodetectors. Firstly, the SRH generation dark current will be lower in a thin absorber. Secondly, carrier collection efficiency can also be improved because the distance that the photogenerated carriers have to diffuse through is less. Additionally, as discussed in chapter 3.4, thinner absorber is also preferred for high bandwidth

purpose. Nevertheless, thin absorber also leads to low absorption efficiency, and so that tradeoff need to be considered between these benefits and shortcomings. A promising method to break this limit is utilizing the photo trapping structures proposed in chapter 3, which can provide high quantum efficiency even with an ultra-thin absorber. Therefore, developing photo trapping structures on nBn photodetector will be a promising future work.

4. Double mesa APDs

4.1. Motivation

The background doping polarity and concentration is a critical parameter for designing MWIR photodetectors. For MWIR nBn photodetectors, since the absorber is mostly undepleted, background doping in the UID region will affects the minority carrier lifetime and so that affects the responsibility of the device. For MWIR SACM APDs, background doping is especially critical as the background doping polarity affects the electric field distribution in the absorber and multiplication layers and influences gain and dark current. Fig. 4.1-1 shows the band diagram comparison of a N-type background and P-type background SACM APD developed in chapter 2. It is evident that the electric field is much higher in the absorber if the background doping is N-type, and this will lead to a much higher dark current. Additionally, with respect to using double and triple mesa structures to reduce surface current in APDs [77, 78], the background doping polarity is especially important as it determines whether the depletion reaches the smaller mesa, thereby determining how much voltage is required to suppress the electric field at the periphery. This concept will be further studied in this chapter.

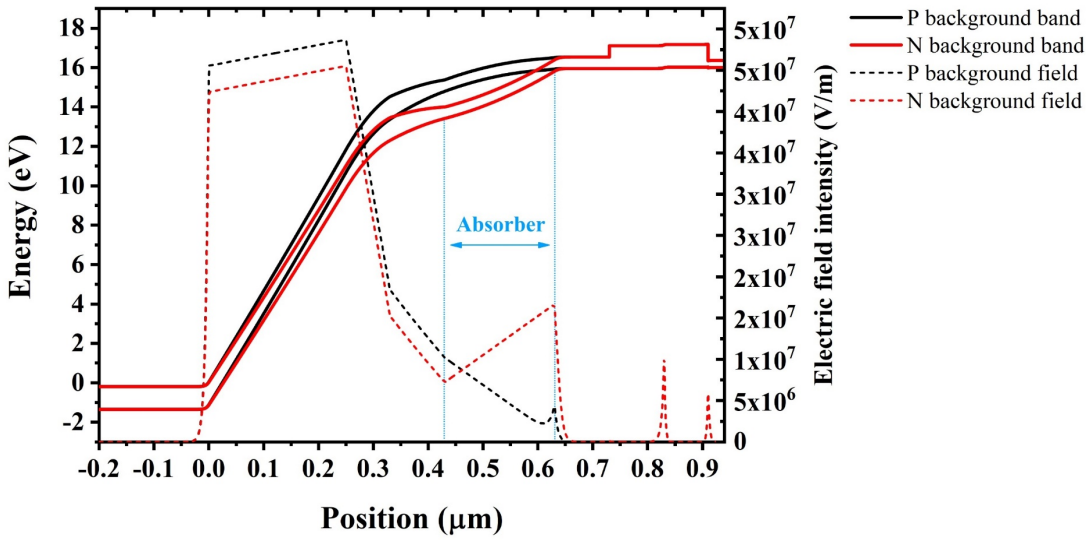

Fig. 4.1-1 Simulated band diagram and electric field profile with N-type and P-type background doping in the absorber.

Background carrier polarity is affected by various uncontrollable factors, many of which arise during the material growth process. Lattice structure, material constituents, and impurity incorporation based on vacuum quality and growth temperature are just a few of the factors that contribute to the defect type and density in a material. Taken together, these form a picture of total background doping that have big impacts on the material. This is often exacerbated for superlattice materials owing to the complex layer structures and interfaces, as well as the many constituents that form them[79, 80]. Digital-alloy based AlInAsSb is a short-period super-lattice structure composed of four binary alloys. Therefore it is critical to determine its background doping in order to accurately design complex APDs structures.

Various approaches have been employed to determine the background doping polarity and concentrations, such as Hall measurements [81], electrochemical capacitance–voltage (ECV) measurements [82] and secondary ion mass spectrometry (SIMS) [83]. Background doping is difficult to determine by Hall measurements on conductive substrates, such as GaSb due to a native point defect on which the AlInAsSb materials system is grown; ECV measurements are destructive to the device and limited by low measurement frequencies; and SIMS measurements require extensive calibrations and are often not accurate enough for low density atoms such background dopants.

Recently, a new approach for determining the background polarity was reported by performing capacitance–voltage (C-V) measurements on over-etched double mesa structures [84]. This approach is based on the dependence of capacitance with the cross sectional area of a p-n junction. As a result,

if fabricated with varying top and bottom mesa sizes, n-type and p-type background doping polarities manifest themselves as different capacitance relations to the diameter of either the top mesa (for n-type) or the bottom mesa (for p-type). This approach has proved superior to conventional approaches as it is straightforward, nondestructive, and independent of substrate type.

In this chapter, the background doping polarity of p-i-n APDs based on $Al_{0.7}InAsSb$ will be investigated. The performance of devices with different background doping polarities was compared through C-V, and low-temperature measurements. These results lay the foundation for further design of APDs based on the AlInAsSb digital alloy and could be applied to other materials systems as well.

4.2. Determine background doping polarity by double mesa structure

Two homojunction p-i-n $Al_{0.7}InAsSb$ samples grown at different times were selected for this study. The layers of these samples were grown by molecular bean epitaxy as a digital alloy of four binary alloys AlAs, AlSb, InAs, and InSb lattice matched to GaSb substrate. As shown in Fig. 4.2-1., the samples were fabricated into double mesa structures with variations in the bottom and top mesa diameters. My convention for referring to the double mesa structures is given by d_{bottom_mesa} - d_{top_mesa}. For example, 200-150 μm represents a double mesa structure with a bottom mesa diameter of 200 μm and top mesa diameter of 150 μm. The mesas were formed by etching in citric acid wet etching which has shown good isotropic etching to AlInAsSb. SU8 was used for surface passivation. After fabrication, C-V characteristics were measured for many double mesa size combinations. Low temperature C-V measurements were also performed in a cryogenic chamber from 80 K to 350 K. In parallel, modeling tools in Lumerical software were used to simulate the electric field profiles in order to further understand the capacitance characteristics of the double mesa structures.

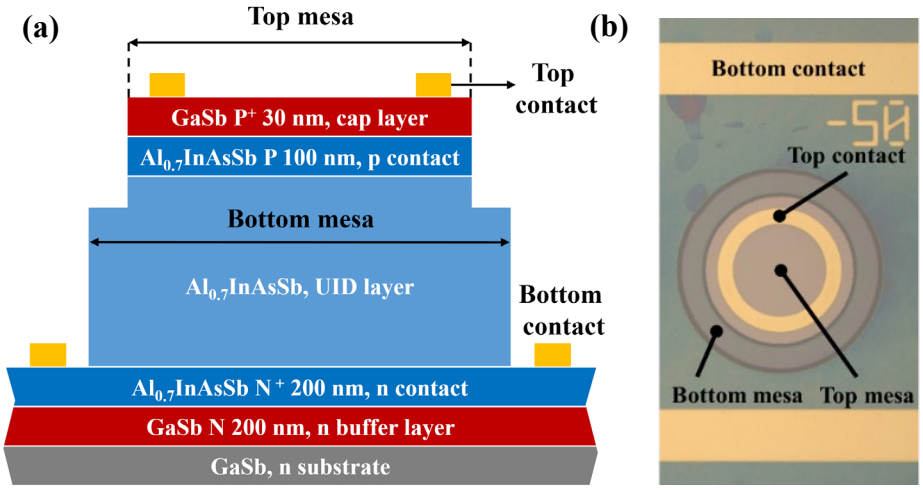

Fig. 4.2-1. (a) Schematic cross-section of the $Al_{0.7}InAsSb$ APDs with an over-etched double mesa structure and (b) Top view of a fabricated device. The doping concentrations are as follows: (1) GaSb P^+ 1×10^{19} cm^{-3}; (2) $Al_{0.7}InAsSb$ P 5×10^{18} cm^{-3}; (3) $Al_{0.7}InAsSb$, unintentionally doped; (4) $Al_{0.7}InAsSb$ N 5×10^{18} cm^{-3}; (5) GaSb N 1×10^{18} cm^{-3}; (5) GaSb substrate; The UID layer thickness is 1000 nm and 887 nm for sample A and sample B, respectively.

Different top and bottom mesa diameters were fabricated for this study. Fig. 4.2-2 shows the C-V curves of sample A with different mesa sizes. The background doping concentration can be estimated by the C-V curve to be around 3×10^{16} cm^{-3}. A notable trend is that the C-V curves behave differently at high and low bias voltages. At low bias, the capacitance is independent of the top mesa diameter, but begins to exhibit separation above -17 V. To further investigate this trend, the capacitance of the devices at -15 V and -30 V was extracted and is plotted in Fig. 4.2-3 with comparison to the theoretical capacitance. The red squares in Fig. 4.2-3 represents the measured capacitance of the double mesa structure with mesa diameter shown by the horizontal axis as well as the number inside the figure. The number represents the size of another mesa that is not marked by the horizontal axis. For example, the very left red square in Fig. 4.2-3 (a) represents the measured capacitance of a double mesa structure which has a top mesa diameter of 80 μm and a bottom mesa

diameter of 100 μm. The dashed line is the theoretical capacitance calculated using the following expression,

$$C = \frac{\varepsilon\pi(\frac{d}{2})^2}{w_d}$$

where C is the theoretical capacitance, ε is the permittivity, d is the mesa diameter, and wd is the depletion width. Figures 3 (a) and (b) show that below -17 V, the capacitance is a function of the bottom mesa diameter but independent of the top mesa diameter. The measured capacitance fits well with the theoretical capacitance calculated using the bottom mesa diameter, except that the measured capacitance is slightly higher. The reason for this is that, as indicated in Fig. 4.2-2, the device is not yet fully depleted at -15 V. This trend indicates a p-type background doping in the UID layer, which causes the depletion to begin from the p-n junction between the p-type UID layer and the N contact layer. As a result, the capacitance is determined by the area of the bottom mesa. However, this trend reverses at high bias. Beyond -17 V, the C-V curves of devices with different top mesa diameters begin to separate. It is worth noting that with the same bottom mesa diameter, devices that have smaller top mesas begin to show lower capacitance. As shown in Figures 3 (c) and (d), the capacitance is better determined by the top mesa diameter at -30 V and fits well with the theoretical capacitance calculated using these sizes. This is exactly opposite to the trend prior to -17 V.

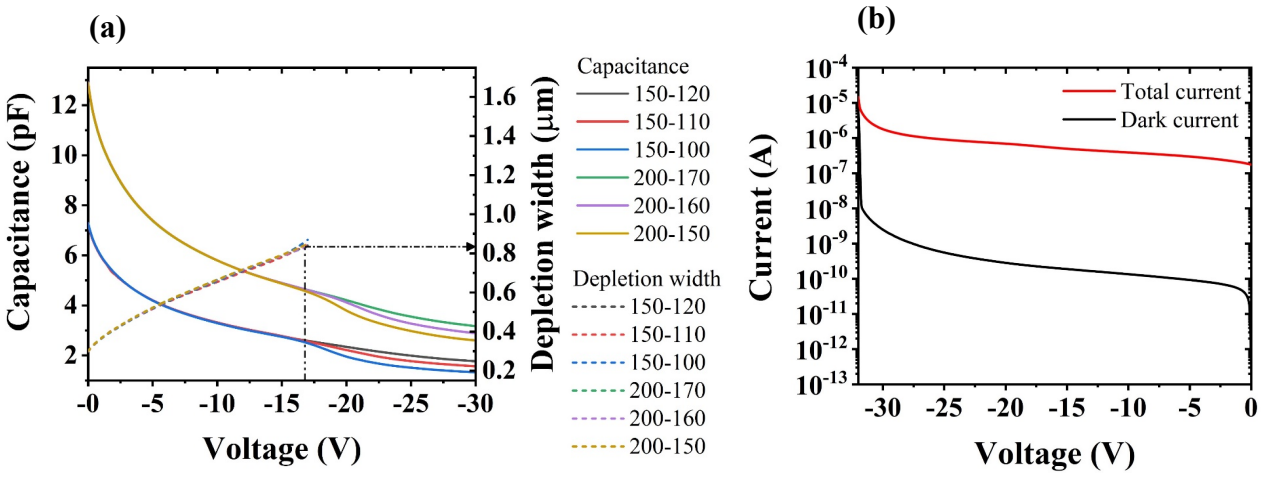

Fig. 4.2-2. Measured capacitance-voltage curves of double mesa devices with different top and bottom mesa diameters from sample A. The legend refers to the mesa size of d_{bottom_mesa} - d_{top_mesa} μm. (b) Current-voltage curves of a 150-100 μm double mesa device on sample A. The total current was measured under flood illumination with a lamp.

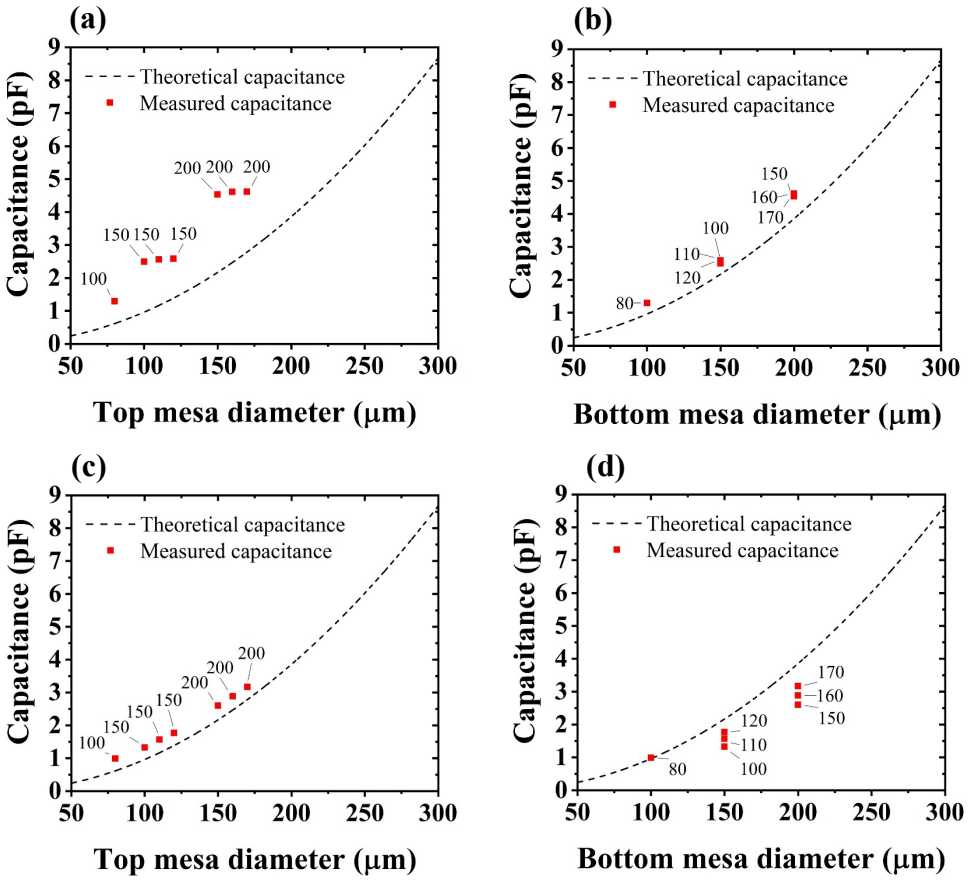

Fig. 4.2-3. Measured capacitance of double mesa devices from sample A compared with the theoretical capacitance calculated using either the top mesa diameter or bottom mesa diameter. The capacitance is measured at -15 V in (a) (b) and measured at -30 V in (c) (d). The number inside the figure represents the size of another mesa that is not marked by the horizontal axis.

To further understand the reversal of the capacitance behavior with respect to mesa area, the electric field profile within the device was simulated with the Lumerical CHARGE solver [] as shown in Fig. 4.2-4. At low reverse bias in Fig. 4.2-4 (a), high electric field develops around the p-n junction formed by the p-type UID layer and bottom N contact layer. This behavior matches Figures 3 (a) and (b) where the measured capacitance is determined by the bottom mesa, as the effective junction area is equal to the area of the bottom mesa. Then, as the reverse bias is increased further, the depletion reaches the narrower top mesa, and the electric field becomes confined beneath the top mesa. As a result, the capacitance begins to decrease with the decreasing effective area. This simulation closely follows the trend shown in Fig. 4.2-2. It follows that in order to determine the background polarity, it is better to analyze the capacitance at low bias when the effect of only one mesa dominates. Moreover, the depletion width at -17 V where the capacitance curves begin to separate is approximately 840 nm, which matches the measured between the bottom of the p-type UID layer to the top of the bottom mesa after etching, which further supports the finding of the simulation that the condition which causes the capacitance to decrease is the depletion width reaching the smaller top mesa. It is also worth noting that the capacitance at -30 V is slightly higher than the theoretical capacitance. This could be due to the high background carrier concentration of the device which prevents the device from fully depleting before it breaks down between -30 V and -31 V. On the other hand, the lateral field extension may also have an influence. As shown in Fig. 4.2-4 (c), there is still a portion of the electric field that extends beyond the confines of the top mesa region

even at high reverse bias. As a result, the effective junction area may be slightly larger than the top mesa area alone.

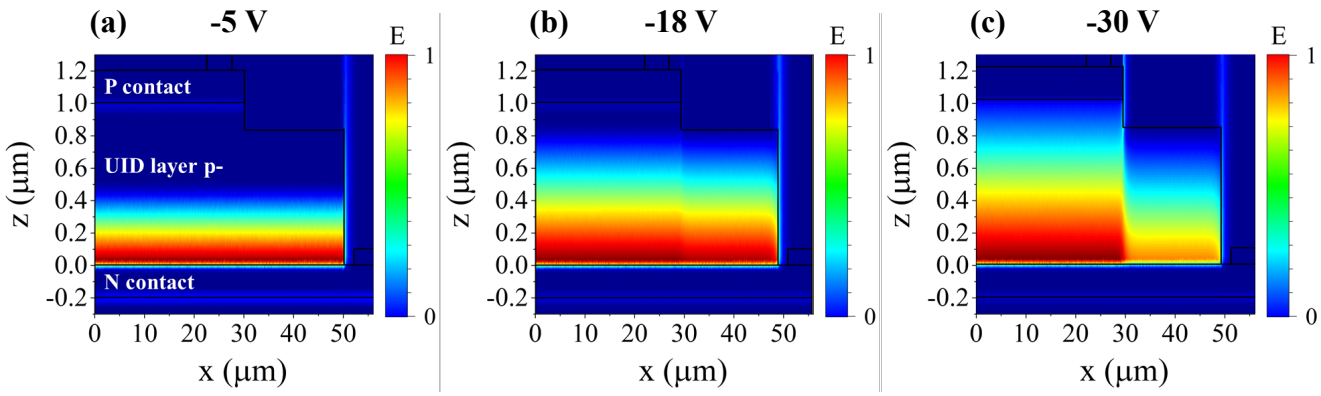

Fig. 4.2-4. Normalized distribution of the electric field magnitude E inside the double mesa devices from sample A (p-type background).

The decrease in the electric field at the periphery of the bottom mesa illustrated in Fig. 4.2-4 has been used to successfully reduce the surface leakage dark current in APDs with multiple mesas [77, 78]. Different from ion-implanted doping based guard ring techniques for CMOS-APDs [85, 86], this approach is based on mesa structure engineering and suitable for mesa-based APDs. Our analysis further shows that the basic condition for achieving low surface field and corresponding low surface leakage is that the depletion must extend to the smaller top mesa. Additional applied bias further extends the depletion region into the smaller mesa, leading to even stronger the electric field confinement and the lower the surface field will be. This is clearly shown by comparing Figures 4 (b) and (c). These results suggest that for a thick or highly doped p-type background depletion layer, a P-down (n-i-p-substrate) structure with the smaller mesa etched on the top N contact would be needed to reduce the surface field, so that the depletion can reach the smaller top mesa from the beginning. Otherwise, largely applied bias may be required before the depletion can reach the top mesa, limiting its effectiveness in reducing the surface field. This high voltage may cause the device

to break down before the low dark current can take effect. Similarly, for a thick or highly doped n-type background depletion layer, an N-down (p-i-n-substrate) structure with the smaller mesa etched on the top P contact would be needed in order to reduce the surface field.

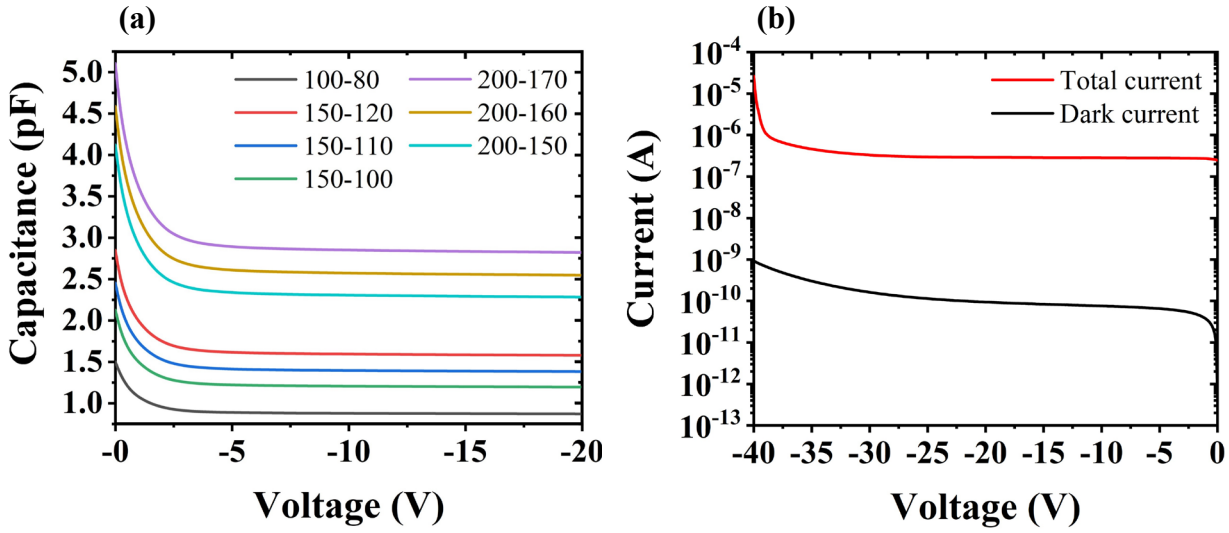

Fig. 4.2-5. Measured capacitance-voltage curves of double mesa devices with different top and bottom mesa diameters from sample B. The legend refers to the mesa size of d_{bottom_mesa} - d_{top_mesa} μm. (b) Current-voltage curve of a 150-100 μm double mesa device on sample A. The total current was measured under flood illumination with a lamp.

Fig. 4.2-5 shows the C-V curves of the devices from sample B with different mesa sizes. The background doping concentration can be estimated by the C-V curve to be around 6×10^{15} cm^{-3}. The C-V behavior of sample B is distinctly different from that of sample A. The measured capacitance of sample B varies with different top mesa sizes, unlike the bottom mesa dependence demonstrated by sample A. Similar to my analysis for sample A, the measured capacitance of sample B at -20 V is plotted with the theoretical capacitance in Fig. 4.2-6. It is evident that the capacitance has a clear dependence on the top mesa size and is independent of the bottom mesa diameter. This is a

characteristic of an n-type background device, where the depletion starts from the p-n junction between the n-type UID region and the P contact layer in the top mesa. The other difference is that the C-V curves of sample B do not separate at high bias, i.e., they behave like a single mesa p-i-n device. To investigate the mechanism for this difference, the electric field was simulated for the sample B devices shown in Fig. 4.2-7. The p-n junction forms at the interface between the top of the n-type UID layer and the bottom of the P contact layer within top mesa. As a result, the depletion initially forms in the top mesa, which determines the effective capacitor area. Contrary to the p-type background devices, the electric field inside the n-type background devices remains confined under the smaller top mesa even when the depletion extends into the bottom mesa. Therefore, the effective area does not change with the applied bias and no C-V curve separation is observed.

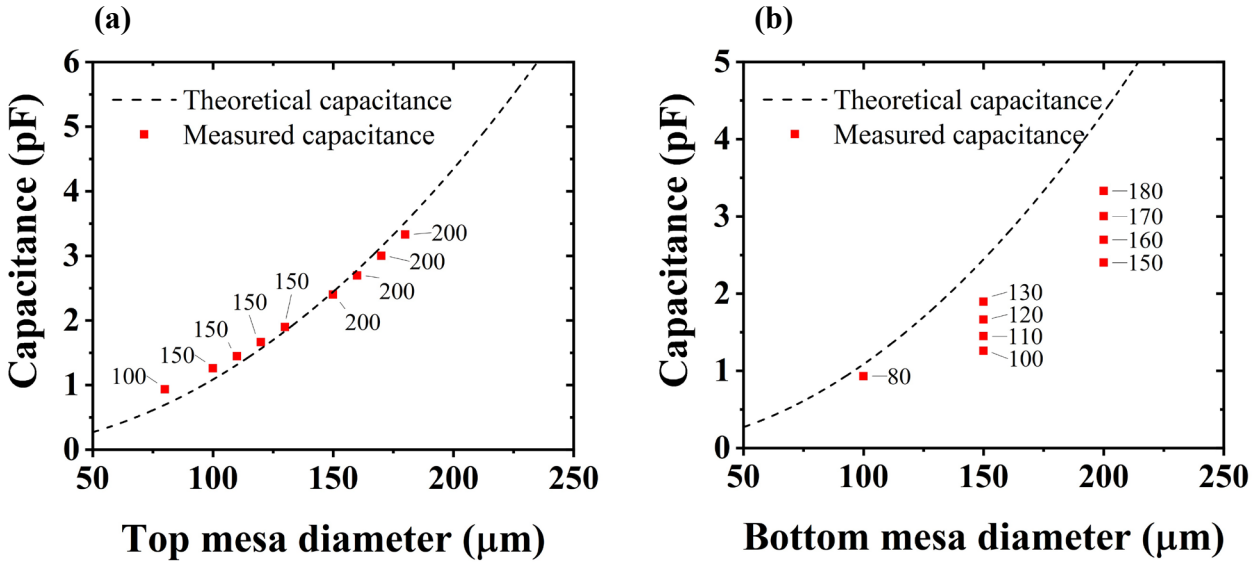

Fig. 4.2-6. Measured capacitance of double mesa devices from sample B compared to the theoretical capacitance calculated using either (a) top mesa diameter or (b) bottom mesa diameter. The capacitance is measured at -30 V. The number inside the figure represents the size of another mesa that is not marked by the horizontal axis.

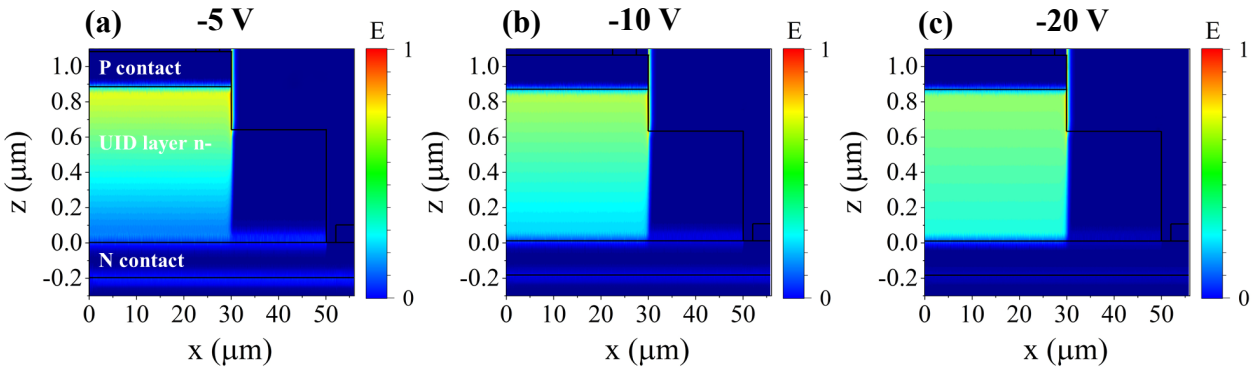

Fig. 4.2-7. Normalized distribution of the electric field magnitude E inside the double mesa devices on sample B (n-type background).

The low-temperatures capacitance of sample B was investigated, since previous research has shown that the background doping in InAs/GaSb superlattices can invert from n-type to p-type when the temperatures is reduced. Such polarity change is attributed to the difference in activation energies of p-type and n-type dopant atoms [87, 88]. If present, this behavior persists in AlInAsSb, electrical characteristics for AlInAsSb APDs would strongly depend on the operating temperature. Fig. 4.2-8 shows the measured capacitance of sample B at -20 V and at 80 K. It suggests that the capacitance is still determined by the top mesa diameter, like in Fig. 4.2-6. This indicates that a background polarity flip has not occurred in $Al_{0.7}InAsSb$ even at cryogenic temperatures. Temperature-independent background polarity can be an important feature for low-temperature operation of AlInAsSb APDs, especially those which are sensitive to high dark currents and may require cooling. The capacitance at 180 K and 350 K was also investigated for sample B and demonstrate the same trend, i.e., the devices consistently show an n-type background behavior. The capacitance does vary with temperature as shown by the 100-150 μm device in Fig. 4.2-8 (b). This can be attributed to the temperature dependence of the AlInAsSb permittivity.

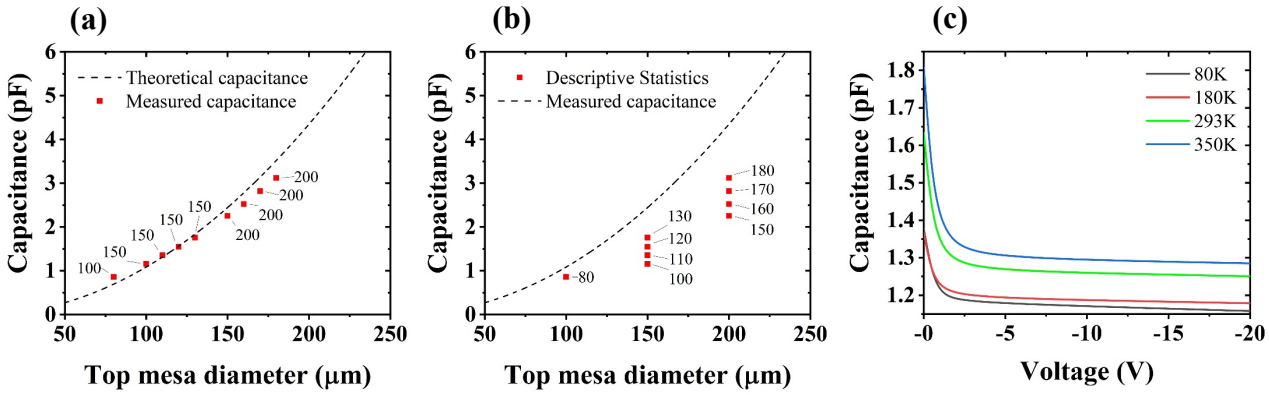

Fig. 4.2-8. Measured capacitance at 80 K of double mesa devices from sample B compared to the theoretical capacitance calculated using either(a) top mesa diameter or (b) bottom mesa diameter. The number inside the figure represents the size of another mesa that is not marked by the horizontal axis. (c) Capacitance-voltage curves of the 150-100 μm devices from sample B measured at different temperatures.

In summary, the C-V characteristics of double mesa $Al_{0.7}InAsSb$ p-i-ns with different background doping polarities were compared. The C-V measurements reveal that the background carrier polarity at low-bias is determined by the top mesa diameter for devices with an n-type background polarity and by the bottom mesa diameter for a p-type background polarity. Identifying the background doping polarity is critical for AlInAsSb APD design, especially for staircase and SACM APDs where the polarity-dependent band bending plays an important role in the device operation. It was also found that the areal dependence of the capacitance for the p-type background double mesa structure reverses at high bias, but not for n-type background structures. This was found to result from the electric field confinement in the smaller top mesa region.

4.3. Future work

In addition to determining background doping, the enhanced field confinement shown by the double mesa structure is also useful for solving the surface field problem of APDs. Surface leakage current, resulting from the recombination and generation through surface states, is one of the primary sources of APD dark current and is strongly affected by the surface electric field. Therefore, as an effective approach to confine the electric field in the bulk region, double/triple mesa structures have been successfully demonstrated to reduce surface leakage dark currents [77, 78].

For the thin absorber SACM APD described in section 2, double/triple mesa structures can serve more than suppressing surface leakage current. In Fig. 2.4-3 (a), it is worth noting that the dark current curve keeps low and flat until it increases abruptly at about -19 V. This is likely caused by the surface breakdown mechanism due to the high electric field in the thin multiplication layer. Therefore, using double/triple mesa structures is beneficial for improving the breakdown performance and achieve higher maximum gain.

As discussed in section 4.2, the electric field is not confined until the depletion extends to the smaller mesa. Therefore, to effectively reduce the surface field in the multiplication layer, the top mesa needs to be etched into the top of the multiplication layer (practically be in charge layer), as shown in Fig. 4.3-1. Following field simulation shows that the surface field is successfully suppressed in the multiplication layer. This is promising to improve the breakdown performance at high gain region.

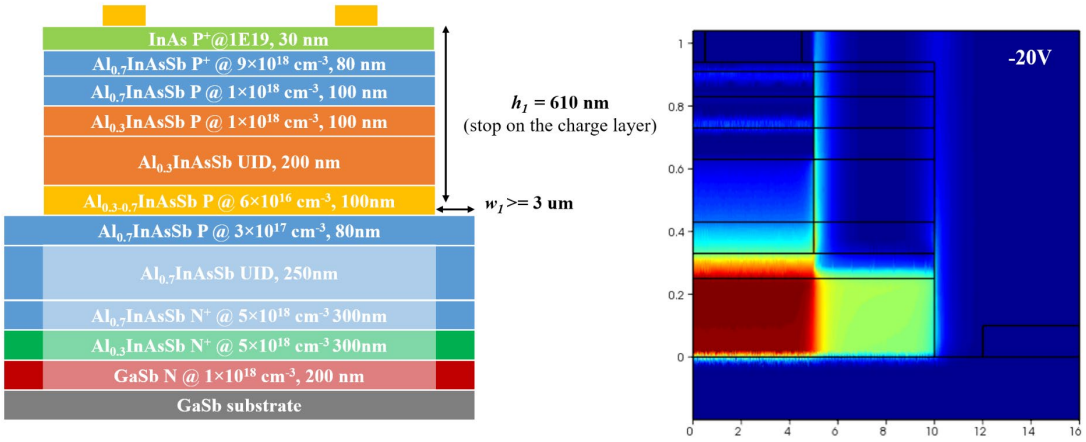

Fig. 4.3-1. Design of the double mesa structure for the thin absorber SACM APD and the simulated electric field profile at – 20 V.

Although the design in Fig 4.3-1 can improve the break down performance, the improvement in the dark current should be limited. Since only the surface field in the multiplication layer is suppressed, dark current is only expected to be reduced before the punch through voltage, where the leakage in the multiplication layer dominates. After the electric field extends into the absorber, the surface leakage in the narrow bandgap material should become dominate, and thus low surface field in the multiplication layer would be less useful for suppressing dark current. Therefore, in order to achieve a lower dark current as well as an improved breakdown performance, a triple mesa structure is needed to suppress the surface filed in both the absorber and the multiplication layer. To achieve this purpose, a top mesa etched into the absorber needs to be added, as shown in Fig. 4.3-2. An electric field simulation shows that the surface field is successfully suppressed in both the absorber and the multiplication layer with the triple mesa design.

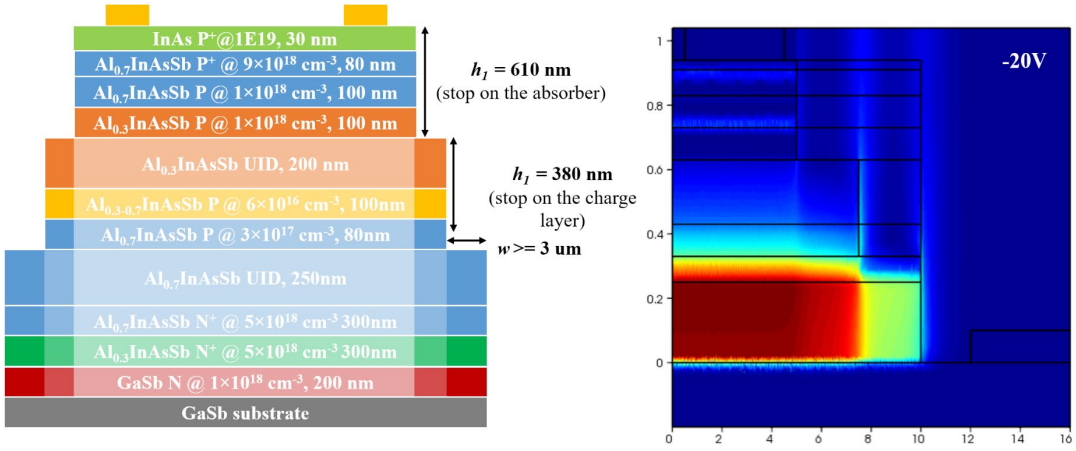

Fig. 4.3-2. Design of the triple mesa structure for the thin absorber SACM APD and the simulated electric field profile at – 20 V.

In summary, the designed two mesa structures in this section are promising to reduce the surface leakage dark current as well as improve the breakdown performance of the thin absorber SACM APD. Therefore, it would be a very promising future work.

References

1. D. Rodrigo, O. Limaj, D. Janner, D. Etezadi, F. J. G. de Abajo, V. Pruneri, and H. Altug, "Mid-infrared plasmonic biosensing with graphene," Science **349**, 165-168 (2015).
2. S. S. Torkestani, S. Sahuguede, A. Julien-Vergonjanne, and J. P. Cances, "Indoor optical wireless system dedicated to healthcare application in a hospital," Iet Commun **6**, 541-547 (2012).
3. A. Hugi, G. Villares, S. Blaser, H. C. Liu, and J. Faist, "Mid-infrared frequency comb based on a quantum cascade laser," Nature **492**, 229-233 (2012).
4. G. Villares, A. Hugi, S. Blaser, and J. Faist, "Dual-comb spectroscopy based on quantum-cascade-laser frequency combs," Nat Commun **5**(2014).
5. U. Willer, M. Saraji, A. Khorsandi, P. Geiser, and W. Schade, "Near- and mid-infrared laser monitoring of industrial processes, environment and security applications," Opt Laser Eng **44**, 699-710 (2006).
6. B. Fang, S. C. Bodepudi, F. Tian, X. Y. Liu, D. Chang, S. C. Du, J. H. Lv, J. Zhong, H. M. Zhu, H. Hu, Y. Xu, Z. Xu, W. W. Gao, and C. Gao, "Bidirectional mid-infrared communications between two identical macroscopic graphene fibres," Nat Commun **11**(2020).
7. M. Razeghi and B. M. Nguyen, "Advances in mid-infrared detection and imaging: a key issues review," Rep Prog Phys **77**(2014).
8. A. H. Jones, S. D. March, S. R. Bank, and J. C. Campbell, "Low-noise high-temperature AlInAsSb/GaSb avalanche photodiodes for 2-mu m applications," Nat Photonics **14**, 559-+ (2020).
9. M. E. Woodson, M. Ren, S. J. Maddox, Y. J. Chen, S. R. Bank, and J. C. Campbell, "Low-noise AlInAsSb avalanche photodiode (vol 108, 081102, 2016)," Appl Phys Lett **108**(2016).
10. S. D. March, A. H. Jones, J. C. Campbell, and S. R. Bank, "Multistep staircase avalanche photodiodes with extremely low noise and deterministic amplification," Nat Photonics **15**, 468-474 (2021).
11. Y. Gao, H. Cansizoglu, K. G. Polat, S. Ghandiparsi, A. Kaya, H. H. Mamtaz, A. S. Mayet, Y. A. Wang, X. Z. Zhang, T. Yamada, E. P. Devine, A. F. Elrefaie, S. Y. Wang, and M. S. Islam, "Photon-trapping microstructures enable high-speed high-efficiency silicon photodiodes," Nat Photonics **11**, 301-+ (2017).
12. J. W. Song, S. Yuan, C. C. Cui, and J. S. Xia, "High-efficiency normal-incidence germanium photodetector with ultra-thin intrinsic layer," 2020 Asia Communications and Photonics Conference (Acp) and International Conference on Information Photonics and Optical Communications (Ipoc) (2020).
13. H. Zhou, S. Q. Xu, Y. D. Lin, Y. C. Huang, B. Son, Q. M. Chen, X. Guo, K. H. Lee, S. C. K. Goh, X. Gong, and C. S. Tan, "High-efficiency GeSn/Ge multiple-quantum-well photodetectors with photon-trapping microstructures operating at 2 mu m," Opt Express **28**, 10280-10293 (2020).
14. M. Lodari, P. Biagioni, M. Ortolani, L. Baldassarre, G. Isella, and M. Bollani, "Plasmon-enhanced Ge-based metal-semiconductor-metal photodetector at near-IR wavelengths," Opt Express **27**, 20516-20524 (2019).
15. P. Latzel, F. Pavanello, M. Billet, S. Bretin, A. Beck, M. Vanwolleghem, C. Coinon, X. Wallart, E. Peytavit, G. Ducournau, M. Zaknoune, and J. F. Lampin, "Generation of mW Level in the 300-GHz Band Using Resonant-Cavity-Enhanced Unitraveling Carrier Photodiodes," Ieee T Thz Sci Techn **7**, 800-807 (2017).
16. H. T. Miyazaki, T. Mano, T. Kasaya, H. Osato, K. Watanabe, Y. Sugimoto, T. Kawazu, Y. Arai, A. Shigetou, T. Ochiai, Y. Jimba, and H. Miyazaki, "Synchronously wired infrared antennas for resonant single-quantum-well photodetection up to room temperature," Nat Commun **11**(2020).
17. D. Palaferri, Y. Todorov, A. Bigioli, A. Mottaghizadeh, D. Gacemi, A. Calabrese, A. Vasanelli, L. H. Li, A. G. Davies, E. H. Linfield, F. Kapsalidis, M. Beck, J. Faist, and C. Sirtori, "Room-temperature nine-mu m-wavelength photodetectors and GHz-frequency heterodyne receivers," Nature **556**, 85-+ (2018).
18. M. W. Knight, H. Sobhani, P. Nordlander, and N. J. Halas, "Photodetection with Active Optical Antennas," Science **332**, 702-704 (2011).
19. A. R. J. Marshall, P. J. Ker, A. Krysa, J. P. R. David, and C. H. Tan, "High speed InAs electron avalanche photodiodes overcome the conventional gain-bandwidth product limit," Opt Express **19**, 23341-23349 (2011).
20. A. H. Jones, Y. Shen, K. Y. Sun, D. K. Chen, S. D. March, S. R. Bank, and J. C. Campbell, "Room-temperature bandwidth of 2-mu m AlInAsSb avalanche photodiodes," Opt Express **29**, 38939-38945 (2021).
21. K. Aydin, V. E. Ferry, R. M. Briggs, and H. A. Atwater, "Broadband polarization-independent resonant light absorption using ultrathin plasmonic super absorbers," Nat Commun **2**(2011).
22. D. J. Ironside, R. Salas, P. Y. Chen, K. Q. Le, A. Alu, and S. R. Bank, "Enhancing THz generation in photomixers using a metamaterial approach," Opt Express **27**, 9481-9494 (2019).

23. C. W. Berry, N. Wang, M. R. Hashemi, M. Unlu, and M. Jarrahi, "Significant performance enhancement in photoconductive terahertz optoelectronics by incorporating plasmonic contact electrodes," Nat Commun **4**(2013).
24. J. T. Shen, P. B. Catrysse, and S. H. Fan, "Mechanism for designing metallic metamaterials with a high index of refraction," Phys Rev Lett **94**(2005).
25. B. Y. Hsieh and M. Jarrahi, "Analysis of periodic metallic nano-slits for efficient interaction of terahertz and optical waves at nano-scale dimensions," J Appl Phys **109**(2011).
26. J. B. Pendry, L. Martin-Moreno, and F. J. Garcia-Vidal, "Mimicking surface plasmons with structured surfaces," Science **305**, 847-848 (2004).
27. Y. M. Lyaschuk and V. V. Korotyeyev, "Interaction of terahertz electromagnetic field with a metallic grating: Near-field zone," Ukr J Phys Opt **13**, 142-150 (2012).
28. S. A. Mikhailov, "Plasma instability and amplification of electromagnetic waves in low-dimensional electron systems," Phys Rev B **58**, 1517-1532 (1998).
29. Y. Yuan, J. Y. Zheng, A. K. Rockwell, S. D. March, S. R. Bank, and J. C. Campbell, "AlInAsSb Impact Ionization Coefficients," Ieee Photonic Tech L **31**, 315-318 (2019).
30. Y. Yuan, A. K. Rockwell, Y. W. Peng, J. Y. Zheng, S. D. March, A. H. Jones, M. Ren, S. R. Bank, and J. C. Campbell, "Comparison of Different Period Digital Alloy Al-0.7 InAsSb Avalanche Photodiodes," J Lightwave Technol **37**, 3647-3654 (2019).
31. H. D. Liu, H. P. Pan, C. Hu, D. McIntosh, Z. W. Lu, J. Campbell, Y. M. Kang, and M. Morse, "Avalanche photodiode punch-through gain determination through excess noise analysis," J Appl Phys **106**(2009).
32. R. J. Mcintyre, "Multiplication Noise in Uniform Avalanche Diodes," Ieee T Electron Dev **Ed13**, 164-+ (1966).
33. O. Gravrand, J. Rothman, C. Cervera, N. Baier, C. Lobre, J. P. Zanatta, O. Boulade, V. Moreau, and B. Fieque, "HgCdTe Detectors for Space and Science Imaging: General Issues and Latest Achievements," J Electron Mater **45**, 4532-4541 (2016).
34. Raith, "RAITH150 Two Ebeam Writer", https://raith.com/product/raith150-two/.
35. Kayaku, "PMMA photoresist data sheet", https://kayakuam.com/wp-content/uploads/2021/07/KAM-PMMA-Datasheet-4.12.21-final.pdf.
36. Kayaku, "LOR and PMGI Resists for Bi-layer Lift-off Processing", https://kayakuam.com/wp-content/uploads/2019/09/KAM-LOR-PMGI-Data-Sheet-11719.pdf.
37. D. K. Chen, K. Y. Sun, A. H. Jones, and J. C. Campbell, "Efficient Absorption Enhancement Approaches for AlInAsSb Avalanche Photodiodes for 2-mu m Applications," Ieee Photon Conf (2020).
38. Q. H. Yu, J. Y. Gao, N. Ye, B. H. Chen, K. Y. Sun, L. L. Xie, K. Srinivasan, M. Zervas, G. Navickaite, M. Geiselmann, and A. Beling, "Heterogeneous photodiodes on silicon nitride waveguides," Opt Express **28**, 14824-+ (2020).
39. K. Y. Sun, J. Y. Gao, D. Jung, J. Bowers, and A. Beling, "40 Gbit/s waveguide photodiode using III-V on silicon heteroepitaxy," Opt Lett **45**, 2954-2956 (2020).
40. Y. Yuan, Z. H. Huang, X. G. Zeng, D. Liang, W. V. Sorin, M. Fiorentino, and R. G. Beausoleil, "High Responsivity Si-Ge Waveguide Avalanche Photodiodes Enhanced by Loop Reflector," Ieee J Sel Top Quant **28**(2022).
41. R. L. Chao, J. M. Wun, Y. W. Wang, Y. H. Chen, J. E. Bowers, and J. W. Shi, "High-Speed and High-Power GaSb Based Photodiode for 2.5 mu m Wavelength Operations," 2016 Ieee Photonics Conference (Ipc), 472-473 (2016).
42. J. A. Huang, Z. Y. Xie, Y. J. Chen, J. E. Bowers, and B. L. Chen, "High Speed Mid-Wave Infrared Uni-Traveling Carrier Photodetector," Ieee J Quantum Elect **56**(2020).
43. R. Chevallier, A. Haddadi, R. McClintock, A. Dehzangi, V. Lopez-Dominguez, P. K. Amiri, and M. Razeghi, "High Frequency Extended Short-Wavelength Infrared Heterojunction Photodetectors Based on InAs/GaSb/AlSb Type-II Superlattices," Ieee J Quantum Elect **54**(2018).
44. A. Dehzangi, R. McClintock, D. H. Wu, J. K. Li, S. M. Johnson, E. Dial, and M. Razeghi, "High speed antimony-based superlattice photodetectors transferred on sapphire," Appl Phys Express **12**(2019).
45. H. J. Lee, H. C. Jung, A. Jang, J. G. Kim, S. Y. Ko, Y. H. Kim, and J. Nah, "Dark current improvement due to dry-etch process in InAs/GaSb type-II superlattice LWIR photodetector with nBn structure," Infrared Phys Techn **94**, 161-164 (2018).
46. J. B. Rodriguez, E. Plis, G. Bishop, Y. D. Sharma, H. Kim, L. R. Dawson, and S. Krishna, "nBn structure based on InAs/GaSb type-II strained layer superlattices," Appl Phys Lett **91**(2007).
47. A. Soibel, D. Z. Ting, S. B. Rafol, A. M. Fisher, S. A. Keo, A. Khoshakhlagh, and S. D. Gunapala, "Mid-wavelength infrared InAsSb/InAs nBn detectors and FPAs with very low dark current density," Appl Phys Lett **114**(2019).

48. D. Z. Ting, A. Soibel, A. Khoshakhlagh, S. A. Keo, A. M. Fisher, S. B. Rafol, L. Hoglund, C. J. Hill, B. J. Pepper, and S. D. Gunapala, "Long wavelength InAs/InAsSb superlattice barrier infrared detectors with p-type absorber quantum efficiency enhancement," Appl Phys Lett **118**(2021).
49. K. Michalczewski, P. Martyniuk, L. Kubiszyn, C. H. Wu, Y. R. Wu, J. Jurenczyk, A. Rogalski, and J. Piotrowski, "Demonstration of the Very Long Wavelength Infrared Type-II Superlattice InAs/InAsSb GaAs Immersed Photodetector Operating at Thermoelectric Cooling," Ieee Electr Device L **40**, 1396-1398 (2019).
50. H. S. Kim, O. O. Cellek, Z. Y. Lin, Z. Y. He, X. H. Zhao, S. Liu, H. Li, and Y. H. Zhang, "Long-wave infrared nBn photodetectors based on InAs/InAsSb type-II superlattices," Appl Phys Lett **101**(2012).
51. D. Z. Ting, A. Soibel, A. Khoshakhlagh, S. A. Keo, S. B. Rafol, A. M. Fisher, B. J. Pepper, E. M. Luong, C. J. Hill, and S. D. Gunapala, "Advances in III-V semiconductor infrared absorbers and detectors," Infrared Phys Techn **97**, 210-216 (2019).
52. E. H. Steenbergen, B. C. Connelly, G. D. Metcalfe, H. Shen, M. Wraback, D. Lubyshev, Y. Qiu, J. M. Fastenau, A. W. K. Liu, S. Elhamri, O. O. Cellek, and Y. H. Zhang, "Significantly improved minority carrier lifetime observed in a long-wavelength infrared III-V type-II superlattice comprised of InAs/InAsSb," Appl Phys Lett **99**(2011).
53. I. Vurgaftman, G. Belenky, Y. Lin, D. Donetsky, L. Shterengas, G. Kipshidze, W. L. Sarney, and S. P. Svensson, "Interband absorption strength in long-wave infrared type-II superlattices with small and large superlattice periods compared to bulk materials," Appl Phys Lett **108**(2016).
54. P. C. Klipstein, Y. Livneh, A. Glozman, S. Grossman, O. Klin, N. Snapi, and E. Weiss, "Modeling InAs/GaSb and InAs/InAsSb Superlattice Infrared Detectors," J Electron Mater **43**, 2984-2990 (2014).
55. A. H. Jones, A. K. Rockwell, S. D. March, Y. Yuan, S. R. Bank, and J. C. Campbell, "High Gain, Low Dark Current Al0.8In0.2As0.23Sb0.77 Avalanche Photodiodes," Ieee Photonic Tech L **31**, 1948-1951 (2019).
56. A. H. Jones, Y. Yuan, M. Ren, S. J. Maddox, S. R. Bank, and J. C. Campbell, "Al(x)In(1-x)AsySb(1-y) photodiodes with low avalanche breakdown temperature dependence," Opt Express **25**, 24340-24345 (2017).
57. M. E. Woodson, M. Ren, S. J. Maddox, Y. J. Chen, S. R. Bank, and J. C. Campbell, "Low-noise AlInAsSb avalanche photodiode," Appl Phys Lett **108**(2016).
58. J. Y. Zheng, A. H. Jones, Y. H. Tan, A. K. Rockwell, S. March, S. Z. Ahmed, C. A. Dukes, A. W. Ghosh, S. R. Bank, and J. C. Campbell, "Characterization of band offsets in AlxIn1-xAsySb1-y alloys with varying Al composition," Appl Phys Lett **115**(2019).
59. D. Z. Ting, A. Soibel, A. Khoshakhlagh, and S. D. Gunapala, "Theoretical analysis of nBn infrared photodetectors," Opt Eng **56**(2017).
60. D. Zuo, R. Y. Liu, D. Wasserman, J. Mabon, Z. Y. He, S. Liu, Y. H. Zhang, E. A. Kadlec, B. V. Olson, and E. A. Shaner, "Direct minority carrier transport characterization of InAs/InAsSb superlattice nBn photodetectors," Appl Phys Lett **106**(2015).
61. P. Martyniuk, W. Pusz, W. Gawron, D. Stepien, L. Kubiszyn, S. Krishna, and A. Rogalski, "nBn T2SLs InAs/GaSb/B-AlGaSb HOT Detector for Fast Frequency Response Operation," C Optoelectr Micro, 226-229 (2014).
62. B. L. Chen, Y. J. Chen, and Z. Deng, "Recent Advances in High Speed Photodetectors for eSWIR/MWIR/LWIR Applications," Photonics-Basel **8**(2021).
63. M. Yang, W. B. Xu, Z. Y. Sun, H. Wu, Y. Z. Tian, and L. T. Li, "Mid-wave infrared polarization imaging system for detecting moving scene," Opt Lett **45**, 5884-5887 (2020).
64. L. X. Zhang, J. Ke, S. Chi, X. W. Hao, T. Yang, and D. W. Cheng, "High-resolution fast mid-wave infrared compressive imaging," Opt Lett **46**, 2469-2472 (2021).
65. A. Schliesser, N. Picque, and T. W. Hansch, "Mid-infrared frequency combs," Nat Photonics **6**, 440-449 (2012).
66. B. Meng, M. Singleton, M. Shahmohammadi, F. Kapsalidis, R. J. Wang, M. Beck, and J. Faist, "Mid-infrared frequency comb from a ring quantum cascade laser," Optica **7**, 162-167 (2020).
67. S. Lambert-Girard, N. Ho, B. Bourliaguet, D. Lemieux, M. Piche, and F. Babin, "Broadband spectroscopic lidar for SWIR/MWIR detection of gaseous pollutants in air," Proc Spie **8534**(2012).
68. D. K. Chen, R. J. Wang, J. A. McArthur, X. J. Xue, A. H. Jones, S. R. Bank, and J. C. Campbell, "Demonstration of infrared nBn photodetectors based on the AlInAsSb digital alloy materials system," Appl Phys Lett **119**(2021).
69. S. J. Maddox, S. D. March, and S. R. Bank, "Broadly Tunable AlInAsSb Digital Alloys Grown on GaSb," Cryst Growth Des **16**, 3582-3586 (2016).
70. N. D. Akhavan, G. Jolley, G. A. Umana-Membreno, J. Antoszewski, and L. Faraone, "Design of Band Engineered HgCdTe nBn Detectors for MWIR and LWIR Applications," Ieee T Electron Dev **62**, 722-728 (2015).
71. K. Kato, S. Hata, K. Kawano, and A. Kozen, "Design of Ultrawide-Band, High-Sensitivity P-I-N Protodetectors," Ieice T Electron **E76**, 214-221 (1993).

72. Lumerical, "CHARGE: 3D Charge Transport Simulator", retrieved https://www.lumerical.com/.
73. D. K. Chen, J. A. McArthur, S. D. March, X. J. Xue, A. H. Jones, A. A. Dadey, S. R. Bank, and J. C. Campbell, "Comparison and analysis of Al0.7InAsSb avalanche photodiodes with different background doping polarities," Appl Phys Lett **119**(2021).
74. J. C. Campbell, "Phototransistors for Lightwave Communications," Semiconduct Semimet **22**, 389-447 (1985).
75. S. Maimon and G. W. Wicks, "nBn detector, an infrared detector with reduced dark current and higher operating temperature," Appl Phys Lett **89**(2006).
76. D. K. Chen, K. Y. Sun, A. H. Jones, and J. C. Campbell, "Efficient absorption enhancement approaches for AllnAsSb avalanche photodiodes for 2-mu m applications," Opt Express **28**, 24379-24388 (2020).
77. Y. Yuan, Y. B. Li, J. Abell, J. Y. Zheng, K. Y. Sun, C. Pinzone, and J. C. Campbell, "Triple-mesa avalanche photodiodes with very low surface dark current," Opt Express **27**, 22923-22929 (2019).
78. M. Nada, Y. Muramoto, H. Yokoyama, T. Ishibashi, and H. Matsuzaki, "Triple-mesa Avalanche Photodiode With Inverted P-Down Structure for Reliability and Stability," J Lightwave Technol **32**, 1543-1548 (2014).
79. C. Anayama, T. Tanahashi, H. Kuwatsuka, S. Nishiyama, S. Isozumi, and K. Nakajima, "High-Purity Gasb Epitaxial Layers Grown from Sb-Rich Solutions," Appl Phys Lett **56**, 239-240 (1990).
80. A. Hood, D. Hoffman, Y. J. Wei, F. Fuchs, and M. Razeghi, "Capacitance-voltage investigation of high-purity InAs/GaSb superlattice photodiodes," Appl Phys Lett **88**(2006).
81. T. Asar, S. Ozcelik, and E. Ozbay, "Structural and electrical characterizations of InxGa1-xAs/InP structures for infrared photodetector applications," J Appl Phys **115**(2014).
82. T. Ambridge and M. M. Faktor, "Automatic Carrier Concentration Profile Plotter Using an Electrochemical Technique," J Appl Electrochem **5**, 319-328 (1975).
83. H. A. Donsig and J. C. Vickerman, "Dynamic and static secondary ion mass spectrometry studies of the solvation of HCl by ice," J Chem Soc Faraday T **93**, 2755-2761 (1997).
84. D. R. Fink, S. Lee, S. H. Kodati, V. Rogers, T. J. Ronningen, M. Winslow, C. H. Grein, A. H. Jones, J. C. Campbell, J. F. Klem, and S. Krishna, "Determination of background doping polarity of unintentionally doped semiconductor layers," Appl Phys Lett **116**(2020).
85. Q. Li, F. Wang, P. Wang, L. L. Zhang, J. L. He, L. Chen, P. Martyniuk, A. Rogalski, X. S. Chen, W. Lu, and W. D. Hu, "Enhanced Performance of HgCdTe Midwavelength Infrared Electron Avalanche Photodetectors With Guard Ring Designs," Ieee T Electron Dev **67**, 542-546 (2020).
86. M. J. Lee, H. Rucker, and W. Y. Choi, "Effects of Guard-Ring Structures on the Performance of Silicon Avalanche Photodetectors Fabricated With Standard CMOS Technology," Ieee Electr Device L **33**, 80-82 (2012).
87. A. Khoshakhlagh, F. Jaeckel, C. Hains, J. B. Rodriguez, L. R. Dawson, K. Malloy, and S. Krishna, "Background carrier concentration in midwave and longwave InAs/GaSb type II superlattices on GaAs substrate," Appl Phys Lett **97**(2010).
88. C. Cervera, J. B. Rodriguez, J. P. Perez, H. Ait-Kaci, R. Chaghi, L. Konczewicz, S. Contreras, and P. Christol, "Unambiguous determination of carrier concentration and mobility for InAs/GaSb superlattice photodiode optimization," J Appl Phys **106**(2009).

Appendix

A. Normal APD fabrication recipe

This recipe is used to fabricate normal-incidence APD/nBn photodetectors introduced in section 2.4, section 2.5.2, section 3.3 and section 4.2.

1. Clean the bare sample by Acetone, Methanol, IPA and DI water in sequence. Ultrasonic bath or spinner can be used to increase the efficiency of the cleaning.
2. Bake the cleaned sample at 100 ºC for 1 min to remove residual moisture on the surface.
3. Spin AZ 5214 photoresist on the sample at a speed of 4000 rpm and for 30s.
4. Pre-bake the coated sample at 100 ºC for 1 min.
5. Expose mesa patterns by mask align lithography, and then develop the sample in AZ 300 MIF for 30s.
6. Wet etch the mesa structure by citric acid ($C_6H_8O_7$) solution. A commonly used composition is 20g $C_6H_8O_7$, 15 mL H_3PO_4, 120 mL DI and 5 mL H_2O_2. The etch rate for digital alloy AlInAsSb is typically 5~10 nm/s.
7. Remove photoresist by the same procedure as in step 1. If the photoresist cannot be completely removed, try using NMP (1-Methyl-2-pyrrolidone) heated to 60 ºC ~ 90 ºC and with ultrasonic bath.
8. Repeat step 2~4 to coat AZ 5214 photoresist on the sample again.
9. Expose metal contacts patterns by mask align lithography, and then develop the sample in AZ 300 MIF for 30s.
10. Deposit 10 nm Ti layer and 100 nm Au layer in sequence on the sample by the e-beam evaporator.
11. Dip the coated sample in heated NMP (60 ºC ~ 90 ºC) for ~ 10 min, and then use ultrasonic bath for 5 ~ 10 min until the metal on the photoresist layer is lifted-off. Then, clean the sample by repeating step 1.
12. Spin SU8 2000.5 photoresist on the sample at a speed of 5000 rpm and for 40s.
13. Pre-bake the coated sample at 90 ºC for 70 s.
14. Expose the passivation windows by mask align lithography, and then post-bake the sample at 90 ºC for 70 s. Finally, develop the sample in SU8 developer for 1 min.
15. Fabrication finished, and the sample is ready for test.

B. Metal grating fabrication by single layer lift-off

This recipe is used to fabricate sub-micron metal gratings introduced in section 2.5.1 by using a single PMMA photoresist layer.

1. Clean the bare sample by Acetone, Methanol, IPA and DI water in sequence. Ultrasonic bath or spinner can be used to increase the efficiency of the cleaning.
2. Bake the cleaned sample at 100 ºC for 1 min to remove residual moisture on the surface.
3. Spin PMMA photoresist on the sample. Different PMMA dilution and spin speed can provide photoresist layer with different thicknesses. For more details, please refer to section 2.5.1 or the factory data sheet [35].
4. Pre-bake the coated sample at 180 ºC for 1 min 30 s.
5. Expose the metal grating patterns by e-beam lithography with electron energy of 30 keV (maximum energy of RAITH 150-2). The appropriate does for a thin PMMA layer (~ 200 nm) should be 40 ~ 50 μC/cm^2. For a thick PMMA layer (0.7 ~ 1.2 μm), the does need to be increased to 150 ~ 160 μC/cm^2. Actual does may varies if the beam current changes, or if different developer dilution and different PMMA layer thickness are used. Therefore, does test is highly recommended before fabrication.
6. Develop the sample in MIBK developer for ~ 1 min 20 s with dilution of MIBK:IPA = 1:3, and 50 s ~ 60 s with dilution of MIBK:IPA = 3:1. Typically, thicker MIBK solution can provide high sensitivity, which is suitable for a thick PMMA layer, and thinner MIBK solution can provide higher resolution. Actual development time may vary a lot for different e-beam does and photoresist layer thickness, therefore development time test is highly recommended before fabrication.
7. Deposit 10 nm Ti layer and 370 nm Au layer in sequence on the sample by the e-beam evaporator. The Ti layer is used to enhance the adhesion between the metal and the semiconductor surface.
8. Dip the coated sample in heated NMP (60 ºC ~ 90 ºC) for at least 30 min (safe to leave it overnight), and wash the sample by Acetone, Methanol, IPA and DI water in sequence by using a spinner. Ultrasonic bath should be avoided in most cases.
9. Metal grating fabrication is finished.

C. Metal grating fabrication by double layer lift-off

This recipe is used to fabricate sub-micron metal gratings introduced in section 2.5.1 by using a combination of PMGI photoresist layer and PMMA photoresist layer.

1. Clean the bare sample by Acetone, Methanol, IPA and DI water in sequence. Ultrasonic bath or spinner can be used to increase the efficiency of the cleaning.
2. Bake the cleaned sample at 100 ºC for 1 min to remove residual moisture on the surface.
3. Spin PMGI photoresist on the sample. Different PMGI dilution and spin speed can provide photoresist layer with different thickness. For more details, please refer to the factory data sheet [36]. Typically, the PMGI layer needed to be ~ 0.33 times thicker than the metal layer.
4. Pre-bake PMGI layer at 180 ºC for 5 min.
5. Spin PMMA photoresist on the sample. Different PMMA dilution and spin speed can provide photoresist layer with different thickness. For more details, please refer to the factory data sheet [35]. Typically for double layer lift-off, a PMMA layer of ~ 200 nm is more than enough.
6. Pre-bake PMGI layer at 180 ºC for 1 min 30 s.
7. Expose the metal grating patterns by e-beam lithography with electron energy of 30 keV (maximum energy of RAITH 150-2). The appropriate does for a PMMA layer of 200 nm and a PMGI layer of 500 nm is ~ 200 $\mu C/cm^2$. The high does used here is to create an anisotropic wet etch, as introduced in section 2.5.1.
8. Develop the PMMA layer in MIBK developer for ~ 1 min 20 s with a dilution of MIBK:IPA = 1:3. Then, wet etch the underlaying PMGI layer by TMAH 0.26 N developer for ~ 10s. As introduced in section 2.5.1, it needs to be careful on controlling the wet time because the lateral dimension of the feature is very small. Thus, wet etch time test is highly recommended before the actual fabrication.
9. Deposit 10 nm Ti layer and 370 nm Au layer in sequence on the sample by the e-beam evaporator. The Ti layer is used to enhance the adhesion between the metal and the semiconductor surface.
10. Dip the coated sample in heated NMP (60 ºC ~ 90 ºC) for at least 30 min (safe to leave it overnight), and wash the sample by Acetone, Methanol, IPA and DI water in sequence by using a spinner. Ultrasonic bath should be avoided in most cases.
11. Metal grating fabrication is finished.

List of Publications

Journals:

1. **Dekang Chen**, Keye Sun, Andrew H. Jones, Joe C. Campbell, "Efficient absorption enhancement approaches for AlInAsSb avalanche photodiodes for 2-μm applications", *Optics Express* 28 (17), 24379-24388 (2020).

2. **Dekang Chen**, J. Andrew McArthur, Stephen D. March, Xingjun Xue, Andrew H. Jones, Adam A. Dadey, Seth R. Bank, Joe C. Campbell, "Comparison and analysis of Al0.7InAsSb avalanche photodiodes with different background doping polarities", *Applied Physics Letters* 119 (3), 032101 (2021).

3. **Dekang Chen**, Renjie Wang, J Andrew McArthur, Xingjun Xue, Andrew H Jones, Seth R Bank, Joe C Campbell, "Demonstration of infrared nBn photodetectors based on the AlInAsSb digital alloy materials system", *Applied Physics Letters* 119 (3), 031101 (2021).

4. **Dekang Chen**, Keye Sun, Yang Shen, Andrew H. Jones, Adam A. Dadey, Bingtian Guo, J. Andrew McArthur, Seth R. Bank, Joe C. Campbell, "Frequency behavior of AlInAsSb nBn photodetectors and the development of an equivalent circuit model", *Optics Express* 30 (14), 25262-25276 (2022).

5. Renjie Wang, **Dekang Chen**, J. Andrew McArthur, Xingjun Xue, Andrew H. Jones, Seth R. Bank, Joe C. Campbell, "Al0.3InAsSb/Al0.7InAsSb Digital Alloy nBn Photodetectors", *Journal of Lightwave Technology* 40 (1), 113-120 (2021).

6. Andrew H. Jones, Yang Shen, Keye Sun, **Dekang Chen**, Stephen D. March, Seth R. Bank, Joe C. Campbell, "Room-temperature bandwidth of 2-μm AlInAsSb avalanche photodiodes", *Optics Express* 29 (23), 38939-38945 (2021).

7. Bingtian Guo, Xiao Jin, Seunghyun Lee, Sheikh Z Ahmed, Andrew Jones, Xingjun Xue, Baolai Liang, Harry Lewis, Sri Harsha Kodati, **Dekang Chen**, Theodore James Ronningen, Christoph Grein, Avik Ghosh, Sanjay Krishna, John P David, Joe C Campbell, "Impact ionization coefficients of digital alloy and random alloy $Al_{0.85}Ga_{0.15}As_{0.56}Sb_{0.44}$ in a wide electric field range", *Journal of Lightwave Technology* (2022).

8. Xiangwen Guo, Linbo Shao, Lingyan He, Kevin Luke, Jesse Morgan, Keye Sun, Junyi Gao, Ta-Ching Tzu, Yang Shen, **Dekang Chen**, Bingtian Guo, Fengxin Yu, Qianhuan Yu, Masoud Jafari, Marko Lončar, Mian Zhang, Andreas Beling, "High-performance modified uni-traveling carrier photodiode integrated on a thin-film lithium niobate platform", *Photonics Research* 10, 1338-1343 (2022).

Conferences:

1. **Dekang Chen**, Keye Sun, Andrew H. Jones, Joe C. Campbell, “Efficient absorption enhancement approaches for AlInAsSb avalanche photodiodes for 2-μm applications”, 2020 IEEE Photonics Conference (IPC).

2. Renjie Wang, **Dekang Chen**, J. Andrew McArthur, Xingjun Xue, Andrew H. Jones, Seth R. Bank, Joe C. Campbell, “$Al_xIn_{1-x}As_ySb_{1-y}$ digital alloy nBn Photodetectors”, 2021 IEEE Photonics Conference (IPC).